Simulation of Additively Manufactured Auxetic Lattice Structures for the Estimation of Energy Absorption and Dissipation Potentials

Simulation von additiv gefertigten auxetischen Gitterstrukturen zur Abschätzung ihres Energieabsorptions- und -dissipationspotenzials

Master thesis by Hugo Pamies Moreno (



Date: 26.09.2025

1. Review: Prof. Dr. Oliver Weeger

2. Review: Mathieu Vinot

Darmstadt





Abstract

This thesis investigates the potential of additively manufactured auxetic lattice structures for energy absorption and dissipation with a particular emphasis on their crashworthiness performance. Auxetic materials, characterized by their negative Poisson's ratio, possess peculiar deformation mechanisms that cause lateral contraction under compression, sugesting potential advantages for energy absorption.

Three thermoplastic polymers were selected to explore the influence of mechanical properties on the acquirable performance: TPU, PP, and PA12, which were characterized through mechanical testing following ISO standards for tension and compression. High Speed Sintering (HSS) manufacturing was used to produce specimens and the auxetic structures. From the test data, material models were developed and validated in LS-DYNA, progressing from simple piecewise linear plasticity (MAT 024) to an advanced compression-tension differentiated model (MAT 124).

A parametric numerical investigation was carried out in order to evaluate the influence of several design variables on the energy absorption capability of the auxetics. The study included the effects of unit cell base size, relative strut thickness, loading orientation, and material selection on performance metrics such as Specific Energy Absorption (SEA), Peak Crushing Force (PCF), and Mean Crushing Force (MCF).

The results demonstrated a 25% higher SEA in 3D reentrant structures loaded at 90° compared to the standard orientation, and an optimal relative thickness of 10% of the base size. Energy dissipation mechanisms were quantified by analyzing both stored elastic energy and irreversibly dissipated energy through loading-unloading simulations. PA12 presented the highest dissipation ratio (96%) due to failure, while TPU showed predominantly elastic behavior, and PP provided an intermediate performance, but the highest overall SEA.

A comparative analysis later revealed superior crashworthiness in conventional lattice architectures. Similarly, 2D honeycomb and extruded reentrant structures outperformed their 3D counterparts, achieving higher SEA values, but at the cost of increased structural mass.

This research establishes a methodology for the design, manufacturing, and simulation of auxetic structures for crash applications. The study provides valuable insights into their trade-offs in terms of structural performance, providing guidance for future accurate simulations of HSS 3D printed crash structures and lattices.

i۷

Acknowledgments

The opportunity Mathieu Vinot gave me by offering me this thesis has been truly extraordinary, and I am very grateful to him for introducing me to the fascinating world of research in the field of materials and structural integrity.

I would like to thank the fantastic team at the Institute of Structures and Design of the German Aerospace Center (DLR) for sharing their expertise, my internship colleagues, and Tobias and Dorothea for their patience in showing me the procedures for each experiment and for trusting me with the laboratory equipment.

I would also like to thank Oliver Weeger for his kindness in acting as my supervisor on behalf of TU Darmstadt, and my other supervisor, Mohamed Ichchou, for giving me the chance to finish my studies with this enriching exchange year.

Since this work marks the end of my academic path, I would also like to take this opportunity to acknowledge the role of everyone who has stood by me from the beginning. In particular, my friends at Xtra2, who always make me want to go back to the workshop at UPV, where I began my journey into the exciting world of aerospace engineering. Jose Morcillo for his trust, Marc Aragó for always letting me be his co-pilot, and David Silla for always coming to talk about airplanes, no matter where.

To the friends who enthusiastically joined me on the adventure of building a prototype at École Centrale de Lyon. And to my colleagues of the Akamodell Stuttgart, for sharing their decades of know-how with me, for teaching me to feel the wind and fly with the birds.

I want to thank Andreea for staying by my side during these years of constant change, for believing in me, for giving me the most beautiful warmth I know, and for always helping me to become better.

Por último, quiero darle las gracias a mi familia, que siempre me ha apoyado en mi formación científica y humana. También a mi familia que ya no está, pero que sé que se alegraría de verme graduado. A mis hermanos por soportarme desde que éramos pequeños, y a mis padres por su enorme generosidad.

Contents

| • | muc | duction |
|---|------|--|
| | 1.1 | Motivation |
| | 1.2 | Approach |
| 2 | Fund | damentals 3 |
| | 2.1 | Energy Absorption and Dissipation |
| | 2.2 | Lattice Structures |
| | 2.3 | Auxetic Structures |
| | 2.4 | Additive Manufacturing |
| | 2.5 | Testing Standards |
| | | 2.5.1 ISO 527: Tensile Testing of Polymers |
| | | 2.5.2 ISO 604: Compression Testing of Polymers |
| | 2.6 | Simulation in LS-DYNA |
| | | 2.6.1 Implicit and Explicit Simulations |
| | | 2.6.2 Suitability |
| | 2.7 | Material Models in LS-DYNA |
| | ۵., | 2.7.1 *MAT 024 |
| | | 2.7.2 *MAT 124 |
| | | 2.7.3 Selection Criteria: Triaxiality |
| | 2.8 | Research Definition |
| | 2.0 | 2.8.1 Hypothesis |
| | | 2.0.1 Hypothesis |
| 3 | Mate | erial Characterization 19 |
| | 3.1 | Selection of Materials |
| | 3.2 | HSS Additive Manufacturing |
| | 3.3 | Characterization Techniques |
| | | 3.3.1 DIC |
| | | 3.3.2 Tensile Test |
| | | 3.3.3 Compression Test |
| | 3.4 | Manufacturing Anisotropy |
| | 3.5 | Summary of Properties |
| | 3.6 | Material Model Implementation |
| | | 3.6.1 Triaxiality Dependent Failure |
| 4 | Muse | nerical Investigation 35 |
| 4 | | • |
| | 4.1 | Validation of the Material Cards |
| | 4.2 | Structure Parametrization and 3D Modelling |

| | 4.3 | Automated Meshing | 1 |
|----|------|-----------------------------------|---|
| | 4.4 | Simulation Setup | 3 |
| | | 4.4.1 Control | 3 |
| | | 4.4.2 Boundary Conditions | 4 |
| | | 4.4.3 Contact Definition | 5 |
| | 4.5 | Postprocess Methodology | 5 |
| 5 | Disc | eussion 4 | 6 |
| | 5.1 | General Behavior | 6 |
| | 5.2 | Experimental Validation | 8 |
| | 5.3 | Effect of the material model | 9 |
| | 5.4 | Load Angle | 0 |
| | 5.5 | Unit Cell Base Size | 1 |
| | 5.6 | Relative Thickness | 2 |
| | 5.7 | Effect of the material properties | 3 |
| | 5.8 | Energy Dissipation | 4 |
| | 5.9 | Performance Against 2D Structures | 5 |
| | 5.10 | Performance Against Non-Auxetics | 7 |
| 6 | Con | clusions 5 | 8 |
| | 6.1 | Summary | 8 |
| | 6.2 | Challenges | 9 |
| | 6.3 | Applications | 0 |
| | 6.4 | Outlook | 0 |
| Ar | nex | 6- | 4 |
| | Α | Material Model Parameters | 5 |
| | В | Material Cards | ۲ |

List of Figures

| 1.1 | lage [7] | 1 |
|------|---|----|
| 2.1 | Example plot of energy absorption (storage) and Dissipation [17] | 4 |
| 2.2 | Stages of an exemplary crash sequence on a Load-Displacement plot [21] | 5 |
| 2.3 | Detail of a Kelvin Cell and lattice with parameters [5] | 6 |
| 2.4 | Non-auxetic (left) and auxetic structure (right) [14] | 7 |
| 2.5 | Classification of various 2D and 3D concepts for auxetic lattice structures [6, 10, 17, | |
| | 20, 15] | 7 |
| 2.6 | Example of an energy-absorbing structure for head protection in a vehicle crash [26]. | 8 |
| 2.7 | Chiral infill morphing airfoil concept by Paolo Bettini et al.[2] | 9 |
| 2.8 | Visual description of the process stages in High Speed Sintering (HSS) manufacturing | |
| | [28] | 10 |
| 2.9 | VX200 HSS printer at the DLR Institut für Fahrzeugkonzepte in Stuttgart | 10 |
| 2.10 | Stair stepping effect on the surface of 3D prints due to layer thickness | 11 |
| 2.11 | Tensile 1BA specimen geometry | 12 |
| 2.12 | Simulation workflow with LS-DYNA | 13 |
| 2.13 | Illustrative plot of Failure Strain against Triaxiality, including stress orientation | 17 |
| 3.1 | Chart of common thermoplastics (light blue) and thermosets (dark blue) | 19 |
| 3.2 | Infrared lamp sliding over the printbed | 21 |
| 3.3 | Manual postprocess of the 3D printed specimens | 21 |
| 3.4 | Sandblasting assisted cleanup | 22 |
| 3.5 | Airbrush painting process | 23 |
| 3.6 | Stochastic pattern on a specimen | 23 |
| 3.7 | Data Image Correlation (DIC) system setup used in the tests with two cameras and | |
| | four lamps. | 24 |
| 3.8 | Image from Istra4D. The red dot marks the origin, the others define the direction of | |
| | each axis | 24 |
| 3.9 | A PA12 specimen on the fixture | 25 |
| 3.10 | True Strain vs True Stress curve for PP | 26 |
| | Enter Caption | 27 |
| | Original, correction, and corrected compression curves | 27 |
| 3.13 | Plot of cross-sectional area as a function of vertical displacement with measurements | |
| | for PP | 28 |
| 3 14 | Compression curve for PP with yield calculation | 29 |

| 3.15 | with different printing orientation | 30 |
|------------|--|----|
| 3.16 | | 31 |
| | Compression stress-strain curve for the materials of the study. | 32 |
| 4.1 | 1 6 | 35 |
| 4.2 | Energy plot for the tensile simulation of PA12 | 36 |
| 4.3 | Tension (left) and compression (right) validation for TPU | 36 |
| 4.4 | Tension (left) and compression (right) validation for PP | 37 |
| 4.5 | Tension (left) and compression (right) validation for PA12 | 37 |
| 4.6 | Reentrant cell parameters [29] | 39 |
| 4.7 | Grid of permutations in size and thickness for the reentrant unit cell | 40 |
| 4.8 | Kelvin Cell Computer-Aided Design (CAD) | 40 |
| 4.9 | Four-node tetrahedron element [24] | 41 |
| 4.10 | Detail of the meshing of a reentrant cell | 42 |
| 5.1 | Strain field and Unit Cell (UC) detail before and after failure for the baseline 3D | |
| | | 46 |
| 5.2 | Comparison of (a) stress field evolution and (b) triaxiality behaviour in the 3D Reentrant cube | 45 |
| - 0 | | 47 |
| 5.3 | Crushing progression of the TPU 3D reentrant structure | 47 |
| 5.4 | Comparison between (a) experimental and (b) numerical simulation validation results. | |
| 5.5 | Experimental and numerical comparison of the force response | 48 |
| 5.6 | Comparison between (a) force–displacement behaviour and (b) SEA–displacement | 40 |
| - <i>-</i> | | 49 |
| 5.7 | Stress contours at 10mm displacement for the 0° structure (left) and the 90° structure (circle) | |
| - 0 | | 50 |
| 5.8 | | 50 |
| 5.9 | • | 51 |
| | Performance comparison for different relative thicknesses | 52 |
| | Force-displacement behaviour for different relative thicknesses | 52 |
| | Performance comparison for different polymers | 53 |
| | Last frame (d=0mm) of the dissipation simulation for the three materials of the study. | 54 |
| 5.14 | Force-Normalized displacement curves for the visualization of dissipated and stored energy of a 3D reentrant structure with the three materials of the study | 54 |
| 5 15 | Breakdown of SEA—displacement behaviour for the three materials | 55 |
| | Contours of stress of a 2D honeycomb structure under crushing | 55 |
| | Performance comparison between 3D and 2D structures | 56 |
| | Contours of stress of a Kelvin Cell structure under crushing. | 57 |
| | Performance comparison of 3D auxetic and non-auxetic structures | 57 |
| | A first PA12 print fail caused by the recoater dragging one of the parts | 59 |
| J. 1 | The transfer of the recourse drugging one of the pure. | , |

List of Tables

| 3.1 | Compilation of mechanical properties from literature [1] | 20 |
|-----|--|----|
| 3.2 | Relevant parameters used for the DIC | 24 |
| 3.3 | Mechanical properties of TPU, PP, and PA12s from experimental data | 31 |
| 4.1 | RMSE values for compression and tension validation of TPU, PP, and PA12 | 38 |
| 4.2 | Definition of lattice design parameters with corresponding symbols, units, and values. | 39 |
| 4.3 | Hardware specifications for the local computer and the workstation | 43 |
| 5.1 | RMSE of SEA between material models 024 and 124 | 49 |
| 5.2 | Effect of loading orientation on SEA, PCF, and MCF | 51 |
| 5.3 | Influence of base size on SEA, PCF, and MCF | 51 |
| 5.4 | Effect of relative thickness on SEA, PCF, and MCF | 53 |
| 5.5 | Comparison of SEA, PCF, and MCF for the polymer materials of the study | 53 |
| 5.6 | Energy distribution in different polymer materials | 55 |
| 5.7 | Comparison of 3D and 2D structures in terms of SEA, PCF, and MCF | 56 |
| 5.8 | Comparison of structural configurations and their compressive performance | 57 |
| 1 | Summary of parameters in the 3 material models considered for the study | 65 |

Acronyms

AM Additive Manufacturing. 9, 11, 19, 30, 32

CAD Computer-Aided Design. ix, 40, 41

CFE Crush Force Efficiency. 5

DIC Data Image Correlation. viii–x, 22–28, 30

DoF Degree of Freedom. 44

FDM Fused Deposition Modelling. 9

FE Finite Element. 11, 17

FEA Finite Element Analysis. 12

FEM Finite Element Method. 33, 41

HSS High Speed Sintering. viii, 10, 11, 17–19

HVLP High Volume Low Pressure. 23

MCF Mean Crushing Force. 5, 45, 52, 53

MJF Multi Jet Fusion. 10

PA12 Polyamide 12. 19, 20

PCF Peak Crushing Force. 5, 8, 45, 48–50, 52, 53, 57

PP Polypropilene. 19, 20, 26

RMSE Root Mean Square Error. 38, 48

SEA Specific Energy Absorption. 4–6, 9, 18, 20, 30, 39, 49, 50, 53, 55, 56

SLA Stereolitography. 9

SLS Selective Laser Sintering. 9

TPMS Triply Periodic Minimal Surface. 9

хi

TPU Thermoplastic Polyurethane. ix, 19, 20, 30

UC Unit Cell. ix, 6, 16, 39, 40, 42, 46, 47, 51

UTM Universal Testing Machine. 12, 23, 25, 27, 36

VEA Volumetric Energy Absorption. 4

Nomenclature

| \ddot{u} | Acceleration vector |
|-----------------------|-------------------------------|
| Δh | Change in height |
| Δt | Time step |
| Δt_{cr} | Critical time step |
| Δt_{max} | Maximum implicit time step |
| $\dot{arepsilon}$ | Strain rate |
| \dot{u} | Velocity vector |
| η | Triaxiality parameter |
| ν | Poisson's ratio |
| ρ | Density |
| σ | Stress |
| $\sigma_1, \sigma_2,$ | σ_3 Principal stresses |
| σ_{eng} | Engineering stress |
| σ_{true} | True stress |
| σ_{UTS} | Ultimate tensile strength |
| $\sigma_{y,c}$ | Yield strength in compression |
| $\sigma_{y,t}$ | Yield strength in tension |
| θ | Reentrant angle |
| ε | Strain |
| ε_a | Axial strain |

Elongation at break

 ε_b

xiii

Transverse strain **Engineering strain** ε_{eng} Effective plastic strain $\varepsilon_{pl_{eff}}$ True strain ε_{true} A(h)Cross-sectional area as a function of height Original cross-sectional area A_0 Base size of the unit cell b_{size} Speed of sound in material cNumber of cells per side of the cube Diameter as a function of height d(h)Original diameter d_0 E_c Young's modulus in compression E_t Young's modulus in tension Energy absorbed E_{abs} Dynamic friction coefficient f_d Static friction coefficient f_s Experimental force F_{exp} F_{ext} Vector of external forces Simulated force F_{sim} Original height h_0 Smallest element length in mesh l_{min} N_1, N_2, N_3, N_4 Shape functions for tetrahedral element r, s, t Natural coordinates for tetrahedral element Original radius r_0 Thickness as percentage of base size t_{bs}

Original volume

 V_0

xiv

A Area

C Strain rate parameter (Cowper-Symonds)

CFE Crush Force Efficiency

d Diameter

E Young's Modulus

F Force

H Unit cell height

h Height/specimen height

K Stiffness matrix

L Unit cell length

M Mass matrix

m Mass

MCF Mean Crushing Force

P Strain rate parameter (Cowper-Symonds)

PCF Peak Crushing Force

RMSE Root Mean Square Error

SEA Specific Energy Absorption

t Strut thickness/time

u Displacement vector

V Volume

VEA Volumetric Energy Absorption

X۷

1 Introduction

1.1 Motivation

Both energy absorption and dissipation are properties of great interest in engineering, particularly regarding the crashworthiness of vehicles. Understanding the mechanisms behind them can help improve the design of structures that preserve their functionality while enhancing their performance in dynamic loading scenarios like a crash or an impact, which has the potential to improve safety in road, rail, and air transportation.

The search for lightweight and crashworthy structures has become increasingly critical in modern engineering. The optimization of aircraft structures like the fuselage section in Figure 1.1 is an example of such advancements in an industry with strict safety regulations, environmental concerns, and increasing performance requirements like aviation.

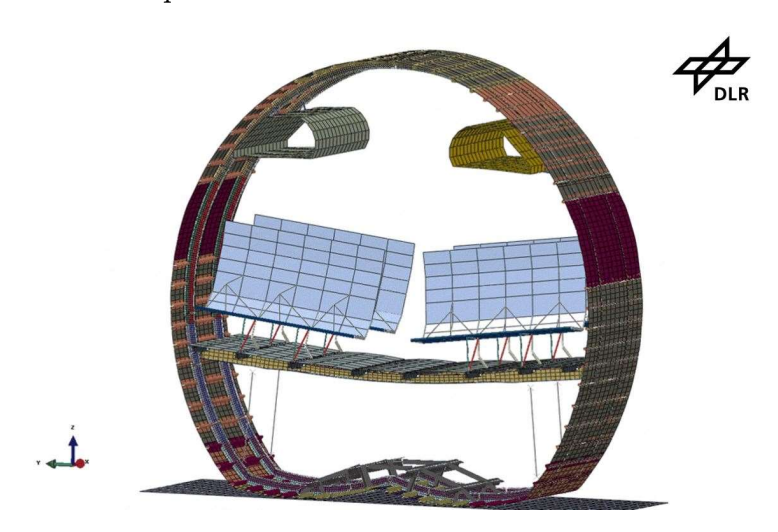


Figure 1.1: Crash concept with energy absorption by tensile loads for a new CFRP aircraft fuselage [7].

The evolution of additive manufacturing technologies has opened the opportunity for novel complex internal geometries that were previously impossible to produce using conventional manufacturing methods. Auxetic materials, characterized by a negative Poisson's ratio, are a particularly intriguing type of engineered structures that offer a completely alternative material behavior. Auxetic structures expand perpendicular to the applied load, creating unique deformation mechanisms.

The integration of auxetic geometries with additive manufacturing presents many opportunities but also complex challenges. While 3D printing enables the fabrication of structures with intricate internal features, the layer-by-layer deposition process introduces material anisotropy and other side effects that can substantially influence mechanical performance. The lack of a validated simulation framework specifically adapted to 3D printed auxetic structures limits their assessment for

1

energy absorption applications, particularly when considering the nonlinear material behaviour, the progressive failure mechanisms, and the contact interactions that dominate the crushing sequence.

1.2 Approach

This research aims to address the identified challenges through an experimental and numerical investigation on additive manufacturing and crashworthiness performance.

The approach begins with a systematic material characterization campaign of additively manufactured polymers. The characterization involves tensile and compressive loading conditions, with particular attention to the manufacturing orientation dependencies that influence structural performance. Advanced measurement techniques, including Digital Image Correlation (DIC), are used to capture true strain distributions and provide highly reliable data for the calibration of the material models.

The experimental characterization is directly fed into the development of numerical models within LS-DYNA, a finite element analysis platform with proven crashworthiness simulation capabilities. A particular interest lies in triaxiality-dependent properties, since auxetic structures subject elements to complex multiaxial stress states.

Finally, the approach includes a critical assessment that compares auxetic structures against other well-established energy-absorbing architectures using consistent metrics and loading conditions to provide direct performance comparisons.

Through this systematic approach, the research aims to establish a validated methodology for predicting the crashworthiness performance of additively manufactured auxetic structures, enabling large parametric studies that would be too expensive to be conducted experimentally.

2 Fundamentals

As a first step, this chapter includes a literature review with the purpose of synthesizing existing research that can be relevant to this thesis. Including conceptual foundations, definitions, as well as experimental and numerical methodologies.

2.1 Energy Absorption and Dissipation

Energy absorption is a process by which a physical material or structure stores energy from an external source. In the context of this thesis, the origin of this external energy is the force exerted on a structure. For example, during a collision or an impact.

Energy dissipation is another closely related physical process that describes how the energy entering a mechanical system spreads and transforms, rather than being retained and transferred.

Materials have different mechanisms to absorb and dissipate energy:

- **Plastic deformation**: Irreversible deformation resulting from the conversion of the input energy into strain energy.
- **Fracture and fragmentation**: Cohesive failure of the material leading to the creation of new facets.
- **Viscoelasticity**: Some materials, like polymers, can dissipate energy as heat through molecular motion and relaxation.

Figure 2.1 shows a typical example of a structure's Force-Displacement curve during a crash. The initial slope can be tied to the elastic regime of the material. which reaches a local peak force before permanently and progressively deforming and/or failing. The area under this curve is the sum of the energy stored in the structure as potential energy and the dissipated energy through the previously mentioned mechanisms.

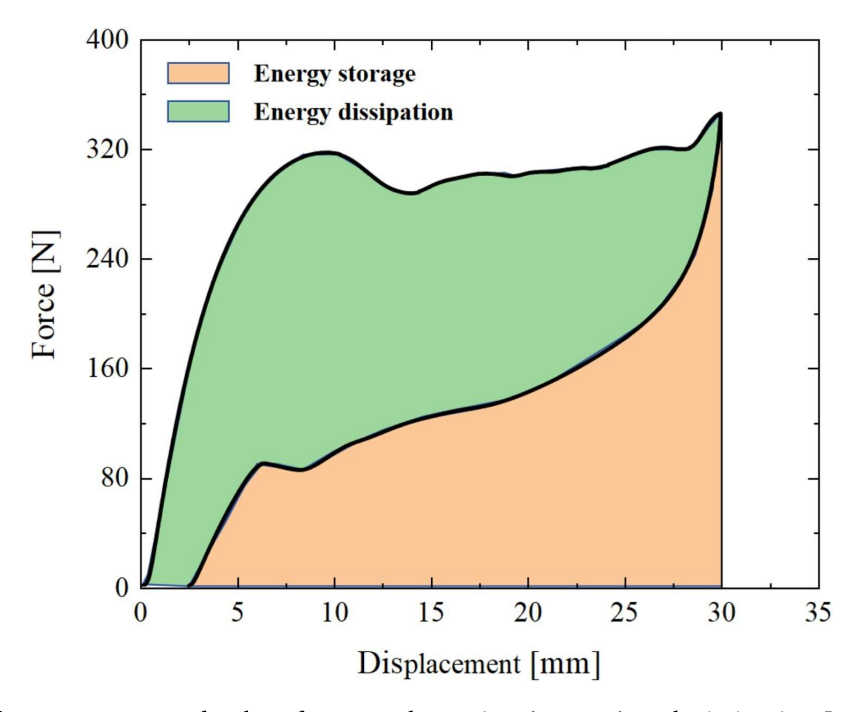


Figure 2.1: Example plot of energy absorption (storage) and Dissipation [17].

In a second stage, the force is completely removed from the structure, which now acts as a spring, recording a reversed Force-Displacement curve describing only the portion of energy that was not dissipated during the first phase.

A frequent optimization problem in the engineering area of crashworthiness is to preserve the absorption capacity while reducing weight, and that is why Specific Energy Absorption (SEA) is widely used for comparisons among different design choices.

$$SEA = \frac{E_{abs}}{m} \tag{2.1}$$

Where:

- E_{abs} is the energy absorbed in J.
- *m* is the mass of the structure in kg.

A definition [21] that justifies the necessity to evaluate crash performance not just based on the ability to absorb energy, but also by comparing it to the structural mass required for it.

For comparison between structures composed by the same material, or by similarly dense materials, a parameter normalized to the volume occupied by the structure is a suitable alternative to SEA. Especially in cases where the research focuses on infill patterns, typically expressed volumetric percentages, introducing the concept of Volumetric Energy Absorption (VEA)

$$VEA = \frac{E_{abs}}{V} \tag{2.2}$$

Where V is the volume of the structure in m^3 .

These two parameters alone are a relevant performance metric in crash scenarios, but are insufficient to describe the complete behaviour. A more detailed view of the Force-Displacement plot depicted in Figure 2.2 illustrates how the structure responds during the crash, and reveals a higher complexity of the sequence.

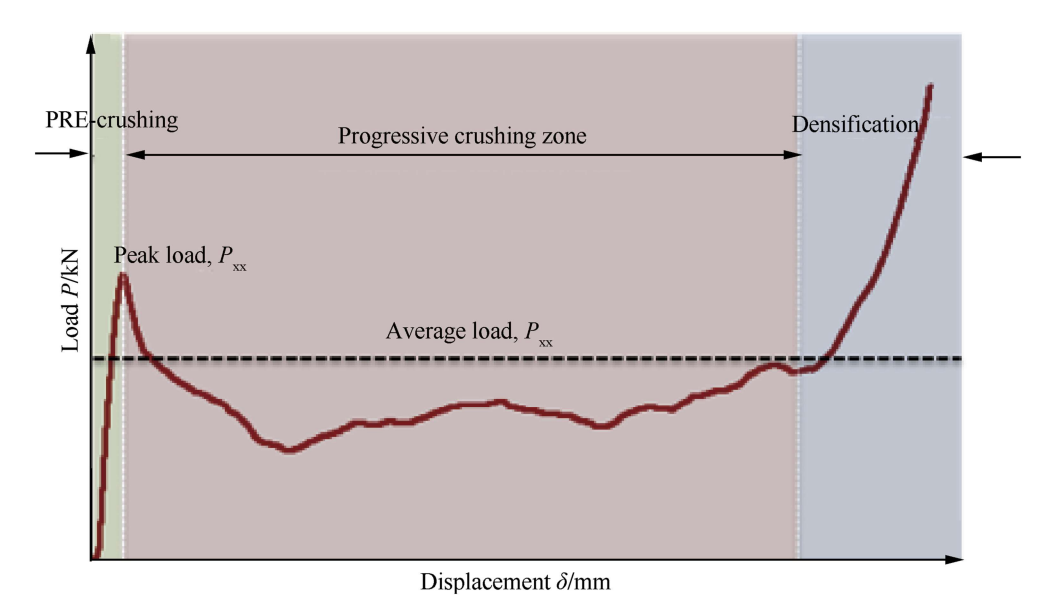


Figure 2.2: Stages of an exemplary crash sequence on a Load-Displacement plot [21].

Four main stages can be identified:

- 1. **Pre-Crushing**: The first part of the curve, representing the phase where the structure deforms elastically, and therefore mostly reversibly (with a low energy dissipation). Force increases proportionally to displacement.
- 2. Peak Crushing Force (PCF): The structure reaches a point where it can no longer deform purely elastically, which results in local maxima that can be tied to buckling, failure, or local yield of the structure. In terms of crashworthiness for transport vehicles, a high initial peak force is often undesirable for occupant safety, since it can lead to potentially harmful accelerations.
- 3. **Progressive Crushing (Plateau Region)**: the curve levels out and the force remains relatively constant as the structure progressively collapses. This is where, ideally, most energy absorption should occur, since a spread of the dissipation across a larger displacement implies a more gradual process that is not concentrated in a very short time span, again preventing dangerously high accelerations. Here, the concept of Mean Crushing Force (MCF) is introduced, representing the average force over the plateau region. And the ratio of PCF to MCF also serving as a relevant crash performance metric: Crush Force Efficiency (CFE).
- 4. **Densification**: As the structure continues to crush, the material becomes more and more tightly packed, and force increases sharply as the original geometry turns into a solid slab. The sudden increase in loads during this stage creates a non-ideal environment for energy absorption. One of the design goals for crash structures is to minimize the contribution of densification to total energy absorption, as the SEA is typically calculated by excluding it [8], a method referred to as "onset of densification".

5

2.2 Lattice Structures

Lattice structures are three-dimensional frameworks composed of the repetition of a UC. They are connected to each other, typically arranged in a regular pattern, and represent a recurrent choice for research of novel lightweight component design concepts. unit cell is composed by nodes and struts connecting them. Figure 2.3 shows an example of a Kelvin Cell lattice with a highlighted UC, and a detail of its different elements. Lattices open the possibility for the customization of mechanical, thermal, and even acoustic properties by fine-tuning their geometry. And Kelvin Cells in particular have been repeatedly studied due to their potential for energy absorption and dissipation[4].

Many different architectures exist, ranging from other periodic lattices such as honeycombs, cubic, or octet-truss, to stochastic structures defined by random arrangements or even functionally graded lattices where mechanical properties vary spatially to achieve a specific target behaviour.

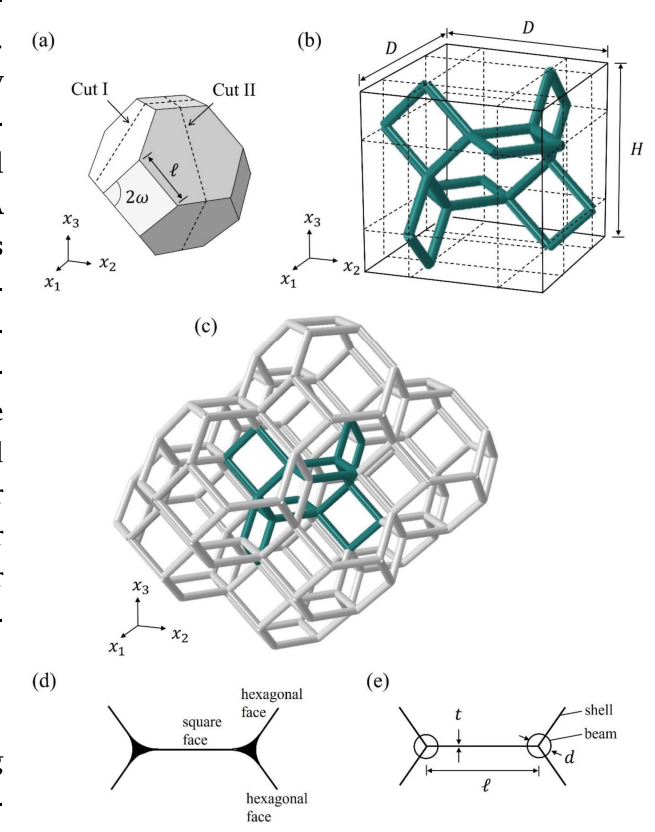


Figure 2.3: Detail of a Kelvin Cell and lattice with parameters [5].

A crucial differentiation among engineered lattice structures is whether their UCs are bending-dominated or stretch-dominated when under loading, since this defines their mechanical behavior:

- In **bending-dominated** lattices, such as Kelvin Cell networks, deformation under load is mainly defined by the bending of struts around the nodes. This mechanism results in a relatively low stiffness and strength, but it allows for large strains and a soft initial response, which makes bending-dominated lattices suitable for impact mitigation and cushioning, effectively reducing peak forces upon impact.
- **Stretch-dominated** lattices are designed so that most of their struts carry axial loads under tension or compression, which leads to a higher stiffness, strength, and SEA when compared to bending-dominated types [9], making them a more suitable option for impact and crashworthiness applications.

The choice between them implies a fundamental trade-off that must be considered according to the specific use case.

2.3 Auxetic Structures

Poisson's ratio is a fundamental material property that describes the ratio between axial and transverse strains in a stressed material.

It quantifies contraction (or expansion) in the direction perpendicular to the load application, and it is defined as:

tion (or expansion) in the lar to the load application,
$$= -\frac{\varepsilon_t}{\varepsilon_a} \qquad (2.3)$$

Where:

- ε_t is the transverse strain
- ε_a is the axial strain

Figure 2.4: Non-auxetic (left) and auxetic structure (right) [14].

Auxetics, from the Greek $\alpha \dot{u} \xi \eta \tau \kappa \dot{o} \varsigma$ (auxetikós), "that which tends to enlarge" are a variety of engineered structures defined by a negative Poisson's ratio. This concept can be traced back to Poisson's work in the 19th century, but it was not until 1987 that Rodney S. Lakes [16] documented the first experimental demonstration of a re-entrant polyurethane foam. The term auxetic itself was later introduced in the early 1990s by Ken Evans [12] in a Nature article, establishing the groundwork for contemporary research in auxetic materials. Unlike conventional materials, auxetics expand when stretched and contract when compressed, as shown in Figure 2.4.

| | Re-entrant | Rotating Rigid | Chiral |
|----|------------|----------------|--------|
| 2D | | OK. | |
| 3D | ** | | |

Figure 2.5: Classification of various 2D and 3D concepts for auxetic lattice structures [6, 10, 17, 20, 15].

This behavior is the result of the mechanics of microstructural geometries such as re-entrant shapes, rotating units, or chiral layouts, which collectively enable this special property. Over years of re-

search, diverse architectures with a negative ν have been discovered. Figure 2.5 summarizes the most relevant families of 2D and 3D structures.

Re-entrant cells are the most widely studied type, characterized by inward-pointing ribs that unfold under tension, while the rotating rigid family consists of connected units that rotate relative to each other, leading to large deformations, and chirals achieve auxeticity with node—ligament structures with twisting of circular nodes that produces a lateral expansion. 2D variants have the advantage of simpler manufacturability and analysis. Their 3D counterparts offer a more orthotropic behavior and a reduced weight for the same infill volume.

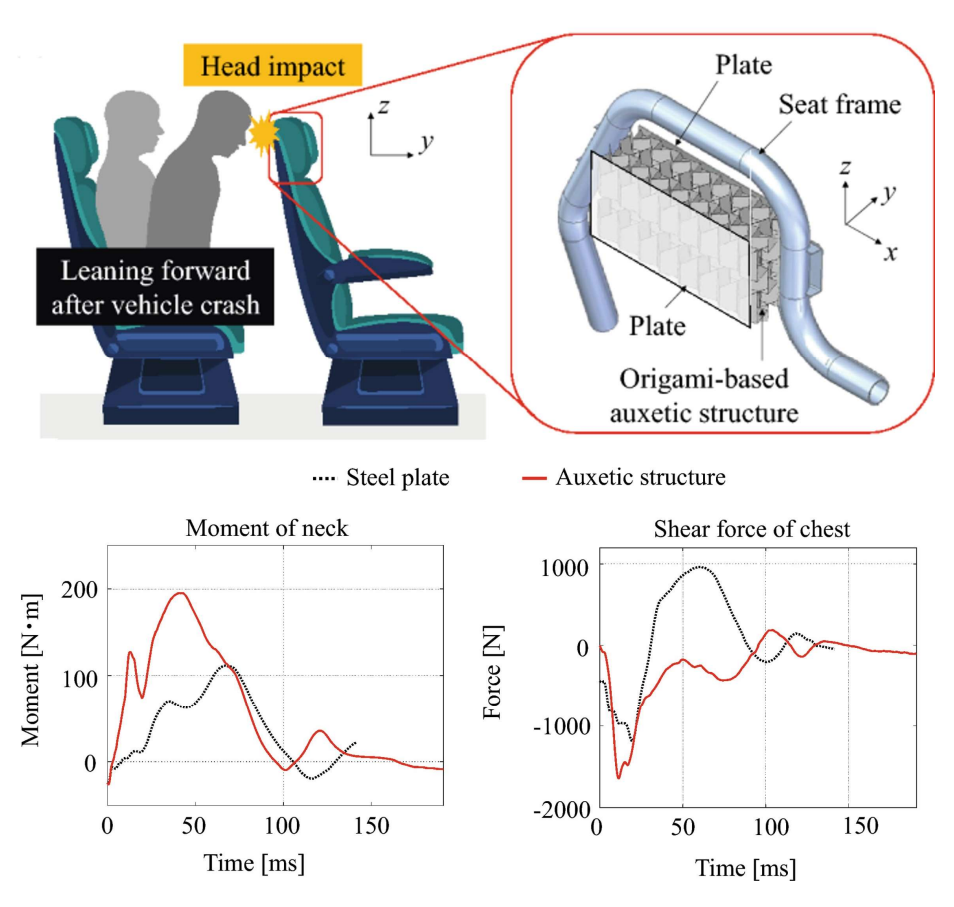


Figure 2.6: Example of an energy-absorbing structure for head protection in a vehicle crash [26].

The unusual behavior of auxetics has the potential to distribute stresses more evenly and to avoid stress concentrations that can lead to premature failure, increasing the deformation volume during energy absorption, which can allow the structure to absorb and dissipate more kinetic energy before failure. By tuning individual parameters, the densification phase can be shifted or mitigated, the plateau regions enlarged, and the energy absorption maximized [20].

A recent study by Sunao Tomita et al. [26] demonstrated the potential for vehicle crash protection by implementing a crushable auxetic headrest as shown in Figure 2.6. It achieves an initial soft regime that mitigates PCF upon head contact, followed by a stiffer regime providing energy absorption through continued deformation. Sled testing in real vehicles confirmed significant improvements in occupant safety when compared to conventional plate headrests, reducing the Head Injury Criterion (HIC) from 274 to 155.

The compliant nature of some polymer auxetics also enables multiple use cases for deformable structures and "print in place" 3D printed mechanisms. Figure 2.7 demonstrates a morphing airfoil using a chiral core, allowing it to adopt an optimal shape according to the flight conditions.

For these reasons, auxetic lattices are considered to be promising tools for innovation in applications like vehicle crash absorbers, aerospace components, protective gear, and even biomedical implants.

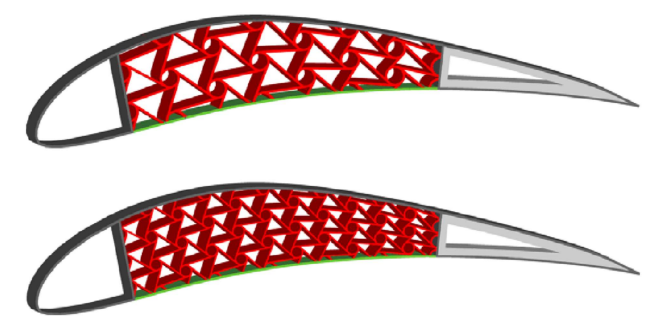


Figure 2.7: Chiral infill morphing airfoil concept by Paolo Bettini et al.[2].

In this thesis, the main focus will be on 3D re-entrant configurations, an architecture with precedents of enhanced SEA capabilities by fine-tuning of their multiple geometric parameters [25]. With the added dimension of a multi-material consideration, and a critical comparison against other non-auxetic, well-performing lattices, as well as their two-dimensional analogs.

2.4 Additive Manufacturing

Additive Manufacturing (AM), commonly referred to as 3D printing, is a range of manufacturing processes by which components are fabricated layer by layer from a virtual model. In contrast to conventional subtractive or formative methods, AM opens the possibility of manufacturing highly complex parts with minimal material waste and is particularly important for the production of auxetics, as well as other lattices and Triply Periodic Minimal Surface (TPMS) structures.

Their characteristic thin struts, overhangs, and void features are often not possible or too expensive to recreate using traditional methods like machining or plastic injection. But building objects slice by slice allows the placement of temporary support material that can hold overhang structures and fill the empty volumes during the printing process. Several 3D printing technologies exist:

- Fused Deposition Modelling (FDM): a widely used, low-cost technology where a thermoplastic filament is melted and extruded through a moving nozzle to form layers made of consecutive strings. FDM is easy to use and versatile in material choice, but it suffers from relatively low resolution and problematic internal support removal, so is therefore discarded as an option for auxetic manufacturing.
- Stereolitography (SLA) is one of the earliest AM technologies; its principle is the curing of a liquid photopolymer resin, layer by layer, by using a UV source. It produces parts with very high resolution and smooth surface finishes, but it is limited to photopolymer materials with moderate mechanical performance, a compromise that collides with the objective of attaining good energy absorption.
- **Selective Laser Sintering (SLS)** fuses powdered polymer layers with a high-power laser. The unmelted powder acts as a support structure and can be removed after the printing process. It

can produce parts with good mechanical properties, at the expense of a more porous surface finish. A good candidate for the production of all sorts of lattice structures, but an expensive service that would have to be externalized.

• **High Speed Sintering (HSS)** follows a similar principle: first, a thin layer of polymer powder (such as PA12, PP, or TPU) is deposited, then an inkjet printhead selectively applies an infrared-absorbing ink to the regions to be sintered. Infrared radiation melts the covered regions while leaving unprinted areas loose, and the process, represented in Figure 2.8 is repeated layer by layer until the completion of the object. **Multi Jet Fusion (MJF)**, developed by HP, also follows this same principle.

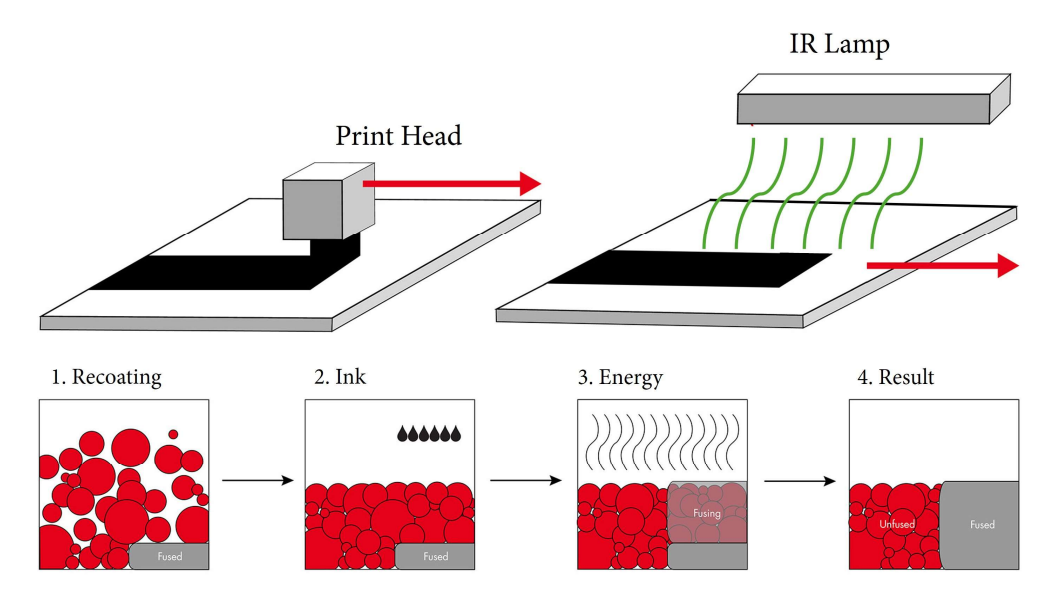


Figure 2.8: Visual description of the process stages in HSS manufacturing [28].



Figure 2.9: VX200 HSS printer at the DLR Institut für Fahrzeugkonzepte in Stuttgart.

HSS is the technology employed in this study due to availability and versatility for printing with high-performance materials of radically different properties. The printer used in this research, the VX200 HSS (Figure 2.9), offers a build space of $290 \times 140 \times 180$ mm, adjustable layer thickness above $80 \mu m$, a medium grain size range of $55 \mu m$ to $1 \mu m$, and a resolution of $360 \mu m$ dpi in the x-y plane. This configuration provides good resolution, and the manufacturer claims mechanical properties comparable to injection molding, which will later prove inaccurate for the used setup.

Despite the great impact of printing parameters on the resulting parts, which will be further discussed in Chapter 3, there are many advantages to this method when compared to conventional

manufacturing techniques. The flexibility of the process results in very short production times giving the option to print parts on demand, and the geometrical complexity of auxetic lattices comes at no additional cost.

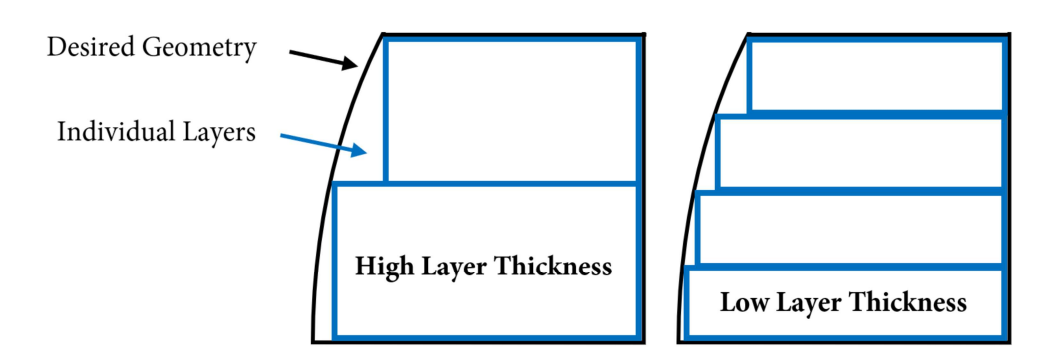


Figure 2.10: Stair stepping effect on the surface of 3D prints due to layer thickness.

Like all AM processes, HSS is subject to a stair-stepping effect depicted in Figure 2.10 caused by finite layer thickness, which can have an impact on performance for applications such as crash absorbing structures, where behavior is geometry-sensitive and deviations from the CAD model should be avoided. Reducing layer thickness improves surface finish and prevents the appearance of stress concentrators that become potential failure points, but at the expense of increasing printing time, which limits the number of parts that can be inserted in the same print job, since the machine needs to be continuously monitored due to safety concerns. By taking these particularities into consideration, it was possible to produce surfaces that are suitable for functional testing of lattices without requiring intensive post-processing.

2.5 Testing Standards

Characterizing the mechanical properties of the 3D-printed polymers used to create the auxetics in this study is essential for understanding their suitability. This characterization is also necessary to obtain an accurate material model for a numerical study including Finite Element (FE) simulations. Internationally recognized standards such as ISO and ASTM are used for that purpose. They specify procedures, universal specimen geometries, and loading conditions for obtaining reliable and reproducible experimental data. The three procedures that provide enough data for general load case modeling are tensile, compression, and shear tests.

2.5.1 ISO 527: Tensile Testing of Polymers

ISO 527 standard defines the experimental procedure for determining tensile properties of polymer materials. It consists of the measurement of the force required to stretch a designated specimen until its failure, together with its elongation (strain).

The main results of this experiment are metrics such as tensile strength, Young's Modulus, yield point, and elongation at break, but it can also provide insights into the plasticity of each material,

which is critical in crash scenarios due to the large deformations sustained by the structures.

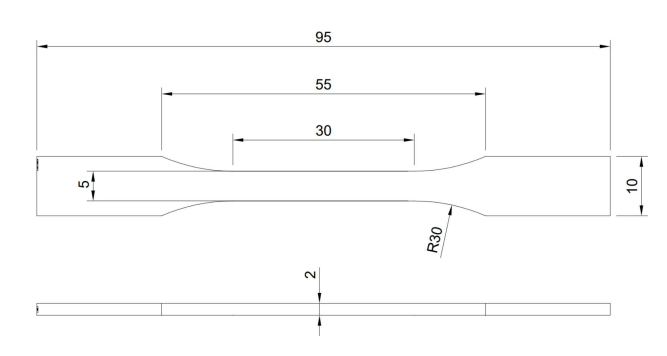


Figure 2.11: Tensile 1BA specimen geometry.

A multipurpose ISO 3167 Type 1BA specimen (Figure 2.11) is gripped in a Universal Testing Machine (UTM). This particular variant was chosen due to its reduced size compared to other standard test specimens like the 1A, which simplifies the manufacturing process by shortening the required height of the print job and therefore allowing for faster prints with a lower failure risk. The machine applies a uni-axial tensile force at constant speed. Testing at different speeds can provide information about

strain rate behaviour. An extensometer measures elongation, and a force sensor, usually piezoelectric, captures the load on the specimen.

2.5.2 ISO 604: Compression Testing of Polymers

ISO 604 sets the protocol for measuring compressive properties of rigid and semi-rigid thermoplastic and thermoset polymers. The test reveals the material's ability to withstand compressive loads. The specified procedure starts with the placement of the specimen, a cylinder of 4mm in height and 10mm in diameter, between two compression plates in a UTM. Compressive force is then applied axially until failure or another predefined parameter is reached. Due to the ductility of most polymers, this parameter is usually set as the upper limit of the force sensor in order to prevent damage to the testing equipment. The test provides compressive strength, compression yield stress, strain at yield, and compressive modulus.

2.6 Simulation in LS-DYNA

LS-DYNA is an advanced Finite Element Analysis (FEA) software developed to simulate the complex real-world behavior of structures under different load cases. It is widely used in research for its strong capabilities in nonlinear analysis, including highly dynamic scenarios such as crash and impact [31]. LS-DYNA allows for explicit and implicit time integration schemes and incorporates a library with over 200 different material models, which can also couple structural, thermal, and fluid domains, making it one of the most trusted tools for crashworthiness studies.

The overall simulation workflow in LS-DYNA is depicted in Figure 2.12. It involves a free preprocessing software (LS-PrePost), where cases can be configured by generating and editing meshes, imposing boundary conditions to the different geometries, selecting the desired contact definition between elements, and assigning among other options. All this information is then read by the solver, which performs numerical analysis according to the specified computational method, calculating strains, stresses and derived variables for every element of the mesh. LS-PrePost is again used as a postprocessor of the generated solution in the format of .d3plot and .binout files, which

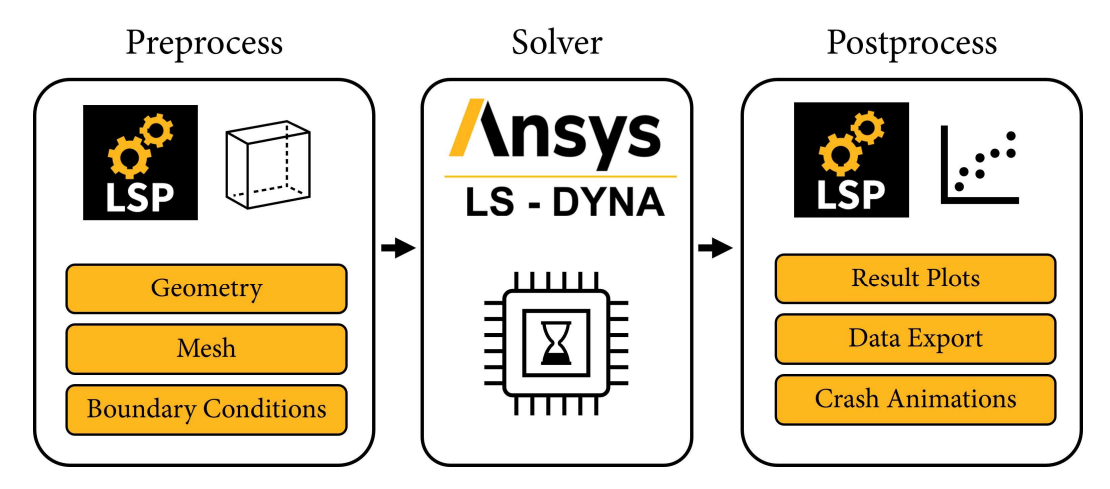


Figure 2.12: Simulation workflow with LS-DYNA.

respectively provide visualization of the results and multiple data extraction options for further analysis.

2.6.1 Implicit and Explicit Simulations

LS-DYNA solves the fundamental equations of motion for a deformable body [22]:

$$\mathbf{M}\ddot{u} + \mathbf{C}\dot{u} + \mathbf{K}u = \mathbf{F}_{\mathbf{ext}} \tag{2.4}$$

Where **M** is the mass matrix, **C** is the damping matrix, **K** is the stiffness matrix, \ddot{u} is the acceleration vector, \dot{u} is the velocity vector, u is the displacement vector, and \mathbf{F}_{ext} is the vector of external forces. This problem can be solved by following two distinct approaches:

Explicit schemes which use central difference time integration, update displacement and velocity directly. The system advances in time by calculating the acceleration response based on known forces and displacements from previous steps, avoiding costly iterative solutions at the cost of small timesteps to ensure stability.

$$\mathbf{u}_{n+1} = \mathbf{u}_n + \Delta t \dot{\mathbf{u}}_n + \frac{1}{2} \Delta t^2 \ddot{\mathbf{u}}_n$$

$$\dot{\mathbf{u}}_{n+1} = \dot{\mathbf{u}}_n + \frac{\Delta t}{2} (\ddot{\mathbf{u}}_n + \ddot{\mathbf{u}}_{n+1})$$
(2.5)

With a critical timestep Δt_{cr} governed by the Courant stability criterion [24]:

$$\Delta t_{cr} = \frac{l_{min}}{c} \tag{2.6}$$

Where l_{min} is the smallest element length in the mesh and c is the speed of sound in the material $(c = \sqrt{\frac{E}{\rho}})$, with E = Young's modulus and ρ = density. This restricts explicit analysis to small incremental steps, ideal for highly dynamic events.

Implicit schemes iteratively solve for displacements that satisfy equilibrium at each time increment:

$$\mathbf{K}\mathbf{u}_{n+1} = \mathbf{F}_{\mathsf{ext},n+1} \tag{2.7}$$

They allow for much larger timesteps which can reduce computing time, and are best suited for static or quasi-static analysis.

2.6.2 Suitability

Analytical models for the determination of periodic lattice behaviour range from Cosserat rods, to Timoshenko or Simo–Reissner beams. Theories that account for large deformations and rotation, but that are limited to the use of linear constitutive models and the assumption of undeformed cross-sections [30].

The prediction of energy absorption, failure modes, deformation patterns and force response of auxetics under dynamic loading needs a tool capable handling large deformations, a complex material model capable of capturing nonlinear plasticity and damage effects, as well as the consideration of contact mechanics. All of them are requirements that LS-DYNA fulfills.

The choice of solver depends on the particular characteristics of the structure, with large deformations expected at an early stage and a complex failure behavior at a later phase. A mix of implicit controls with an automatic switch to explicit after failure will later prove to be the optimal solution for reducing computational effort.

2.7 Material Models in LS-DYNA

A key aspect of simulation fidelity in LS-DYNA lies in the accurate selection and calibration of material models. These models define the stress–strain response of the material under different loading conditions, and are critical to ensure a reliable prediction [23]. In the case of auxetic lattice structures, where mechanical performance is governed by the nonlinear response at large strains and complex failure mechanisms, this is particularly relevant. The ability of LS-DYNA to reproduce plastic deformations and progressive damage through its constitutive models is essential for a realistic interpretation of energy absorption and crashworthiness.

Understanding the constitutive behavior behind the selected material models requires a brief review of fundamental material response types implemented in LS-DYNA. Linear elastic behavior represents the foundation of all material models, described by Hooke's law:

$$\sigma = \mathbf{E}\varepsilon \tag{2.8}$$

where stress σ is proportional to strain ε through the elastic stiffness tensor **E**. For isotropic materials, two independent parameters are considered: Young's modulus E and Poisson's ratio ν . This relationship governs the initial response in all the material models investigated.

Elastoplastic behavior extends beyond the elastic limit through the introduction of a yield criterion and plasticity, usually implemented through a piecewise linear hardening law:

$$\sigma_y(\varepsilon_p) = \sigma_{y0} + H\varepsilon_p \tag{2.9}$$

where σ_{y0} is the initial yield stress, H is the hardening modulus, and ε_p is the accumulated plastic strain. It can also be defined through a load curve (LC) with any given number of stress and effective plastic strain pairs.

The library of LS-DYNA offers a wide range of complexity, from linear elastic models to advanced formulations that incorporate viscoplasticity, failure criteria, and strain rate effects. For this study, two candidates are considered: MAT024 (Piecewise Linear Plasticity) and MAT124 (Plasticity Compression-Tension). These models differ in terms of assumptions and computational cost, but they share the ability to reproduce large strain plasticity and failure, which are the defined prerequisites for lattice-level simulations under crash loads.

The progression from MAT024 to MAT124 also reflects an increasing ability to capture the effects of property variations in different axis. There is a direct link between simulation and experimental characterization, which is particularly relevant because the selected models are designed to utilize multi-axial input data, and the tensile and compression tests to be carried out will provide the right dataset for calibration and validation.

2.7.1 *MAT_024

Among the many constitutive models available, *MAT_024 (*MAT_PIECEWISE_LINEAR_PLASTIC-ITY) is one of the most widely used elasto-plastic representations for its versatility and low demanding computational requirements. It allows to reproduce the measured plastic response of a material without restrictions to a single hardening law, and can accommodate a bilinear hardening description through the input of a tangent modulus or a complete stress–strain curve from a table of experimental datapoints.

An advantage of *MAT_024 is its ability to account for strain-rate effects, which improves accuracy for high load speed applications [27]. Several options are offered: user-defined scale curves, tabulated stress—strain curves, or a simple scaling of the yield stress using Cowper—Symonds factor:

$$1 + \left(\frac{\dot{\varepsilon}}{C}\right)^{1/p} \tag{2.10}$$

Where $\dot{\varepsilon}$ is the strain rate $\dot{\varepsilon} = \sqrt{\dot{\varepsilon}_{ij}\dot{\varepsilon}_{ij}}$

Failure can be included in *MAT_024 through a critical plastic strain criterion with the parameter "FAIL". Once reached the specified effective plastic strain, element erosion (removal of the element) takes place. This provides an approximation of material degradation and fracture, but it should be noted that the failure definition lacks other considerations like advanced damage accumulation or softening laws.

In the context of this study, *MAT_024 acts as an entry point. Its relative simplicity means it can be generated with results from a tensile test campaign alone. Allowing to establish a consistent baseline representation of the material at a low computational cost.

2.7.2 *MAT_124

The previously described option provides a general-purpose model, but it does not differentiate between tensile and compressive behaviour. For auxetic structures, this simplification can lead to a loss of detail of their response, because the UC geometry induces asymmetric stress states. *MAT_124 (*MAT_PLASTICITY_COMPRESSION_TENSION) offers the possibility to define two independent yield stress and plastic strain curves for tension and compression, with a smooth interpolation in the transition regime. This distinction is relevant to auxetic lattice architectures, where local bending generates different effective strengths under compression and tensile stretching.

Tension-compression asymmetric plasticity addresses the limitation of symmetric yield behavior through separate constitutive relationships. *MAT_124 implements this by defining independent yield for tensile and compressive states:

$$\sigma_y = \begin{cases} \sigma_{y,t}(\varepsilon_p) & \text{for } \sigma_m > 0\\ \sigma_{y,c}(\varepsilon_p) & \text{for } \sigma_m < 0 \end{cases}$$
 (2.11)

where $\sigma_m = \frac{1}{3} \text{tr}(\boldsymbol{\sigma})$ is the mean stress, and $\sigma_{y,t}$ and $\sigma_{y,c}$ are the tension and compression yield functions, respectively. This formulation captures the different mechanical responses observed in polymer materials under varying loadings.

Table 1 of Annex A provides a summary with details of the available input parameters for each of the proposed material models, giving an overview of the mentioned increase in complexity [23].

2.7.3 Selection Criteria: Triaxiality

Triaxiality is a dimensionless parameter that quantifies the relative contribution of hydrostatic stress to the equivalent stress state in a material:

$$\eta = \frac{1/3(\sigma_1 + \sigma_2 + \sigma_3)}{\frac{1}{\sqrt{2}}\sqrt{(\sigma_1 - \sigma_2)^2 + (\sigma_2 - \sigma_3)^2 + (\sigma_3 - \sigma_1)^2}}$$
(2.12)

Where σ_1, σ_2 and σ_3 are the components of stress in the three axis.

A key reason for employing stress triaxiality as selection criteria for material models is its ability to classify the predominant stress states within a given geometry [3]. Quantifying triaxiality in the auxetic structures of interest, allows to anticipate whether it is governed primarily by tension, bending (tension and compression), or shear. Figure 2.13 illustrates this logic over a failure strain curve.

If a numerical analysis reveals that the auxetic mostly experiences uniaxial tension, a simple model such as MAT_024 is sufficient. In case the geometry induces significant bending and local compression zones, the use of MAT_124 becomes more appropriate. An observed behaviour where the auxetic structure is subjected to complex multiaxial states with noticeable shear components, a more advanced model like MAT_187 (SAMP-1) is required. In this sense, a preliminary triaxiality

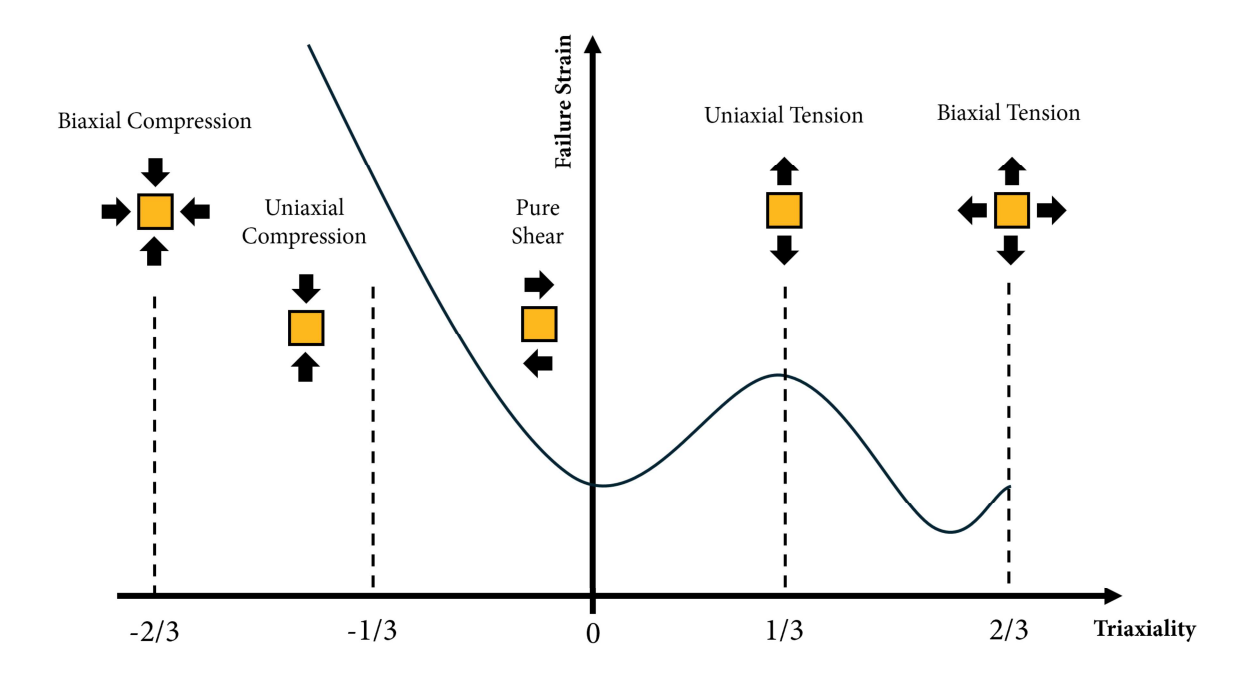


Figure 2.13: Illustrative plot of Failure Strain against Triaxiality, including stress orientation.

analysis of the lattice geometry will provide a rational basis for selecting the most computationally efficient material model without sacrificing accuracy.

2.8 Research Definition

From the reviewed literature, several conclusions can be drawn. It becomes apparent that no analytic method is universally capable of capturing the full nonlinear quality of auxetic lattices under large deformation. FE simulations remain irreplaceable tools for exploring their potential for energy absorption, despite their complexity and computational demand.

The design flexibility offered by additive manufacturing, particularly HSS, enables numerous possibilities to fabricate custom lattice geometries using thermoplastics. Identifying structural mechanisms that benefit from auxetic deformation to enhance energy absorption requires both experimental characterization for calibration of material models and numerical studies.

The primary objective of this thesis is to assess the potential of auxetic 3D printed structures for energy absorption and dissipation, and to understand which design variables and mechanisms influence these properties.

The scope is defined by:

- A familiarization with nonlinear finite element methods and material modelling in LS-DYNA.
- Experimental testing of specimens for multiple polymer materials, followed by calibration and validation of the selected material model.
- Development of a methodology for generating and simulating auxetic lattices.

- Numerical evaluation of different auxetic geometries under crash loads, with an assessment of their energy absorption and dissipation efficiency for crashworthiness applications.
- Design, manufacturing, and testing of representative structures using HSS, in order to validate the numerical results.

2.8.1 Hypothesis

The conclusions from the literature review carry over into the hypotheses. As it is common in studies on lattice structures, two divisions of hypotheses are formulated [9]. The first is concerned with the accuracy of material models in LS-DYNA applied to additively manufactured parts. The calibration and validation of these models through experimental data is necessary for a precise prediction of large-deformation response and energy absorption.

The second uses the previous tools to study how lattice design variables and auxeticity itself can influence energy absorption. The results are expected to show that the performance of a lattice is strongly related to their special topology, and that auxeticity could provide an advantage under certain circumstances.

A summary of the hypothesis for each of the two branches follows:

- 1. Material model fidelity in LS-DYNA:
 - a) The predicted force—displacement curves from calibrated LS-DYNA models should match experimental results within a reasonable accuracy for peak load and SEA.
 - b) A numerical analysis of triaxiality should reveal which material model complexity is required to reproduce global and local responses of auxetic structures.
- 2. Structural and design variables:
 - a) **Unit cell base size** is expected to have an influence on the deformation localization and on the different failure modes.
 - b) **Relative strut thickness**. There should be an optimal strut thickness as a percentage of base size offering the best SEA. Increasing thickness should lead to higher stiffness.
 - c) Material choice. Different thermoplastics should present distinct deformation profiles, since softer polymers can sustain large strains, while higher modulus candidates will fail earlier.
 - d) **Load application angle**. 3D re-entrant lattices loaded at 0° and 90° are expected to display distinct responses.
 - e) **3D** lattices have the potential to outperform **2D** counterparts in SEA due to the increase in accessible deformation modes.

3 Material Characterization

The following chapter describes the methodology used to characterize the polymer materials used to manufacture the auxetic structures of this study. It includes a description of the manufacturing process of the specimens, their preparation for testing, and the results of the test campaign, followed by their implementation as material cards for simulation.

3.1 Selection of Materials

The first step in the mechanical characterization was the definition of the base materials used for AM. Attributes such as modulus, plastic strain capacity, and failure strain play an important role in the determination of crash performance. Figure 3.1 shows density and tensile strength ranges for some of the most widely used polymer chemistries.

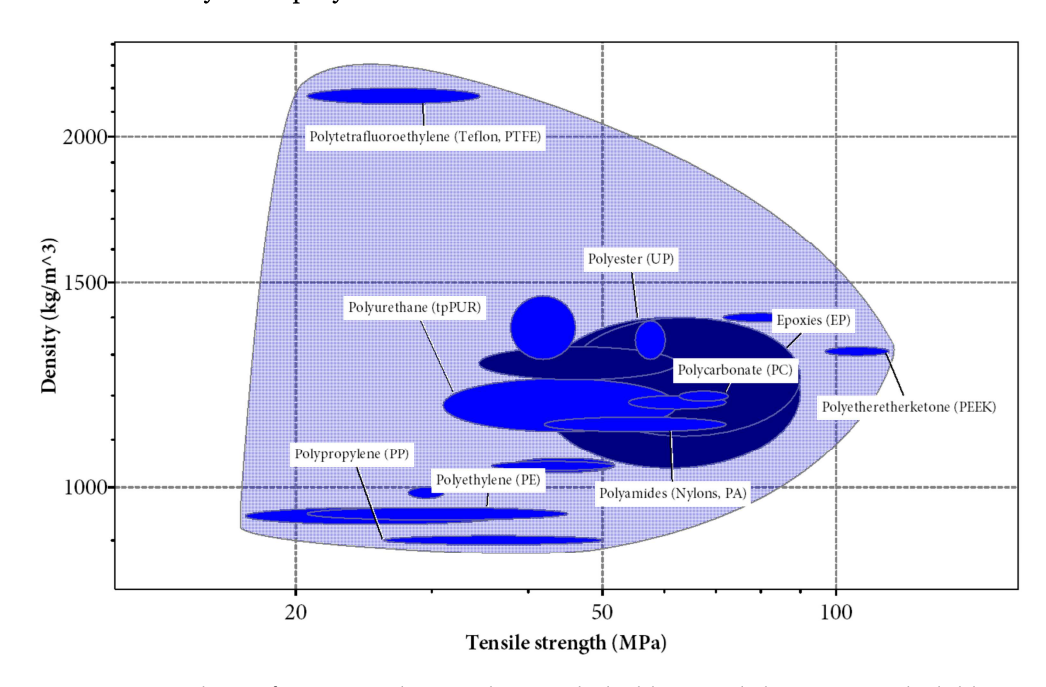


Figure 3.1: Chart of common thermoplastics (light blue) and thermosets (dark blue)

Among all the available options, three thermoplastic polymers were selected: TPU, Polypropilene (PP), and Polyamide 12 (PA12), more commonly known as Nylon. The choice was primarily made due to their compatibility with the HSS process chosen for this study, which provides the required design freedom for manufacturing complex lattices.

Beyond manufacturability, the selected materials provide a meaningful spectrum of mechanical behaviours that can influence their energy absorption and dissipation capacity. From Table 3.1 it can be seen that TPU is a highly ductile elastomer with relatively low modulus and high failure strain, which makes it a promising candidate for structures where energy absorption relies on large recoverable deformations, since it will behave in a mostly elastic regime throughout the crash. PA12, by contrast, is a high-performance polymer used in engineering applications due to a high elastic modulus and well-defined yielding behaviour. Despite a lower post-yield strain capacity compared to TPU, it has the ability to sustain higher stresses before failing. PP acts as a representative for an intermediate case, with moderate stiffness and significant plasticity, offering a middle ground to evaluate the dependence of SEA on material properties with more precision.

| | TPU | PP | PA12 |
|------------------------|-------------|------------------|----------------|
| Density [kg/m³] | 1120 - 1240 | 895 - 909 | 1120 - 1150 |
| Young's Modulus [GPa] | 0.1 - 1 | 0.824 - 1.02 | 0.94 - 2.04 |
| Yield Strength [MPa] | 8 - 15 | 24.1 - 28.4 | 39 - 64 |
| Tensile Strength [MPa] | 10 - 20 | 26 - 50 | 42 - 72 |
| Elongation [%] | 200 - 500 | 112 - 483 | 40 - 60 |

Table 3.1: Compilation of mechanical properties from literature [1].

This range of properties, from soft (TPU), to moderately ductile (PP), to stiff (PA12)—allows a systematic investigation of how material behaviour interacts with auxetic topology in governing the mechanisms of energy absorption and dissipation.

3.2 HSS Additive Manufacturing

The starting point for production is the conversion of the designed CAD files of the specimens into STL format. The files are oriented within the available build volume of 290 x 140 x 180 mm. The parts to print are tensile and shear coupons, compression cylinders, and sample lattice cubes. A slicing step translates the 3D geometry into two-dimensional cross-sectional layers according to the chosen layer thickness of $80\mu m$.

Although all parts can be manufactured in the same print job, special attention needs to be paid to the guidelines provided by the printer manufacturer in terms of object placement within the print bed. The heat irradiated from the melted cross sections can cause problems that should be easily prevented if a correct setup is achieved. Placing parts too close together, or too close to the walls, should be avoided. A specified maximum printed surface area of 128cm² per layer should also be respected, and a 40x40mm area should be left empty in the corner where the pyrometer head is placed.

Before each print, the machine is loaded with the selected polymer powder. Process parameters such as layer thickness or sintering energy are defined through the printer's control software. These parameters are material-dependent and need to be carefully adjusted to correctly adjust the bond of the subsequent layers, the accuracy of the prints as well as their surface finish. During the build,

a thin layer of polymer powder is spread across the build platform. An inkjet head selectively places a dark ink onto the areas that correspond to the parts cross-sections. The exposure to an infrared lamp then melts the regions to be printed, while the rest of the powder remains loose, acting as a natural support. Figure 3.2 shows the heating element moving over the powder bed. This layer-by-layer process is repeated until the complete part is built.

After completion of the print job, which took several hours, the printed parts remain embedded in a brick of relatively loose powder. In the next step, the surrounding powder is carefully removed by hand in a fume hood to avoid the inhalation of the fine particles. This procedure requires patience and attention to detail because the thin struts and cavities of some of the parts make access to some features challenging. Manual cleaning using brushes and special carving tools of various sizes and shapes, in several iterations, until most of the excess powder is removed or the remaining is not easily accessible. Figure 3.3a shows the state of the powder block after printing and the mate-

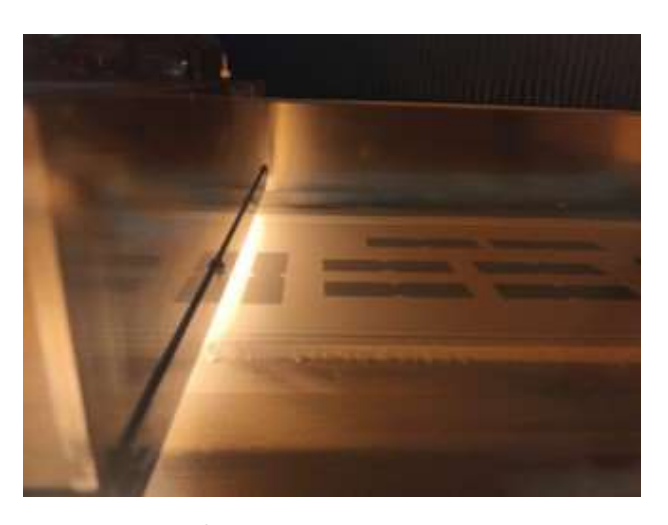


Figure 3.2: Infrared lamp sliding over the printbed.

rial crumbling, liberating the parts, and one of the gyroid specimens can be seen in Figure 3.3b after a first cleaning using brushes.

Following this step, the samples are transferred to a sandblasting station, where they are processed with pressurized air and fine and abrasive silica particles, removing the residual powder adhered to the surfaces, resulting in a more homogeneous finish. Sandblasting is the only practical method to reach deep or hidden channels and narrow cavities where powder can remain trapped after manual cleaning.



(a) Powder block containing all the printed parts.



(b) Cleanup of the PA12 powder from a gyroid cube.

Figure 3.3: Manual postprocess of the 3D printed specimens.

It is important to note that trapped powder could potentially affect the mechanical response and

the mass measurements, but at the same time, excessive exposure can gradually erode material from the surface of the actual parts. This effect is particularly critical in lattice structures, where the size of the struts is already small and often close to the resolution limit of the machine. Figure 3.4 depicts the process with lattice samples and with specimen coupons, for which a special tray was employed to facilitate the handling against the high-pressure air.

In addition to sandblasting, mechanical tumbling was also considered as an alternative for post-processing, exposing the parts to continuous agitation in a rotating drum with an abrasive material, gradually polishing the surfaces. While tumbling has the potential to reduce surface roughness, the confined internal volumes prevent uniform abrasive action, and it may even weaken thin struts through continuous collisions. For these reasons, it was ultimately discarded.





(a) Sandblasting of a lattice.

(b) Test specimens fixed on a dedicated tray.

Figure 3.4: Sandblasting assisted cleanup.

The final step of the post-processing is a visual inspection and a verification of the specimens' dimensions.

3.3 Characterization Techniques

A fundamental step in the development of an accurate numerical model is the mechanical characterization of the base materials. For this, a combination of tensile tests and compression tests was performed for each material, covering quasi-static tension and compression regimes. To obtain full-field strain data with the highest possible accuracy, all tests were performed with DIC, enabling the measurement of local deformations on the specimen surface and directly providing true strain data.

3.3.1 DIC

DIC is an optical method used for the measurement of strain fields on the surface of the specimens. It works by tracking the displacement of a random pattern recorded by two high-resolution cameras throughout the tensile or compression tests. As the specimen deforms, defined pixel groups of the image transform, and a comparison of successive images using cross-correlation algorithms reveals local displacements that can be calculated with sub-pixel accuracy. Unlike traditional extensometers, DIC is able to capture both homogeneous strain fields and localized strain, making it

an essential tool for the investigation of behaviours like necking or shear bands, which are expected in this study.

A prerequisite for the implementation of DIC measurements is the use of a stochastic surface pattern on the specimen with a high-contrast paint. The random pattern is used as a unique digital fingerprint for the correlation algorithm to recognize and track during its deformation. For this purpose, specimens were first coated with a thin, uniform base layer of matte white acrylic paint to create a homogeneous background, as shown in Figure 3.5. For the black speckle application, a SATAjet 100B airbrush with a High Volume Low Pressure (HVLP) system was used due to its ability to deliver fine



Figure 3.5: Airbrush painting process.

atomization, critical for producing non-overlapping speckles. Operating at a recommended inlet pressure of 2.0 bar and a painting distance of 15 cm allowed the tuning of droplet size with a target speckle size of 3–5 pixels in the DIC images. Care was also taken to avoid oversaturation of paint, which could lead to smeared or merged speckles that result in lower accuracy. Figure 3.6 shows the pattern achieved on the specimens and lattice cubes.



Figure 3.6: Stochastic pattern on a specimen.

Specimens are held against a cardboard piece, and masking tape is used to cover the tips to prevent sliding once in the grips of the UTM.

The DIC system used consists of two Baumer VCXU-123M, 12 megapixel monochrome cameras with 75mm 7528C lenses in combination with the Istra 4D software. Before each testing campaign, the system was calibrated using a target, ensuring that the cameras accurately reconstruct the displacement field from the stereo images by correcting for optical distortions. The calibration target contains a grid of markers with a known geometry that the DIC software uses to compute the camera parameters. For tensile specimens, a GL-04-WMB_9x9 calibration target was employed to match the field of view of the specimen during the entirety of the test. For compression specimens, with a diameter of only 10mm, a smaller GL-02-WMB_9x9 calibration target was used, allowing the cameras to focus on the smaller region of interest with higher pixel density.

Since tensile and compression tests were conducted at different strain rates, ranging from 5 to 500mm/min, the duration of the tests varied significantly, which has a direct impact on the DIC recording sequence. The temporal resolution must be high enough to capture the evolution of deformation without missing critical strain localization or failure. But

excessively high frame rates will increase data volume, leading to a longer processing time that does not necessarily improve accuracy.

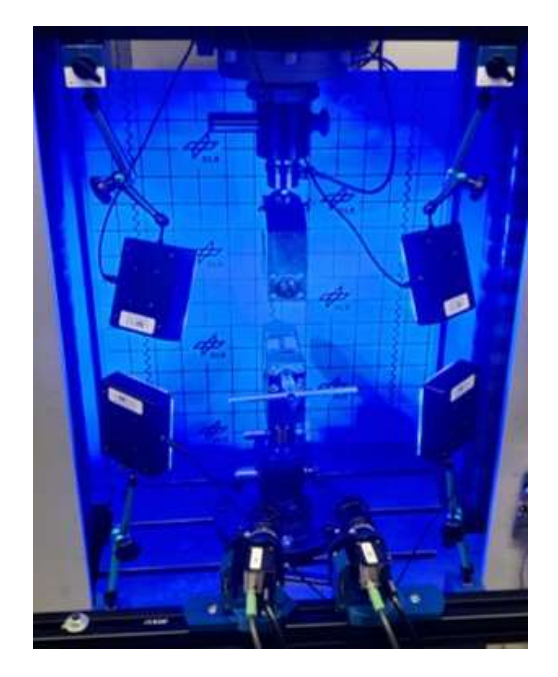


Figure 3.7: DIC system setup used in the tests with two cameras and four lamps.

To ensure a balance between an acceptable resolution with a manageable file size, a target of approximately 600–700 frames per test was To achieve this, two main acquisition parameters were tuned: camera clock frequency and frame decimation. For longer tests at low strain rates, the system was set to record every 10th frame at a lower frequency. For the adequate functioning of the DIC system, a bright and uniform lighting is required to ensure that the speckle contrast stays constant throughout the test. Four blue LED lamps were arranged symmetrically around the specimen as shown in Figure 3.7 (two above, two below, at oblique angles) in order to minimize shadows and overexposed areas.

A user-defined reference system was chosen to specify the x-axis direction of the specimen,

standardizing coordinates of the exports and accounting for potential deviations in the camera angle with respect to the sample. Figure 3.8 shows the mask over the specimen and the three concentric circle pairs defining the coordinate system. Smoothing was applied, and several processing parameters, summarized in Table 3.2, were adjusted to the specific needs of the setup.

| Parameter | Value |
|--------------|---------------------|
| Facet size | 25 Pixels |
| Facet model | Bilinear |
| Grid spacing | 30 Pixels |
| Smoothing | 5x5 Gaussian filter |

Table 3.2: Relevant parameters used for the DIC.

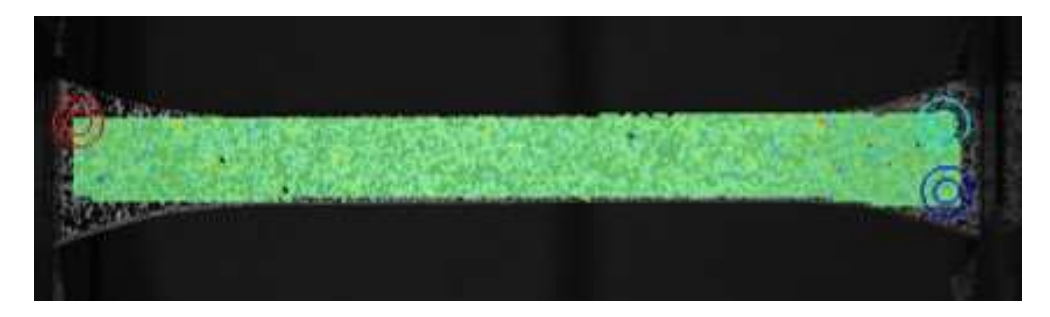


Figure 3.8: Image from Istra4D. The red dot marks the origin, the others define the direction of each axis.

3.3.2 Tensile Test

The test machine used is a Zwick Roell Retroline paired with a testControl II unit. Subsequent tests following ISO 527 with the three selected polymer materials were performed, using 5 samples per case for repeatability. A measurement of the cross-section of each specimen was taken prior to the test, and an identification number was given to each individual coupon for later reference. The naming convention used to designate specimen IDs begins with the name of the material, followed by information about the type of test (T for tension and C for compression), then the printing orientation of that sample (XY or Z) and finally the strain rate at which it should be tested, plus a number to distinguish repeated specimens. Figure 3.9 shows specimen PA12 T XY 2 SR 5 fixed to a dedicated tensile fixture with a maximum rated force of 10kN, which doubles that of the piezoelectric force sensor of the UTM, a value with a considerable safety margin.



Figure 3.9: A PA12 specimen on the fixture.

In this setup, the lower grip is fixed to the bottom of the machine, and the upper grip is connected to the 5kN sensor, which at the same time is attached to the moving platform carried by the leadscrews. Prior to the tests, safety limits were set to prevent damage by avoiding a crash between the fixtures or exceeding the rated force. Then, the gauge length, or the distance between grips at the start position, is given at 58mm. Every sample is taken to failure at a constant speed and the data is recorded via DIC and Zwicks' software in order to ensure a backup of the results.

All the recordings are postprocessed in Istra4D, where a polygon is drawn over the region of the specimen where failure initiates, so as to capture the complete local strain behaviour instead of the global displacement field. From this polygon, the mean strain over the surface in the x and y directions, as well as the analog inputs from the acquisition system (force [kN], time[s], displacement[mm]), are exported as an ASCII file. To interpret and process the test data and to calculate the desired material properties, a Python tool was developed that could read these files for evaluation.

This tool integrates a series of scientific libraries such as Pandas, NumPy, SciPy, scikit-learn, Matplotlib, or Plotly. It automatically scans for files tagged with the naming convention, filtering for the datasets corresponding to the correct test series. Files are parsed by detecting their header and converting the tab-separated values into a structured Pandas DataFrame. For each test, the specimen cross-sectional area is introduced to the DataFrame by referencing a CSV file containing width and thickness measurements for each ID. Then, an initial smoothing of the displacement and force signals is performed using a uniform moving average filter from the SciPy library, mitigating

high-frequency fluctuations coming from sensor noise and mechanical vibrations on the measurement equipment. The smoothing of the analog signals is critical for obtaining stable derivatives in the following calculations. All curves for the same series are then averaged before proceeding

Then, engineering stress and strain are derived from the force-displacement curves, followed by the calculation of true stress from the true strain [11] given by the DIC through the following equation:

$$\sigma_{true} = \sigma_{eng} \cdot e^{\varepsilon_{true}} \tag{3.1}$$

The assumption of a constant cross-sectional area implicit in engineering definitions does not hold, and thus true stress—strain curves represent a more physically meaningful description of the material response.

To extract the elastic modulus, the script isolates the quasi-linear region in the true stress–strain curve. A linear regression is performed, and the slope of the fitted function is saved as E, which is then stored in the DataFrame to be subsequently employed in the calculation of effective plastic strain ε_{eff}^{pl} , defined as:

$$\varepsilon_{eff}^{pl} = \varepsilon_{true} - \frac{\sigma_{true}}{E} \tag{3.2}$$

Where $\frac{\sigma_{true}}{E}$ is the recoverable strain [11].

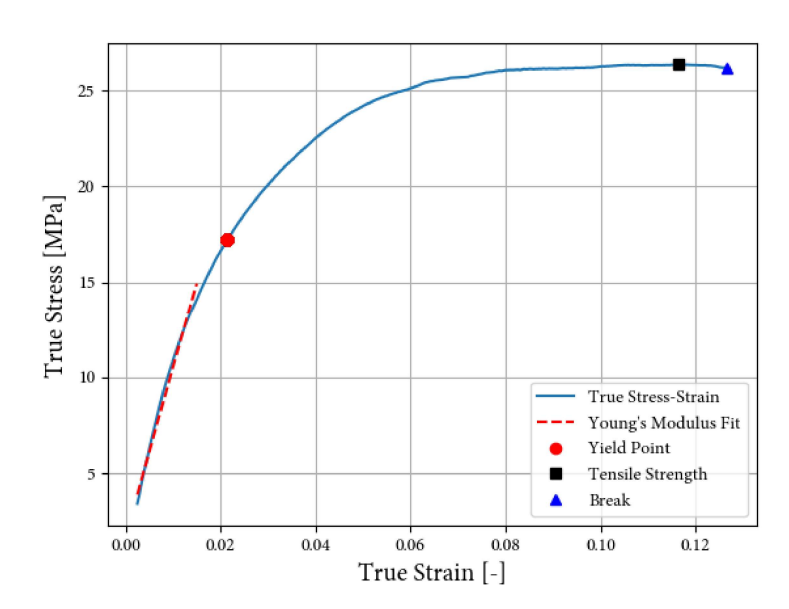


Figure 3.10: True Strain vs True Stress curve for PP.

The analysis of plasticity is followed by the determination of yield stress, for which the widely adopted 0.2% offset method is used. An offset line parallel to the elastic slope is constructed, and it identifies the intersection point with the true stress-strain curve. Since the experimental data is discretized, this can be achieved with the help of discrete sign-change detection together with linear interpolation. After the corresponding yield stress and yield strain are saved to the DataFrame, the tool identifies ultimate tensile strength (the maximum value of true stress) and the elongation at break (the last strain recorded

before failure). Figure 3.10 shows a visual overlay of the fitted Young's Modulus line on the experimental curve for PP material at 5mm/min under tension, as well as the yield point, the tensile strength, and the elongation at break. This is repeated for TPU and for PA12 following the same methodology.

3.3.3 Compression Test

For compression tests conducted according to ISO 604, the same UTM was used with a different setup. In order to keep a sufficient resolution with the reduced region of interest, up to four 4mm rings were added to the base of each lens providing enough optical zoom. The tensile grip was replaced for a flat base plate with a heavy duty ball joint with free rotation in all axis to avoid hyperstaticity, on the top platform, a punch cylinder of 40mm in diameter was attached, and the 5kN sensor was replaced for a 100kN sensor, given the expected higher loads of this test. The lighting was one of the main challenges due to the small size of the specimen. The blue LED lamps were arranged as shown in Figure 3.11, with two units on the base and two on the moving platform, as close together as the field of view of the cameras allowed. To improve stability in picture brightness, a small steel block was used to raise the specimen and allow its placement closer to the edge at a more appropiate angle.

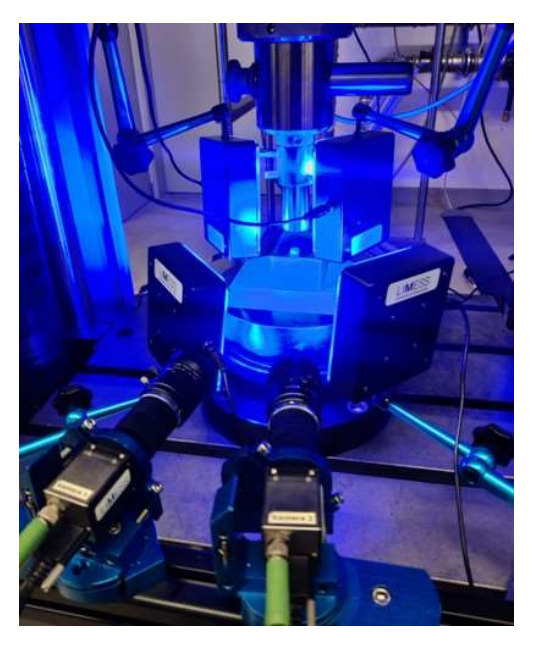


Figure 3.11: Enter Caption

Despite all efforts to obtain reliable DIC data, the large deformations of the specimen in depth led to a majority of facets that would become out of focus after the first few frames, thus losing all strain information. Fortunately, force and displacement data from the UTM were enough to derive the necessary properties through further processing using yet another Python script.

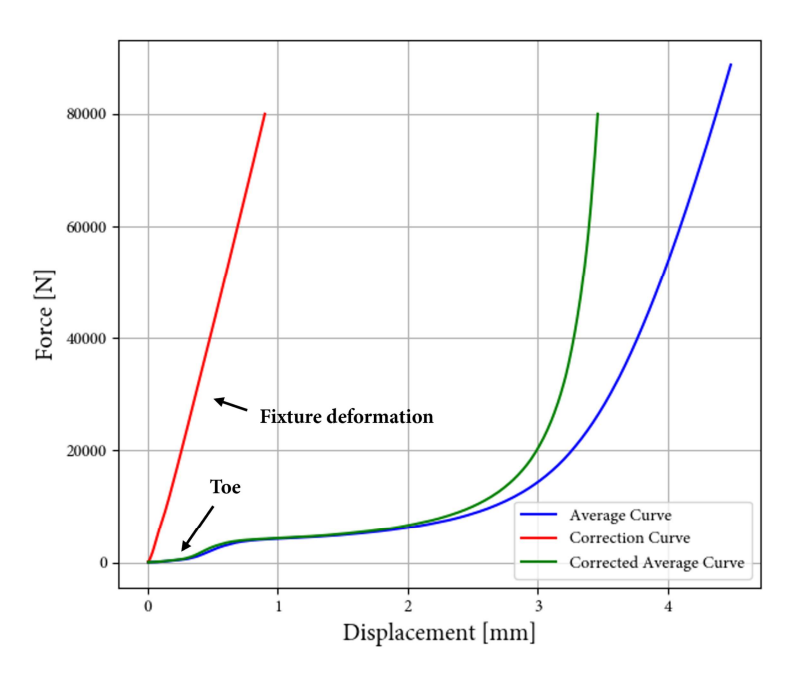


Figure 3.12: Original, correction, and corrected compression curves.

The code to extract the compressive properties follows a similar logic to the one depicted in the previous section. It also reads the ASCII files exported from the Zwick software, and sorts all the information within a Pandas dataframe, filtering the noise and averaging the curves of the same test series in the same way. A first dry test without any specimen was carried out to record the force-displacement curve inherent to the elasticity of the fixtures. In Figure 3.12, this effect is seen, leading to an overshoot of the height of 4mm of the specimen; the curve of the dry run is subtracted, and the corrected curve is considered for the rest of the calculations. A manual toe compensation is also performed,

to align the origin of the curve with the beginning of the elastic phase. The appearance of the toe is attributed to the irregularities on the top and bottom faces of the specimen, and the squeezing of the smear compound used on the fixtures to reduce friction and allow lateral displacement of the material under compression.

The solution to the lack of DIC footage for the calculation of true strain and true stress stems from the assumption that, on the three tested polymer materials, the deformation of the cylinder under compressive loads is radially symmetric and complies with the conservation of volume:

$$V = V_0 = A(h)h \tag{3.3}$$

Where h is the specimen height and A(h) is its cross-sectional area as a function of height.

This allows the calculation of the instantaneous cross-section of the specimen throughout the test:

$$A(h) = \frac{V_0}{h} = \frac{\pi r_0^2 h_0}{h} \tag{3.4}$$

Where r_0 is the original radius of the cylinder.

And so, the expected diameter at each height can also be obtained:

$$d(h) = \sqrt{\frac{4A(h)}{\pi}} = d_0 \sqrt{\frac{h_0}{h}}$$
 (3.5)

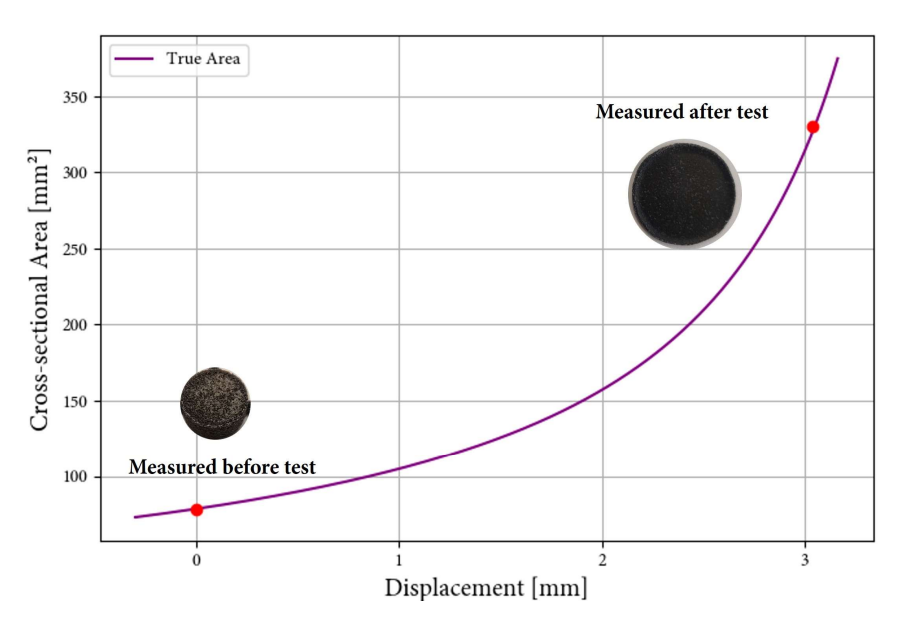


Figure 3.13: Plot of cross-sectional area as a function of vertical displacement with measurements for PP.

To validate this simplification, measurements before and after testing were taken to compare against the theoretical increase in diameter as a function of vertical displacement given by the volume conservation. The measurements match the derived expression for cross-sectional area with near-perfect accuracy, as Figure 3.13 reveals.

Continuing with the obtention of the compressive properties, the previous step allows to compute true stress directly:

$$\sigma_{\text{true}} = -\frac{F}{A(h)} = \frac{F(h_0 - \Delta h)}{A_0 h_0} \tag{3.6}$$

And for the strain, starting from the previous equation used for the tensile properties:

$$\sigma_{\rm true} = \sigma_{\rm eng} e^{\varepsilon_{\rm true}} \quad {\rm with} \quad \sigma_{\rm eng} = \frac{F}{A_0}$$
 (3.7)

Solving for true strain gives:

$$\varepsilon_{\text{true}} = \ln\left(\frac{\sigma_{\text{true}}}{\sigma_{\text{eng}}}\right) = \ln\left(\frac{\sigma_{\text{true}}A_0}{F}\right)$$
(3.8)

Substituting 3.8 into 3.6 eliminates A_0 and F, yielding:

$$\varepsilon_{\text{true}} = \ln\left(\frac{h}{h_0}\right) = \ln\left(1 - \frac{\Delta h}{h_0}\right)$$
 (3.9)

Having obtained σ_{true} and ε_{true} , the rest of the procedure for obtaining modulus and yield point is equivalent to the method used for the tensile specimens: modulus from the initial quasi-linear regime (ignoring the toe) and yield point by means of the 0.2% method. It is important to note that, contrary to the tensile counterparts, these specimens show no signs of apparent failure. In Figure 3.14, the stress curve begins a steep descent towards the end. Capturing this part of the compressive plastic deformation will play a key role in the determination of the densification phase in the simulation of structures.

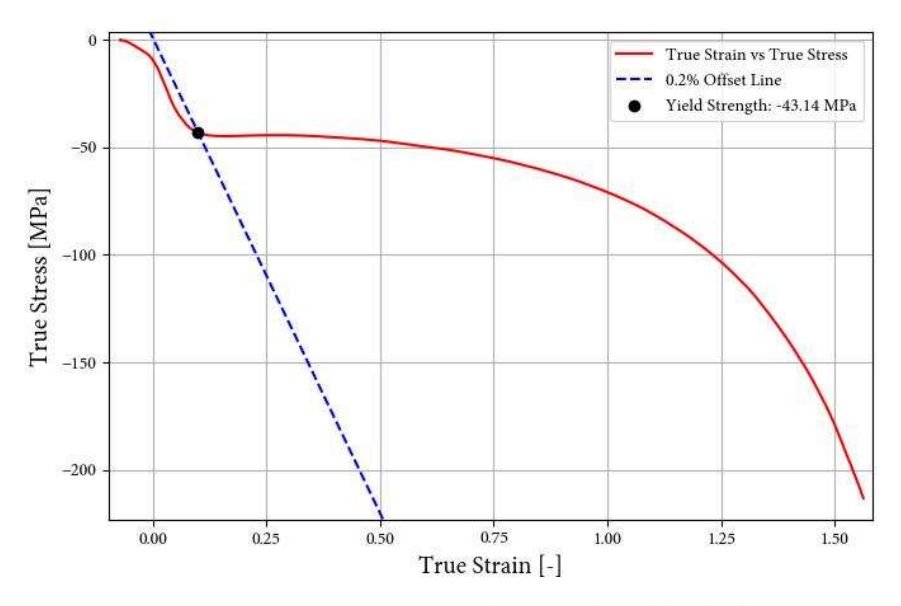


Figure 3.14: Compression curve for PP with yield calculation.

3.4 Manufacturing Anisotropy

A critical aspect of these parts is the presence of manufacturing anisotropy, which is inherent to the layered nature of the printing process. Unlike nearly isotropic materials produced by injection or extrusion, the mechanical properties of HSS prints depend on their build orientation. This anisotropy is primarily defined by the bonding between adjacent layers and the thermal history related to the deposition sequence.

When a load is applied parallel to the plane of the layers (X or Y direction), the mechanical response is determined by the strength of the continuous polymer strings, which allow the material to exhibit relatively high tensile strength and elongation at break. But when the load is applied perpendicularly to the layer interface, the strength is limited by the quality of interlayer adhesion. In AM, the bonding between layers is achieved through localized melting and cooling, rather than homogeneous consolidation, which leads to weaker interfaces that significantly reduce strength and ductility in directions normal to the build plane (Z).

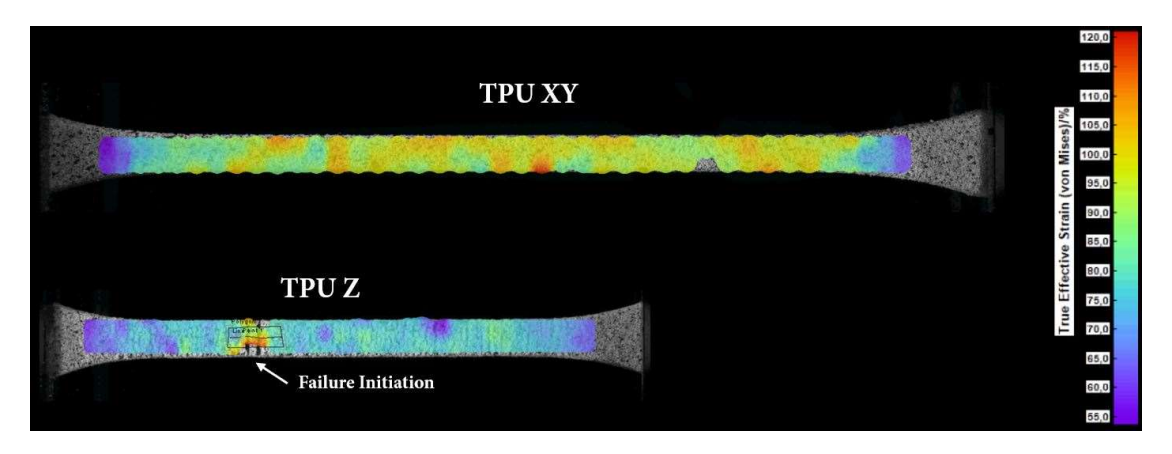


Figure 3.15: DIC comparison of the elongation at break for TPU with different printing orientation.

Figure 3.15 shows an example of this behaviour through DIC images of the elongation at break of TPU. The XY specimen is able to withstand significantly larger strains before failure than the Z specimen, in which localized failure of the layer interfaces, leading to rupture, can be observed in the center-left portion of the image.

In the context of this study, the mechanical characterization was carried out with particular emphasis on this (weakest) print direction. By adopting this conservative approach, the obtained material properties reflect the lowest structural performance that can be expected in service. Building the material model from properties measured along the strongest orientation would risk an overestimation of the SEA potential, and this optimistic bias could compromise the reliability of crashworthiness assessments, or even lead to unsafe design conclusions.

The decision on this conservative approach ultimately results in a safety margin, ensuring that the mechanical response observed in a real application will always be equivalent to or better than the simulated behavior.

3.5 Summary of Properties

The mechanical property summary presented in Table 3.3 results from the processed experimental data, and provides an overview of the three polymers. Several trends can be highlighted: TPU presents very low stiffness, with tensile modulus values on the order of 20 MPa. This is contrasted by PA12, where E_t exceeds 1.5 GPa and tensile strength reaches 40 MPa. PP sits between these two extremes with values in the hundreds of MPa range.

| Property | Symbol | TPU | PP | PA12 |
|-------------------------------|----------------|------------------------|------------------------|------------------------|
| Density | ρ | $1.12~\mathrm{g/cm^3}$ | 0.89 g/cm ³ | 1.01 g/cm ³ |
| Poisson ratio | u | 0.38 | 0.32 | 0.36 |
| Young's modulus (tension) | E_t | 21 MPa | 880 MPa | 1500 MPa |
| Young's modulus (compression) | E_c | 17 MPa | 440 MPa | 1080 MPa |
| Yield strength (tension) | $\sigma_{y,t}$ | 1.13 MPa | 17 MPa | 30 MPa |
| Yield strength (compression) | $\sigma_{y,c}$ | 3 MPa | 43 MPa | 48 MPa |
| Tensile strength | σ_{UTS} | 3 MPa | 26 MPa | 40 MPa |
| Elongation at break | $arepsilon_b$ | 33% | 13% | 6% |

Table 3.3: Mechanical properties of TPU, PP, and PA12s from experimental data.

The table successfully illustrates how a correct material selection allows for the adaptation of the mechanical response for different applications. The tensile stress-strain curve in Figure 3.16 also demonstrates the large deformability expected from an elastomer like TPU (33%), while PA12 fails at relatively low strains of around 6%.

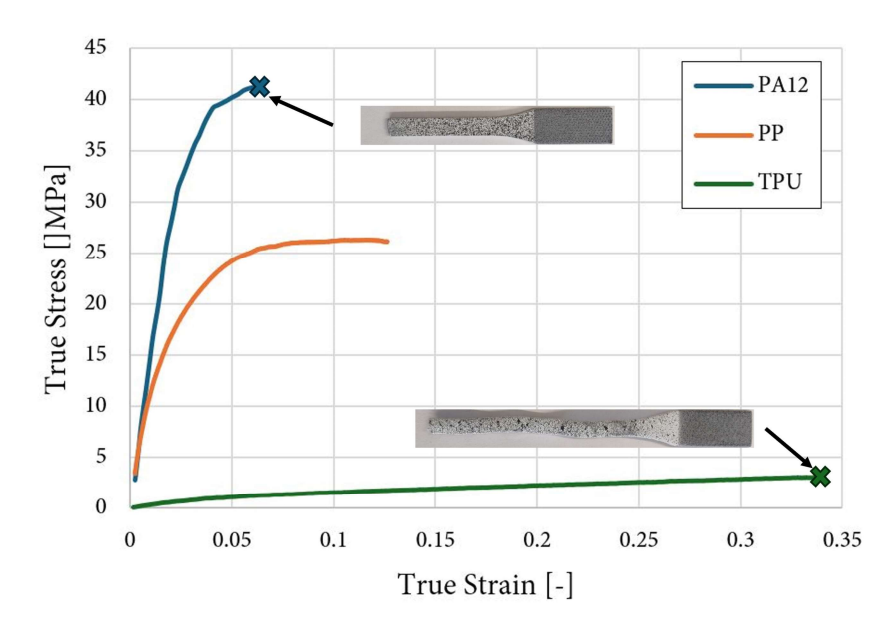


Figure 3.16: Tensile stress-strain curve for the materials of the study.

The performance of TPU, in particular, is significantly lower than what would be expected from conventionally processed material. Injection-molded TPU can achieve tensile strengths an order of

magnitude higher, but the samples tested here reveal values as low as 3 MPa. This is a relevant limitation of powder-bed AM for elastomers related to the previously described interlayer adhesion and porosity problems.

An interesting occurrence is the consistent difference between the elastic moduli measured in tension and compression. For all the tested polymers, E_c is lower than E_t . This is seemingly counterintuitive because compressive loading often results in additional constraints that could induce a stiffer response. However, the reduction in modulus under compression is linked to the microstructural reconfiguration of polymer chains. Under tension, chain segments align with the direction of the stress, which translates into a more efficient transfer of load. While under compression, chains are forced into configurations where buckling or local bending is more likely, which explains the reduced stiffness observed in compression. This already suggests the probable need for a material model that distinguishes between tensile and compressive properties like MAT124.

The same trend continues when evaluating the compression stress-strain curves in Figure 3.17, where the three materials show three different levels of performance, with the particularity of a crossover of the PA12 and the PP lines at around 115 MPa, indicating an overall better ductility of Nylon besides its initially higher stress in the plastic regime.

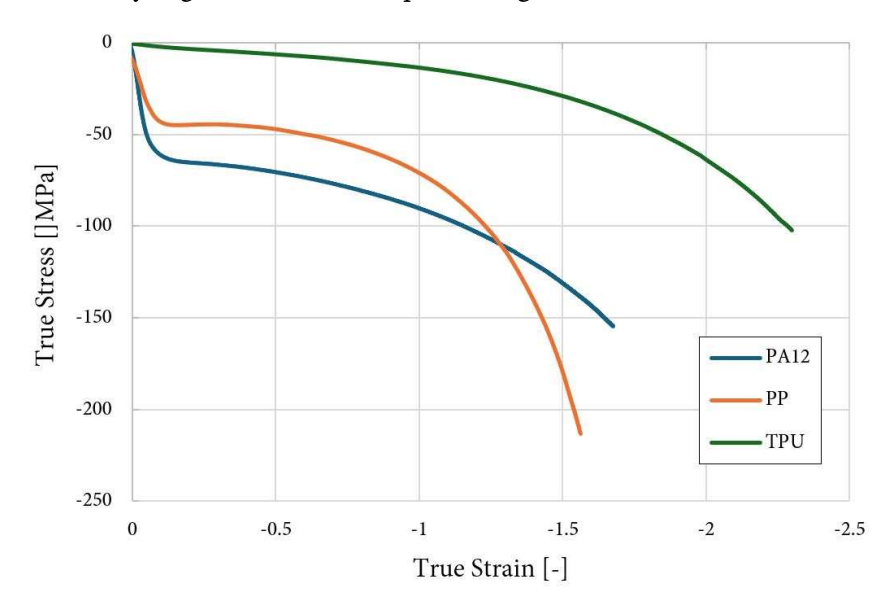


Figure 3.17: Compression stress-strain curve for the materials of the study.

3.6 Material Model Implementation

The transition from the measured material properties to the numerical implementation in LS-DYNA requires the implementation of a material model through a "keyword" card. Each keyword in LS-DYNA represents a constitutive model that translates physical behavior into a set of mathematical rules that the solver can apply to each element. The values discussed in the previous section are mapped into the standardized syntax.

| \$ | | | | | | | | | | | | |
|---------------------------------|---------|--------------|------------|-----------|------|------|----------|--|--|--|--|--|
| \$ Material card for PA12 - 024 | | | | | | | | | | | | |
| \$ | | | | | | | | | | | | |
| *MAT | _PIECEW | ISE_LINEAR_F | PLASTICITY | _2D_TITLE | | | | | | | | |
| Card | Templa | te | | | | | | | | | | |
| \$# | mid | ro | е | pr | sigy | etan | fail | | | | | |
| | 10 | 1.010e-6 | 1.495 | 0.3618 | | | 0.035687 | | | | | |
| \$# | С | р | lcss | lcsr | vp | | | | | | | |
| | | | 15 | 16 | | | | | | | | |
| \$# | eps1 | eps2 | eps3 | eps4 | eps5 | eps6 | eps7 | | | | | |
| \$# | es1 | es2 | es3 | es4 | es5 | es6 | es7 | | | | | |

In this example, MAT_PIECEWISE_LINEAR_PLASTICITY (MAT024) requires an initial yield stress and a tabulated plasticity curve defined through load curves. For this, the same Python tool automates the transformation of the effective plastic strain curve (LCSS) starting from the determined yield point into an ASCII export including 50 pairs of values describing the plastic behaviour. Failure strain (FAIL) corresponds to the maximum strain at break, and strain rate parameters (C, P) are left empty in this case since it is defined through a second load curve (LCSR).

For MAT124, a compressive modulus parameter (EC) is introduced, and a second effective plastic strain load curve(LCIDC) is added to model the compressive behaviour.

| \$ \$ \$ | Materia | l card for I | PA12 - 124 | | | | | |
|----------------|----------|--------------|------------|-----------|--------|--------|---------|--|
| 1 . | _PLASTI | CITY_COMPRES | SSION_TENS | ION_TITLE | | | | |
| Card | d Templa | te | | | | | | |
| \$# | mid | ro | е | pr | С | р | fail | |
| | 10 | 1.010e-6 | 1.495 | 0.3618 | | | | |
| \$# | lcidc | lcidt | lcsrc | lcsrt | srflag | lcfail | ec | |
| | 14 | 15 | | 16 | 0.0 | | 1.07705 | |
| \$# | рс | pt | pcutc | pcutt | pcutf | _ | _ | |
| \$# | k | | | | | | | |

Material ID (MID) is set at 10 for consistency across simulations and to facilitate the automation of the Finite Element Method (FEM) cases with minimal changes between studies. The complete material cards for the three polymers, including all load curves, can be found in Annex B.

3.6.1 Triaxiality Dependent Failure

One of the critical limitations of plastic material models in LS-DYNA is their inability to simulate failure in a physically realistic way. To improve the accuracy of the material cards, *MAT_ADD_ERO-SION was added, a tool that offers a broad set of parameters to incorporate element deletion through different strain, stress, or damage criteria.

| * | MAT_ADD_ER | OSION | | | | | |
|----|------------|----------|-------------|--------|---------|--------------|--|
| \$ | mid 10 | exc | effeps | voleps | numfip | ncs 1e-08 | |
| \$ | mnpres | sigp1 | epssh | sigth | impulse | failtm | |
| \$ | idam -1 | dmgtyp | dmgexp | dcrit | fadexp | lcregd | |
| \$ | dityp 0 | p1 99 | p2 | рЗ | | | |
| \$ | detyp 1 | dctyp | q1 5e-05 | q2 | | | |

A very small cutoff parameter ncs = 1e - 08 was introduced to prevent singularities that could appear when the model attempts to evaluate unstable conditions near fracture. In this model, using (idam = -1), the response remains fully elastic-plastic up to the defined failure point, when the element becomes instantly eroded, a simplification that is consistent with the experimental results, where a relatively abrupt fracture after necking takes place, and there is no apparent extended softening that could justify a gradual damage law.

The *MAT_ADD_EROSION keyword is coupled with a triaxiality-dependent failure criterion defined through a load curve, meaning the critical strain at which fracture occurs is no longer assumed to be constant. Instead, it is modeled as a function of the stress state defined by Equation 2.12 within the material. This is again motivated by the experimental evidence of failure at different plastic strains depending on the loading direction, and especially by the strong influence of the absence of failure in the compression specimens. In the case of PP, this curve is discretized assuming a high failure strain for uniaxial and multiaxial compression:

| *DEFINE_CURVE_TITLE | | |
|----------------------|--------------------|--|
| Triaxiality curve of | undamaged material | |
| 99 | | |
| -1 | 10.000 | |
| -0.33 | 5.000 | |
| 0 | 0.19120901 | |
| 0.33 | 0.19120901 | |
| 1 | 0.19120901 | |
| | | |

Despite the ability of the material card to capture this effect through the FAIL input, the use of a triaxiality curve allows the solver to interpolate for stress states that are not purely tensile or compressive, and hence the utility of this additional feature.

4 Numerical Investigation

This chapter presents the numerical investigation of additively manufactured auxetic lattice structures. It describes the complete methodology used for simulation, from material model validation to 3D modeling, meshing, and simulation setup, as well as the postprocessing methods employed to extract performance metrics. This provides a comprehensive framework for evaluating different auxetic designs with regard to crash applications and potential for energy absorption.

4.1 Validation of the Material Cards

The fidelity of the previously defined material cards cannot be assumed directly. The translation from experimental data to constitutive parameters involves several approximations, and numerical artifacts such as mesh size can further affect accuracy. For these reasons, it is crucial to validate the developed material models against the baseline tests that were used for their calibration. This ensures that the material models reproduce not only the stress–strain behavior at an element level, but also the global response of the tested specimens under tension and compression.

The validation procedure consists on the simulation of tensile and compression tests of the three base materials using finite element models of the coupon specimens. By directly mimicking the testing procedure in LS-DYNA, the comparison between measured and simulated force—displacement curves provides a quantitative measure of model accuracy. These simulations also serve as a familiarization step for the use of LS-DYNA since they do not require high computational power and can be run in a few minutes.

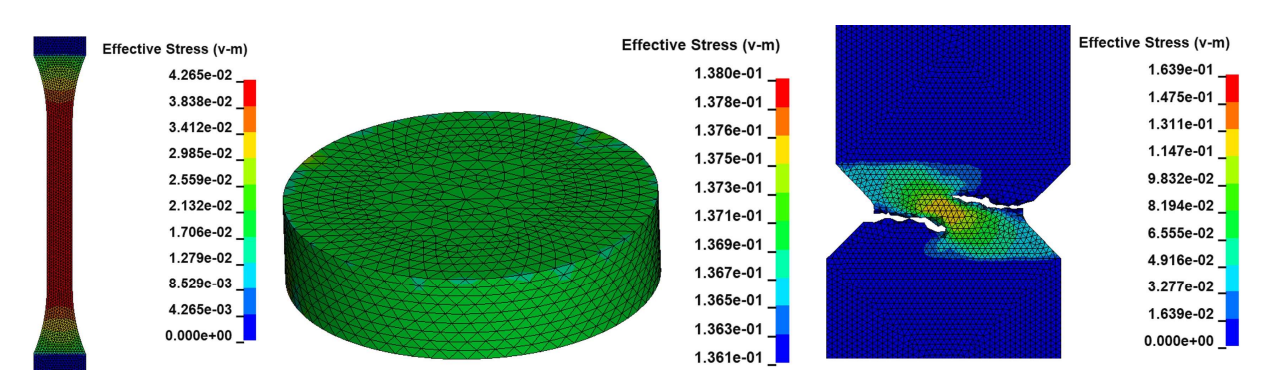


Figure 4.1: Stress contours for simulated specimen geometries in PA12.

Figure 4.1 illustrates representative finite element meshes of the tensile, compression, and shear coupons with contours of effective stress (GPa) at different points of the simulation sequence. The tensile specimen shows a homogeneous distribution of stresses in the center part of the coupon, while the compression cylinder spreads all loads equally throughout the entire test piece. In the

35

case of the shear specimen, the two fractures initiating from the narrowest section indicate an appropriate behaviour, and the stress is concentrated on the remaining connecting material. These figures establish the link between the physical experiments and the numerical counterparts used for validation, and visually display an equivalent response to the experiments.

The next step to evaluate the numerical accuracy is the control of non-physical energy modes in the simulation. Figure 4.2 shows the evolution of external work, internal energy, and hourglass energy in the tensile simulation of PA12. External work is the total energy input by the UTM, internal energy corresponds to the energy stored and dissipated in the material, and Hourglass energy is a purely numerical artifact resulting from the use of finite elements. An accurate simulation exhibits hourglass energy at negligible levels. In this case, the hourglass energy remained

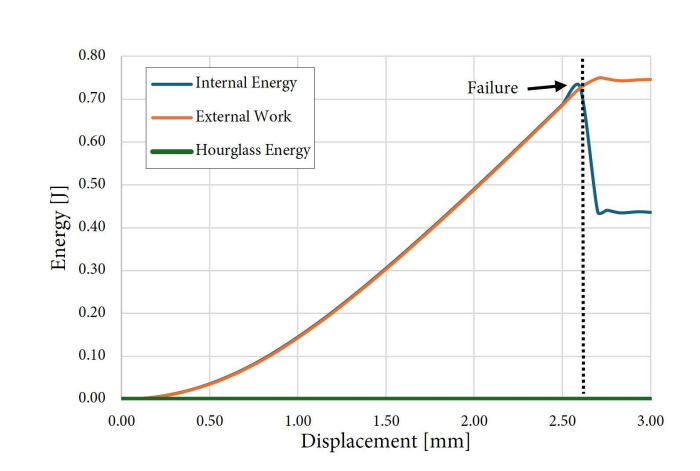


Figure 4.2: Energy plot for the tensile simulation of PA12.

at zero throughout the whole sequence, confirming that no spurious energy modes were involved and providing confidence that the results are governed only by the material model.

The central results of the validation are the force–displacement plots for each of the three investigated polymers. For tension and compression, the experimental response is compared against simulations of the same specimen under the specified loading conditions. To evaluate the robustness against mesh dependence, three different element sizes were tested for each configuration: 1mm, 0.5mm and 0.25mm. For TPU, the simulation curves (Figure 4.3) reproduced the character-

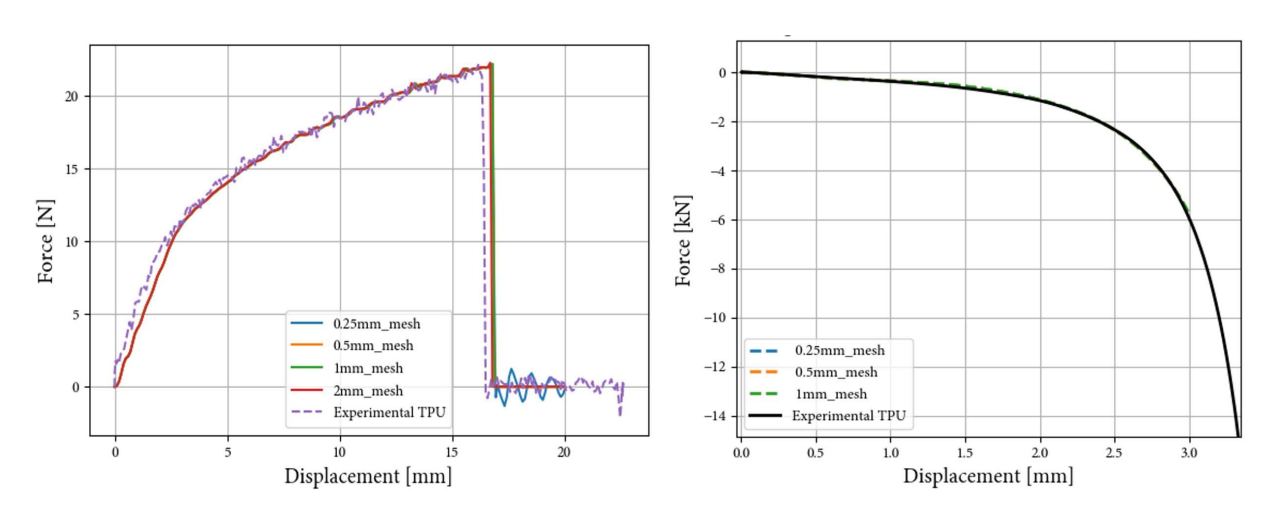


Figure 4.3: Tension (left) and compression (right) validation for TPU.

istic large-strain ductility observed in the experiments. A minor deviation in the elastic regime can be noticed, but the yield transition and the plasticity region are remarkably accurate. Elongation at break is not predicted with perfect accuracy, but within a reasonable margin. The accuracy in the

compression simulation is near perfect, and the variation between different mesh element sizes is negligible.

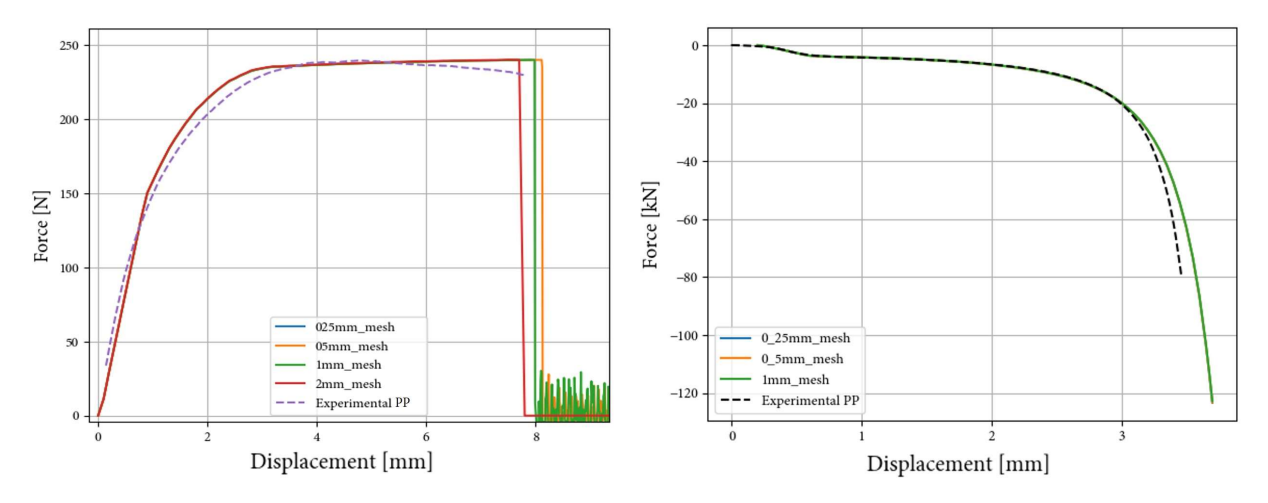


Figure 4.4: Tension (left) and compression (right) validation for PP.

The validation of PP involved some fine-tuning in the definition of the effective plastic strain (LCIDT) curve, due to the fact that the maximum tensile strength of this material is not located at the failure strain, which is an exception in this study. Multiple errors from LS-DYNA are derived from the change in this load curve from an increase to a decrease of the true stress once past σ_{UTS} .

To eliminate this issue, an artificial slope was imposed, and hence the discrepancy that can be observed in the tensile plot in Figure 4.4, where the experimental curve has a noticeable decay near the elongation at break that is not present in the simulation data. There is also a slight deviation towards the end of the plastic regime in the compression curve, but the model works with acceptable accuracy, and the global response is adequate for the purpose of this study. The models with 0.5mm elements appear to be the lowest resolution providing mesh independence.

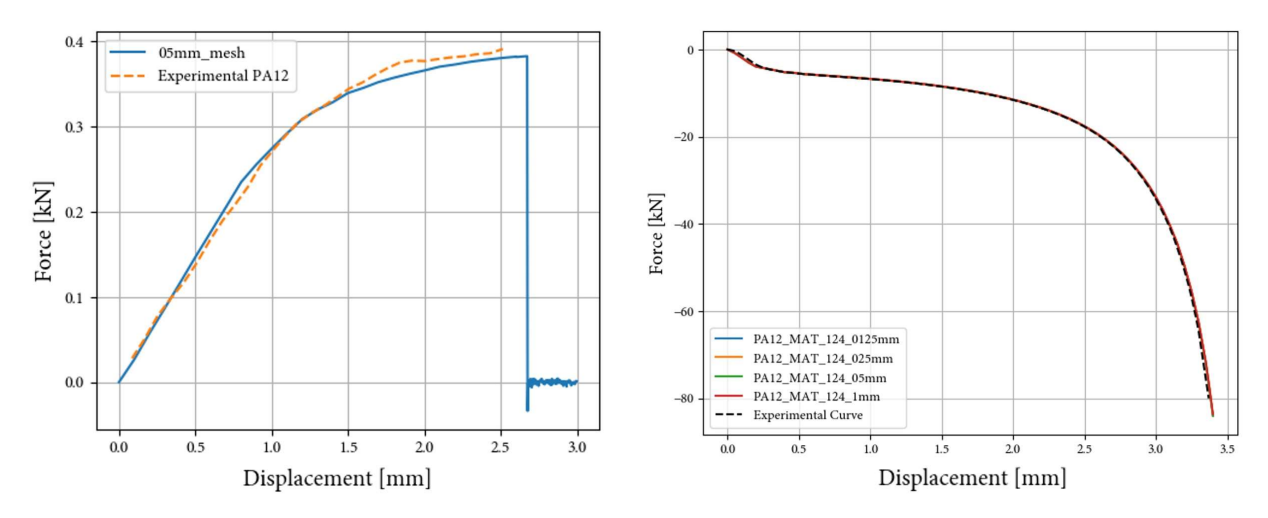


Figure 4.5: Tension (left) and compression (right) validation for PA12.

For PA12, the stiffer and more brittle characteristics were also correctly reproduced. The sharp failure near the experimentally observed elongation was captured by the erosion criterion, and the compression validation is the best match yet.

To assess the accuracy of the material models in a quantitative way, the Root Mean Square Error (RMSE) was calculated between the experimental curves and the numerical predictions in tension and compression. For each case, the RMSE is defined as:

$$RMSE = \sqrt{\frac{1}{N} \sum_{i=1}^{N} \left(F_i^{\text{exp}} - F_i^{\text{sim}}\right)^2}$$
 (4.1)

where

- $F_i^{\text{exp}} = \text{experimental force at displacement step } i$,
- $F_i^{\text{sim}} = \text{simulated force at the same displacement step } i$,
- N = total number of data points considered in the comparison.

To normalize this comparison across different materials and load cases, the error was also expressed as a percentage RMSE relative to the maximum experimental force:

$$RMSE[\%] = \frac{RMSE}{F_{max}^{exp}} \times 100 \tag{4.2}$$

where $F_{\rm max}^{\rm exp}$ is the maximum experimental force recorded during each test.

The calculated RMSE values are summarized in Table 4.1.

| | | TPU | PP | PA12 |
|-------------|---------------|--------|-------|-------|
| Compression | RMSE[kN] | 0.891 | 7.540 | 0.563 |
| Compression | Relative RMSE | 1.11% | 9.43% | 0.70% |
| Tension | RMSE[kN] | 0.0011 | 0.010 | 0.009 |
| rension | Relative RMSE | 4.78% | 4.17% | 2.31% |

Table 4.1: RMSE values for compression and tension validation of TPU, PP, and PA12.

Overall, the results confirm a satisfactory agreement between experiments and numerical models. In tension, the errors remain below 5% for all materials, although in compression, there is a larger discrepancy for polypropylene (PP), which shows an RMSE of 9.43%. A deviation that can be attributed to a more complex nonlinear behavior of PP that is challenging to capture with the employed constitutive models. In comparison, TPU and PA12 show excellent agreement in compression, with errors below 1.2%. The consistently low errors across the table validate the accuracy of the developed material cards and the reliability of the simulation approach, providing confidence in its capability for prediction in the subsequent structural simulations.

4.2 Structure Parametrization and 3D Modelling

In this study, a 3D reentrant auxetic geometry was selected over other available alternatives, such as chiral or rotating unit cells, a decision that was mainly motivated by the different deformation mechanisms that dominate in each topology. Chiral lattices exhibit bending-dominated behavior, where energy absorption is driven by localized rotations and flexural modes of the struts [13].

This generally results in a reduced SEA compared to stretch-dominated systems. Reentrant lattices present a configuration that exploits axial stretching of a portion of the struts during compression, a response that could enable a more efficient load transfer and has the potential to improve the energy dissipation capacity per unit mass of material, as stated in the hypothesis. In addition, chiral lattices are well documented in the literature, with consistent results on the optimization of their radius, strut thickness, and global configuration. For reentrant types on the other hand, the analysis of optimal parameter combinations remains less explored, opening the possibility for further contributions.

The geometry of the 3D reentrant unit cell can be simply defined by a relatively small set of parameters: the base size $b_{\rm size}$, the height H, the length L, the strut thickness t, and the reentrant angle θ . These variables are illustrated in Figure 4.6, which includes a two-dimensional representation of the unit cell. L and H are dependent on the base size of the UC, but more critical is the reentrant angle θ , which defines the auxetic effect.

In this study, θ was fixed at 70° based on previous results from the literature, where it represents a good balance between negative Poisson's ratio and stability under compressive loading [19]. By fixing this angle, the analysis can then focus on the influence of two other key parameters: the base size and the relative thickness of the struts, which control the structural density, stiffness, and the resulting SEA, and whose combined effect has not been quantified in a systematic manner to this date.

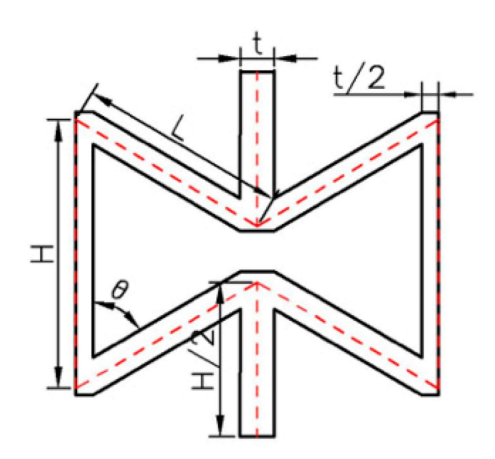


Figure 4.6: Reentrant cell parameters [29].

The parametrization scheme developed in this study is summarized in Table 4.2. Parting from the decision to make all specimens take the shape of cubes with 50mm sides due to limited manufacturing resources, the number of cells per side of the cube, $c_{\rm count}$, is a user-defined input that determines the resolution of the lattice tessellation.

| Parameter | Units | Value | Description |
|----------------------|--------------------------------|-------------------------------|--|
| c_{count} | User defined | | Number of cells per side of the cube |
| $t_{ m bs}$ | _ | User defined | Thickness as a percentage of base size |
| $b_{ m size}$ | mm | $50/c_{ m count}$ | Base size of the unit cell |
| t | mm | $b_{ m size} \cdot t_{ m bs}$ | Strut absolute thickness |

Table 4.2: Definition of lattice design parameters with corresponding symbols, units, and values.

As a consequence, the base size $b_{\rm size}$ is calculated as the overall specimen size divided by $c_{\rm count}$. The thickness of the struts t is computed as a percentage of $b_{\rm size}$ through the parameter $t_{\rm bs}$, allowing it to be expressed in a dimensionless way that can be easily compared across specimens. This approach aims to ensure consistency between different lattice configurations and provide the ability to vary the structural parameters.

Base Size 8.33mm 7.14mm 6.25mm 8.37 8

Figure 4.7: Grid of permutations in size and thickness for the reentrant unit cell.

Two geometric parameters were selected for a more detailed study: the base size $b_{\rm size}$ and the relative strut thickness $t_{\rm bs}$, which were varied in nine different permutations with the goal of quantifying their influence on the specific energy absorption. By sweeping these values, it is possible to generate a dataset of lattice designs with the capability to reveal performance trends.



Figure 4.8: Kelvin Cell CAD.

This parametrization was implemented in Fusion 360, the tool used as default CAD environment throughout the study. A fully parametric model of a single three-dimensional reentrant cell was constructed. This allowed for an automated generation of every different 3D model as soon as one of the parameters is modified, eliminating the need for a manual redrawing of the entire lattice geometry. Figure 4.7 compiles the nine permutations in a visual grid to gain a perspective of size and thickness.

The use of parametric modelling also ensures that the dependent dimensions t, H, and L preserve the geometric relationship when updated. Since one of the objectives is to compare the performance of auxetics against other regular lattices with a critical perspective, a well-studied structure like the Kelvin Cell also needs to be modeled.

Following the same design methodology, a UC like the one in Figure 4.8 was created with the baseline parameters of $b_{\rm size}=8.33{\rm mm}$ and $t_{\rm bs}=0.08$.

4.3 Automated Meshing

In order to perform numerical simulations, the continuous geometry of the CAD models must be discretized into a finite set of elements. This is the goal of meshing, a process that enables the equations of motion to be solved through the FEM.

For the present study, tetrahedral elements are chosen because they offer a practical solution for meshing complex geometries. Unlike other element types requiring structured meshes and hard to implement in thin features, tetrahedral elements can adapt to intricate shapes. This versatility makes them a suitable candidate for auxetic structures, with sharp angles and intersecting struts.

The formulation employed is the four-node tetrahedron element (Figure 4.9) with one-point integration, characterized by its simplicity and robustness. Its shape functions are linear, defined over the coordinate system (r, s, t) as:

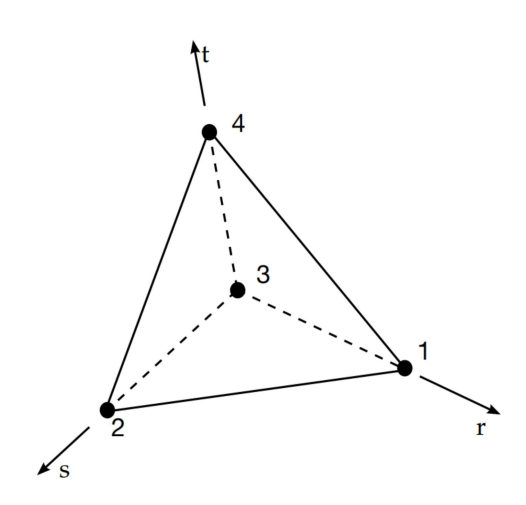


Figure 4.9: Four-node tetrahedron element [24].

$$N_1(r, s, t) = r,$$
 (4.3)

$$N_2(r, s, t) = s,$$
 (4.4)

$$N_3(r, s, t) = 1 - r - s - t, (4.5)$$

$$N_4(r, s, t) = t.$$
 (4.6)

This eliminates potential spurious kinematic modes and the need for hourglass control, as opposed to hexahedral elements. In the context of auxetic lattice simulations, the advantages of a tetrahedral mesh outweigh any possible drawbacks. For lattice structures in particular, meshing plays an important role in terms of accuracy and computational efficiency. A coarse mesh will fail to capture the complex stress and strain distributions at the struts and nodes, while an excessively refined mesh can result in an infeasibly large computational cost. This is especially concerning in the case of three-dimensional lattices with thousands of unit cells. A maximum element size of t/2 was chosen for the meshing, as shown in Figure 4.10, which represents a balance between an acceptable resolution and a run time that can be handled with the available hardware.

Difficulties were found when attempting to generate a mesh in PrePost directly by importing the CAD file (.step format was generally used) due to the capabilities of the software to read and processs all the facets of the geometry, which would require up to 100Mb of storage space. Other alternatives, such as the implicit geometry generator NTop software, were explored. This tool is able to generate complicated lattice objects while still allowing a very light fast manipulation, but the conversion of the structure to a compatible format for PrePost turned out to be yet another barrier.

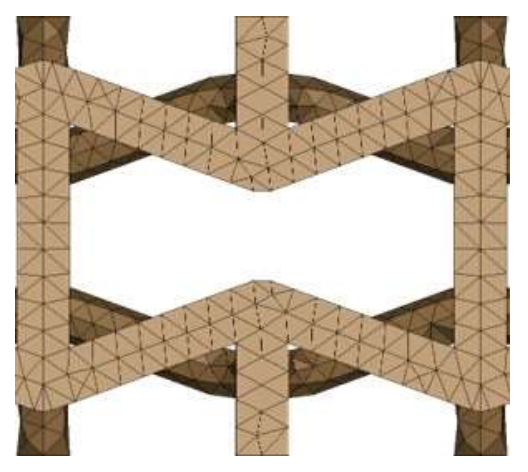


Figure 4.10: Detail of the meshing of a reentrant cell.

In the end, the meshing approach relied on a two-phase process. As a first step, a unit cell was imported to Prepost, and a tetrahedral mesh was generated from its geometry. The UC received special treatment of the lateral faces to ensure node symmetry in all directions, in preparation for a posterior merging operation with the contiguous cell. This mesh was saved with a traceable name indicating the type of lattice (RE= reentrant, KC= Kelvin Cell...) and the particular version of base size (BS8.33, BS7.143...) and thickness ratio (T0.08, T0.10...).

In a second phase, a Python code was used to generate the full setup mesh from the individual unit cells. The script reads the keyword file of a meshed unit cell, replicates it

in the three axis, attaches compression plates, and outputs a mesh that is ready for simulation. The process begins by parsing the keyword file to extract node coordinates and element data, which are then stored in dictionaries. The unit cell is positioned, rotated (if indicated), and duplicated in the x, y, and z axes through the base size indicated in the name of the file. During this replication, the nodes located at the same coordinates (the boundaries of the cells) are searched using a nearest-neighbor method and merged to join the cells.

```
# === AUTOMATIC BATCH PROCESSING ===
target_cube_mm = 50.0
plate_size = (100.0, 100.0, 5.0)
plate_spacing_above = 0
plate_spacing_below = 0
plate_divs = (50, 50, 2)
```

Once the lattice is generated, two meshed plates with customizable size and mesh fineness are created and positioned above and below the structure, acting as the loading and support elements. The plates are also discretized with tetrahedral elements in a structured grid, and positioned relative to the lattice bounding box to ensure the correct distance to the test object. Finally, they are assigned different part IDs for the definition of boundary conditions. After merging all the duplicate nodes, the complete system is written into LS-DYNA keyword format.

The process is run in batch mode, which means that the script scans the working directory for all the unit cell meshes of different base sizes. For every individual case, the cell count per side is automatically adjusted so that a 50 mm cube is generated. With this tool, dozens of lattice configurations can be generated in seconds, facilitating the parametric studies of this work.

4.4 Simulation Setup

The computational work for this study was divided between two platforms according to the scale of the simulation. The validations of single specimens under tension or compression were run on a local computer. With a relatively small number of elements, they could be executed within a reasonable time of under an hour on limited resources, making it adequate for the validation of the material cards.

The full-scale lattice structures required a significantly larger mesh, especially when exploring different base sizes and relative thicknesses. These models contained around 600.000 elements on average and demanded several days of runtime to complete. To handle this, a dedicated workstation with higher processing power and memory was used, allowing the simulations to run stably and avoiding excessive computation times that would make the parametric study impossible. The specifications of both systems are summarized in Table 4.3.

| System | Component | Value |
|----------------|------------------|--|
| | CPU | Intel Xeon w3-2435, 8 Cores / 16 Threads, 3.10 GHz |
| Local Computer | RAM | 32 GB, 3200 MHz |
| | Data storage | 1 TB |
| | CPU | 2 × 16-Core AMD EPYC 7313 |
| Workstation | RAM | 16×64 GB DDR4, 3200 MHz |
| Workstation | Number of nodes | 20 |
| | Cores (per node) | 32 |

Table 4.3: Hardware specifications for the local computer and the workstation.

4.4.1 Control

To ensure numerical stability and efficiency in the simulations, an automatic implicit-to-explicit switch was adopted, following the methodology developed by Lupprian [18]. Her approach makes use of the advantages of implicit integration for the initial part of the simulation and automatically transitions to explicit time integration once failure occurs, or if convergence difficulties are found.

Implicit methods are computationally more efficient for problems dominated by quasi-static behaviour, which makes them ideal for the early stages of the simulations, where the response is predominantly elastic. Once damage and failure mechanisms make an appearance, the iterative solution process required by implicit solvers will fail to reach equilibrium, and a premature termination of the simulation will occur. The keyword *CONTROL_IMPLICIT_AUTO was employed to monitor convergence and trigger a switch to explicit time integration.

The specific control parameters set the maximum implicit time step to $\Delta t_{\rm max} = 0.005\,{\rm ms}$. Once the explicit phase begins, the solver continues with a smaller time step to ensure stability in the highly nonlinear regime. Despite being more computationally demanding, it is robust against divergence and able to handle fracture and behaviour after failure.

4.4.2 Boundary Conditions

The boundary conditions were defined to reproduce the experimental setup: the lattice was kept completely free without constraints, to allow its deformation and transfer off loads to develop naturally under the rigid plates and avoiding an artificial stiffening of the structure.

The upper rigid plate was imposed a prescribed displacement in the negative y direction through the *BOUNDARY_PRESCRIBED_MOTION_RIGID_ID keyword. This motion used a sinusoidal loading curve (Listing 4.1) to provide a smooth force increase during the initial stage. This is done to prevent a sudden dynamic shock.

Listing 4.1: Boundary condition for the top plate using a prescribed sinusoidal motion.

| *B0l | JNDARY_PRES | SCRIBED_MOT | ION_RIGID | _ID | | |
|------|-------------|-------------|-----------|------|----|--|
| \$ | nsid | dof | vad | lcid | sf | |
| | 1 | | | | | |
| | 11 | 2 | 0 | 1000 | -1 | |

For energy dissipation studies, where a phase in which the load is released from the specimen, a second motion curve was defined (Listing 4.2), reversing the direction of the displacement, which was defined before the densification phase for each material after a first evaluation.

Listing 4.2: Boundary condition for the top plate in energy dissipation case studies.

| *DEFINE_CURVE_TITLE | | | | | | | | | | | |
|---------------------|------|------|---------|--------|------|------|--------|--|--|--|--|
| \$ | LCID | SIDR | SCALEX | SCALEY | OFFA | 0FF0 | DATTYP | | | | |
| | 1000 | 0 | &et/100 | &v | 0.0 | 0.0 | 0 | | | | |
| | | 0.0 | | 0.000 | | | | | | | |
| | | 0.5 | | 1.000 | | | | | | | |
| | | 1.0 | | 0.000 | | | | | | | |

The lower rigid plate was not assigned any boundary condition. Instead, it was fixed in position through its material card. Assigning it a *MAT_RIGID model with all translation and rotation Degree of Freedoms (DoFs) constrained as shown in Listing 4.3, the plate remained stationary during the simulation.

Listing 4.3: Bottom plate fixed using a rigid material model.

| *MAT_RIGID_TITLE | | | | | | | | | | | |
|------------------|---------|----------|-------|--------|------|--------|------|--|--|--|--|
| Botto | m Plate | Material | | | | | | | | | |
| \$# | mid | ro | е | pr | n | couple | m | | | | |
| | 12 | 7.5E-6 | 210.0 | 0.3 | 0.0 | 0.0 | 0.0 | | | | |
| \$# | cmo | con1 | con2 | spcnid | xspc | yspc | zspc | | | | |
| | 1.0 | 7 | 7 | 0 | 0.0 | 0.0 | 0.0 | | | | |

Together, these boundary conditions replicate the experimental compression and tension setups: the lattice deforms freely between two rigid plates, one fixed and one prescribed with a smooth vertical motion. This configuration ensures that the numerical model captures the intrinsic response of the auxetic structures under load without introducing boundary artifacts.

4.4.3 Contact Definition

An accurate contact modeling is essential to achieve a realistic interaction between the rigid plates and the lattice structure, but also within the lattice itself. LS-DYNA's automatic contact options are used because they adapt efficiently to contact surfaces that evolve through the simulation in a convenient manner

Two *CONTACT_AUTOMATIC_NODES_TO_SURFACE definitions are applied to model the interaction between the nodes belonging to the lattice and each plate respectively. Frictional effects are also included with a static coefficient of $f_s = 0.4$ and a dynamic coefficient of $f_d = 0.2$, chosen from the literature, to prevent excessive sliding.

Finally, a *CONTACT_AUTOMATIC_SINGLE_SURFACE was added to capture self-contact within the lattice, which was necessary due to the large deformations that caused local collisions between struts. Without this definition, an interpenetration with increasing unrealism as the structure progressively fails would take place, compromising the validity of the results.

4.5 Postprocess Methodology

The postprocessing of the simulations is prepared with the goal of extracting meaningful data that can allow the validation against experimental results and, more importantly, a deeper understanding of the mechanical behavior of the structures. From each simulation, different types of information were systematically collected. First, the internal energy was monitored throughout the compression; to evaluate it, the eroded internal energy belonging to the deleted (failed) elements must also be considered. Both are taken from the *matsum* section of the .binout files generated by LS-DYNA. It provides valuable insights into the progression of damage and energy absorption capacity of the structure, which is key to assess crashworthiness. Then, the force—displacement curves are obtained from the reaction forces at the rigid plates (master - reforce in the .binout file). From them, values such as PCF or MCF can be calculated, and serve as the primary validation metric

In addition to global measures, local field data were also analyzed through fringe plots. These included distributions of *triaxiality*, *stress*, and *strain* within the lattice members. The triaxiality parameter was particularly useful to identify failure modes by indicating whether the local stress state is dominated by tension, compression, or shear. Stress and strain contours, on the other hand, provide a detailed view of load distribution across the unit cells and allow the identification of failure initiation zones and progressive collapse mechanisms.

The numerical approach offers several advantages over experimental testing. Experiments provide direct physical validation, but they are limited by their high cost and the difficulty of measuring internal variables such as triaxiality or localized stress. Numerical simulations, on the other hand, allow for practically unlimited exploration with reduced resources, opening the possibility to study multiple geometry variants without having to manufacture them. Simulations offer additional access to internal mechanical parameters that can not be captured experimentally, providing a more complete dataset. This makes the numerical study a powerful tool for investigations.

5 Discussion

This chapter includes a comprehensive analysis and interpretation of the results obtained from the numerical simulation of the auxetic lattice structures. The discussion examines the behavior of 3D reentrant structures under compressive loading, evaluating their energy absorption and dissipation characteristics. The influence of design parameters, material model selection, loading orientation, unit cell dimensions, and strut thickness on crashworthiness performance is evaluated with the aim of providing insights into their potential, but also their limitations.

5.1 General Behavior

The discussion on the results of the numerical simulations starts with an overview of the general behaviour of the auxetic structures under crash loading. A first remark that can be pointed out is that the deformation across the geometry is uniform until the failure begins to develop close to the nodes. This indicates that stress concentrators were not artificially introduced to the lattice through the mesh resolution. Figure 5.1 presents the strain field on the loaded cube and a detail of the unit cell behaviour before and after failure.

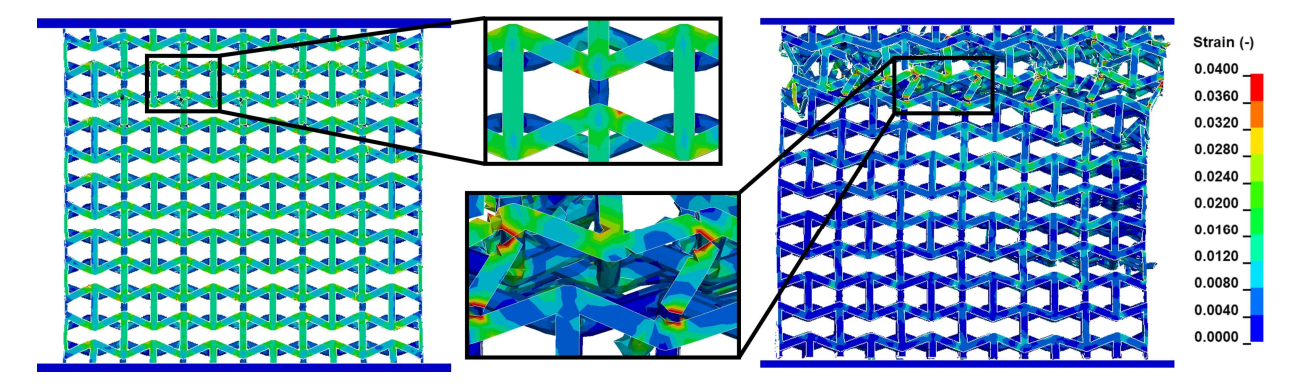


Figure 5.1: Strain field and UC detail before and after failure for the baseline 3D Reentrant cube in PA12 material.

When failure initiates, it does so at the base and top of the vertical pillars, through the shallow corner described by the strut angle θ . Subsequently, the pillars in the same row bend and the structure begins to collapse floor by floor, causing asymmetric deformations on the layers beneath.

An evaluation of the stress field in Figure 5.2a reveals higher loads in red tones near the vertices of the struts.

LS PrePost offers the option to visually display the loading state of individual elements within the structure, and thus, a triaxiality evaluation is also carried out. Figure 5.2b, with a range from -2/3

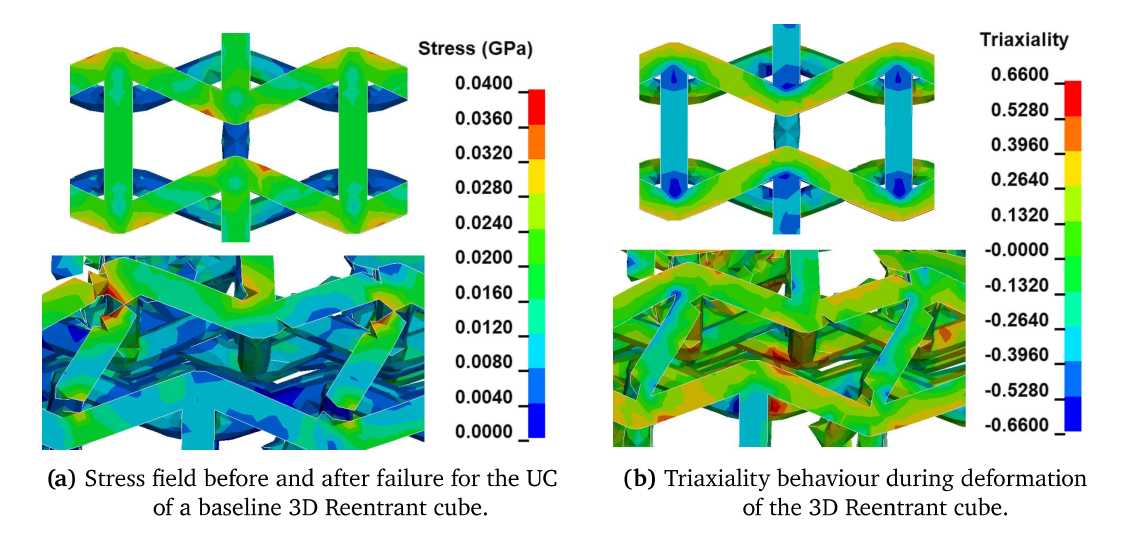


Figure 5.2: Comparison of (a) stress field evolution and (b) triaxiality behaviour in the 3D Reentrant cube.

to 2/3 indicates the direction of the stresses in each part of the UC. The vertical pillars in a light blue colour correspond to uniaxial compression loads, which drift to a more negative value toward the nodes and turn into biaxial compression due to the additional lateral forces from the angled struts. Uniaxial tension is present in the angle struts except for the transition regions, where pure shear (in green) takes over. The vast majority of the elements display the two load cases for which the materials were characterized: compression and tension. This further supports the decision to opt for material models like MAT_124, and confirms hypothesis 1-b).

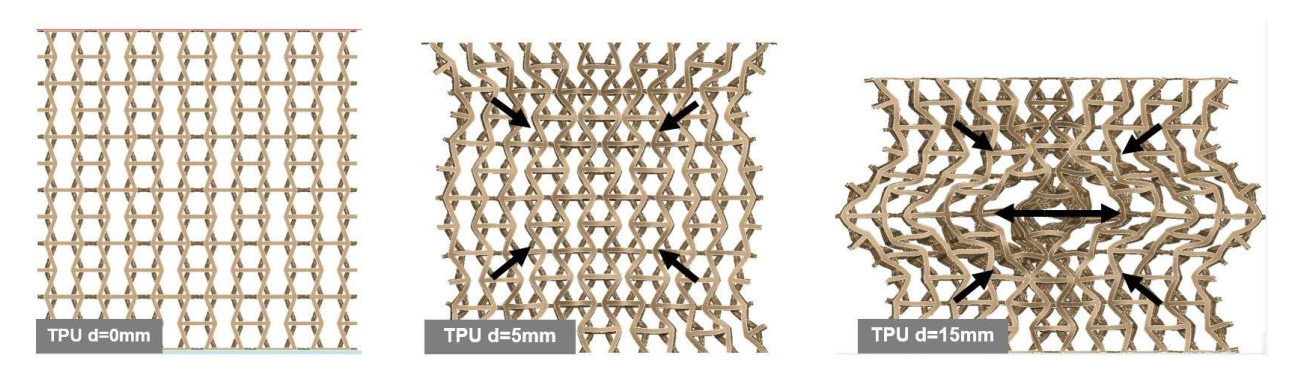


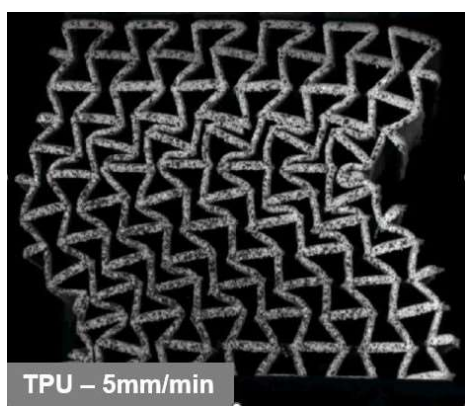
Figure 5.3: Crushing progression of the TPU 3D reentrant structure.

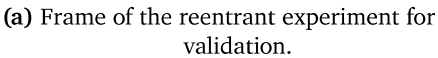
Among other observations, the auxetic effect of a lateral shrinkage under compression was more apparent with the softer TPU specimens. Figure 5.3 shows how, at a displacement of 5mm, the structure begins to deform toward its center from the sides. A global buckling of the structure appears, and presents evolving patterns that also change with parameters that will be discussed later. The relevance of the variability of stress states within the same structure at larger displacements, as the 15mm step displays, should also be noted, since the presence of stretch-dominated regions in the center of the cube will potentially have an advantage in terms of energy absorption over the localized bending that takes place in the periphery.

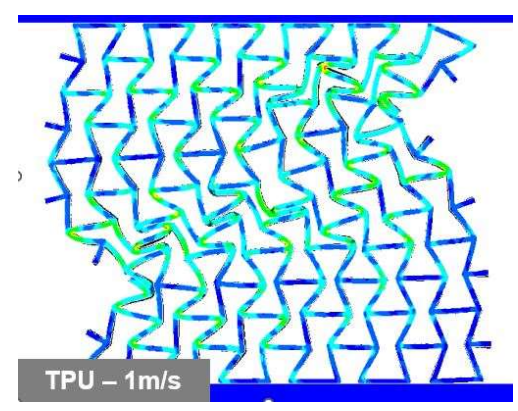
47

5.2 Experimental Validation

Despite the previous validation of the material models by means of a numerical simulation equivalent to the experimental setup. Additional validation is required to provide solid evidence that the complete simulation methodology, including material models, meshing procedure, contact definition, and boundary condition selection, is able to capture the deformation patterns and the global behaviour of the real structures both in a qualitative and a quantitative way.







(b) Frame from the equivalent step of the numerical simulation.

Figure 5.4: Comparison between (a) experimental and (b) numerical simulation validation results.

For this purpose, a crash test of a baseline reentrant structure was performed at the laboratory, and its force response was compared to the numerical equivalent.

Figure 5.4 reflects a similar deformation pattern for the experimental and the simulation cases, where the reentrant effect pulls from the sides of the cube inwards and from opposite directions in each of the laterals, resulting in the formation of an *S* pattern. The displacement on both top and bottom skip one row towards the center in the experimental case, but the sequence is completely analogous.

This accuracy is confirmed through the comparison of the response curves in Figure 5.5, with a strong correlation and a RMSE of approximately 0.9kN, therefore confirming the first hypothesis on the material model fidelity.

There are significant deviations in the PCF and fluctuations of the simulation curve throughout

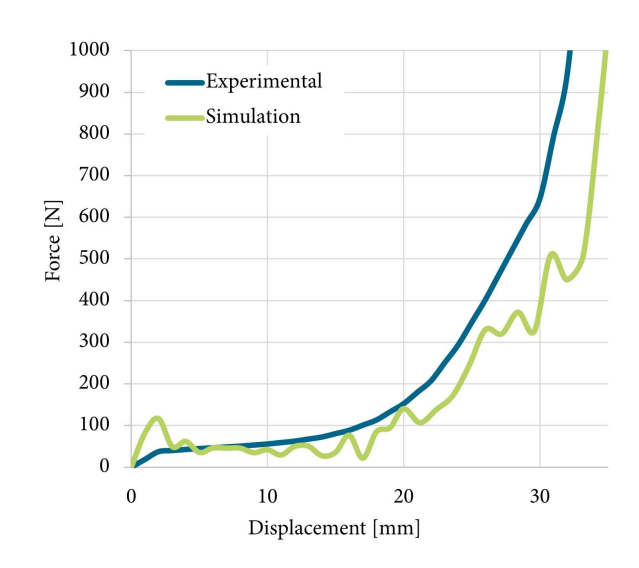
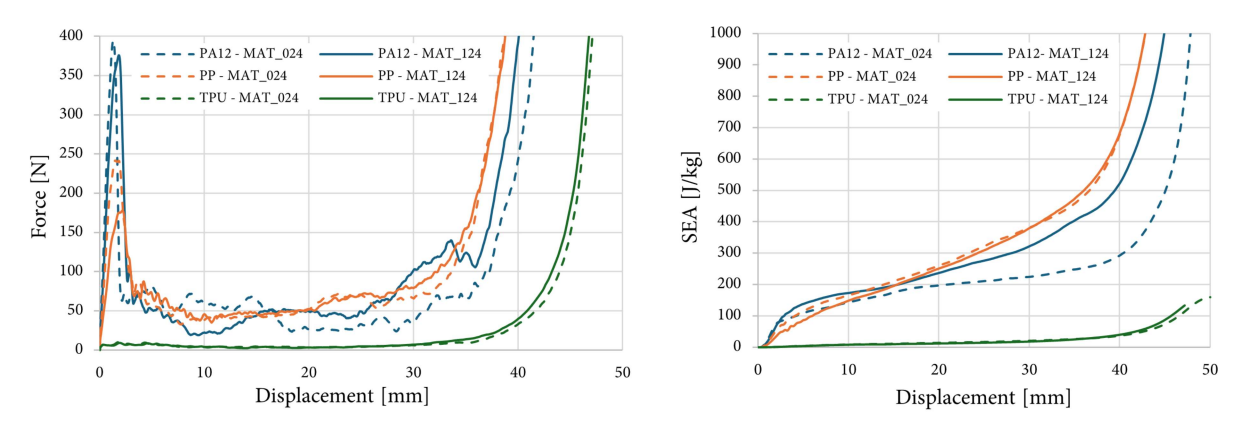


Figure 5.5: Experimental and numerical comparison of the force response.

the crushing plateau that can be attributed to the higher strain rates and the dynamic effects of the much faster displacement of the crushing plates in the case of the numerical counterpart.

5.3 Effect of the material model

To better understand the influence of the material models of choice, and to quantify the actual benefit of increasing its complexity by incorporating compression-tension differentiation, the same baseline simulations are run with the two material cards available for each polymer. Their force response and the evolution of their SEA with the displacement are represented in Figure 5.6.



- (a) Force–displacement response for the different material models.
- **(b)** SEA as a function of displacement for the different material models.

Figure 5.6: Comparison between (a) force–displacement behaviour and (b) SEA–displacement across material models.

The strongest difference in force response can be observed in the PA12 curves, which diverge significantly after failure initiates. Table 5.1 sumarizes the error in SEA between models across the three polymers, with PP and TPU displaying a deviation of approximately 10%, and PA12 a significant 92.63% increase in energy absorption after considering compression-tension properties.

| Material | SEA RMSE [J] | SEA RMSE [%] |
|----------|--------------|--------------|
| PA12 | 390,18 | 92,63 |
| PP | 46,92 | $9,\!65$ |
| TPU | 4,63 | 11,18 |

Table 5.1: RMSE of SEA between material models 024 and 124.

This phenomenon can be attributed to the particular failure strain of Nylon, which offers the lowest of all three materials, which also explains why the force response and the SEA curves only diverge from the PCF onwards.

5.4 Load Angle

3D Reentrant structures appear in literature with different orientations. The auxetic effect remains independently of the axis on which the structure is loaded, but differences in behaviour and potentially energy absorption are expected as stated in hypothesis 2-d). For this reason, the baseline structure is simulated at 0° and 90° and their responses are evaluated. Figure 5.7 shows a side by side comparison revealing a radical difference in the way the two variants deform and fail.

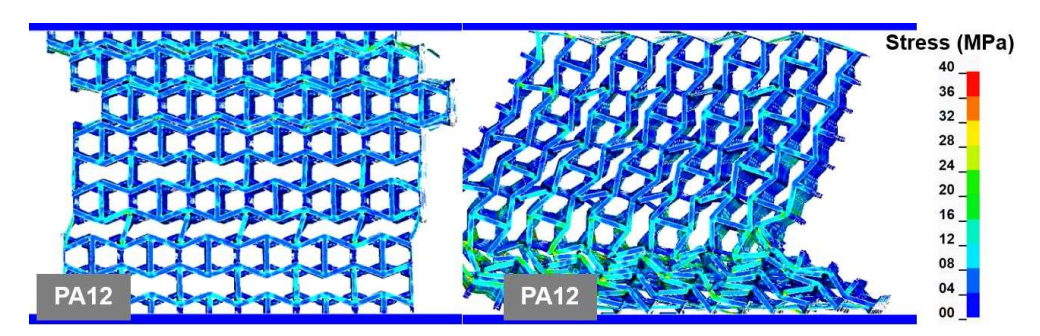


Figure 5.7: Stress contours at 10mm displacement for the 0° structure (left) and the 90° structure (right).

This difference is better understood by means of the force response in Figure 5.8a, where the subsequent collapse of the floors in the 0° structure leads to strong fluctuations throughout the crushing plateau, while the 90° structure exhibits a steady plateau at the expense of a higher PCF and an earlier densification.

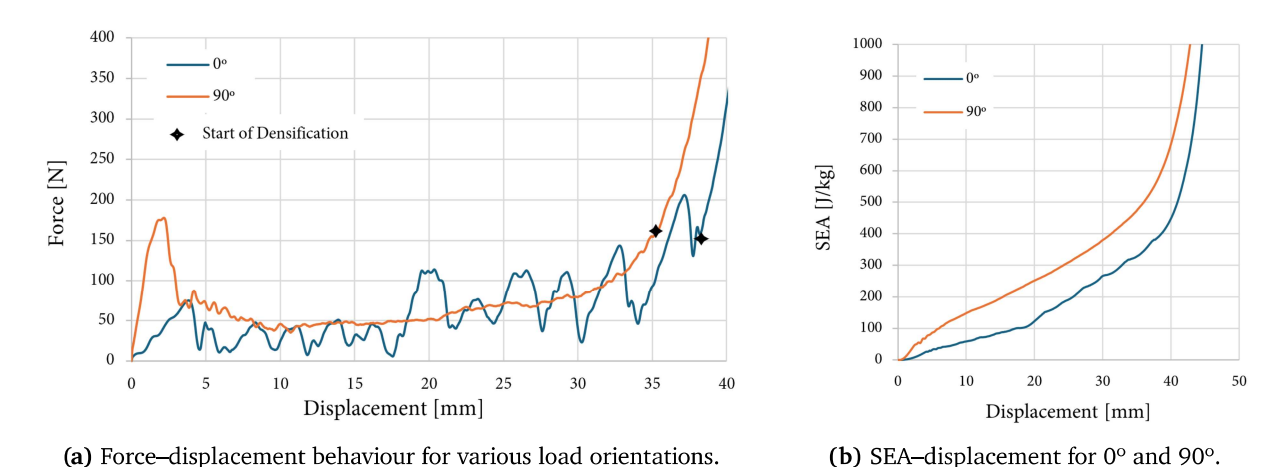


Figure 5.8: Performance comparison for different load angles.

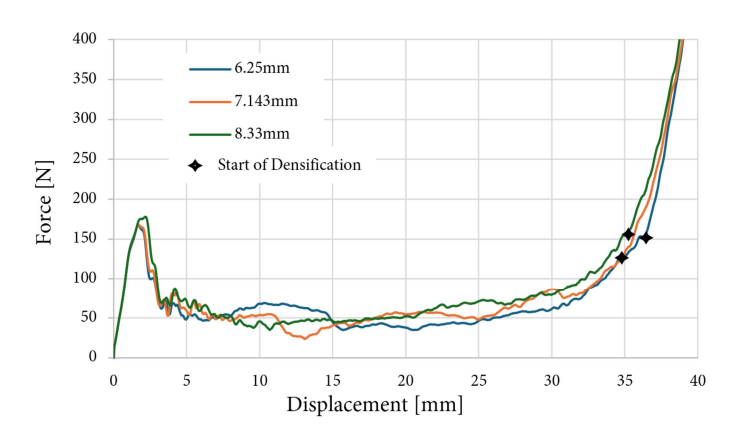
The rate at which the energy is absorbed during the crash, which is represented by the slope of the curves in Figure 5.8b is directly impacted by this, with the 90° providing a stable increase in SEA, resulting in an advantage of 25% over the original structure. Table 5.2 summarizes the main performance metrics and their variation with orientation and justifies the selection of the 90° load case for the continuation of the study.

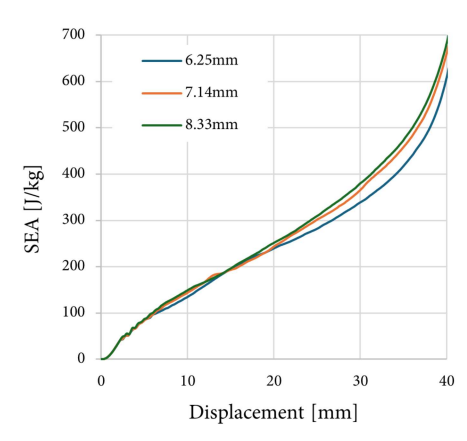
| Orientation | SEA [J/kg] | PCF [N] | MCF [N] |
|---------------|------------|---------|---------|
| 0° | 387 | 75 | 63 |
| 90° | 486 | 180 | 66 |
| Variation [%] | 25 | 138 | 5 |

Table 5.2: Effect of loading orientation on SEA, PCF, and MCF.

5.5 Unit Cell Base Size

The variation of the base size of the unit cells did not result in a significant change in the response of the structures, as evidenced by Figure 5.9. A slight increase in SEA with the cell size can be noticed only when normalizing by the mass of the structure, since a larger UC results in a lower number of cells required to fill an equivalent volume and therefore a reduced mass.





- (a) Force–displacement behaviour for different unit cell base sizes.
- (b) SEA-displacement response.

Figure 5.9: Performance comparison for different unit cell base sizes.

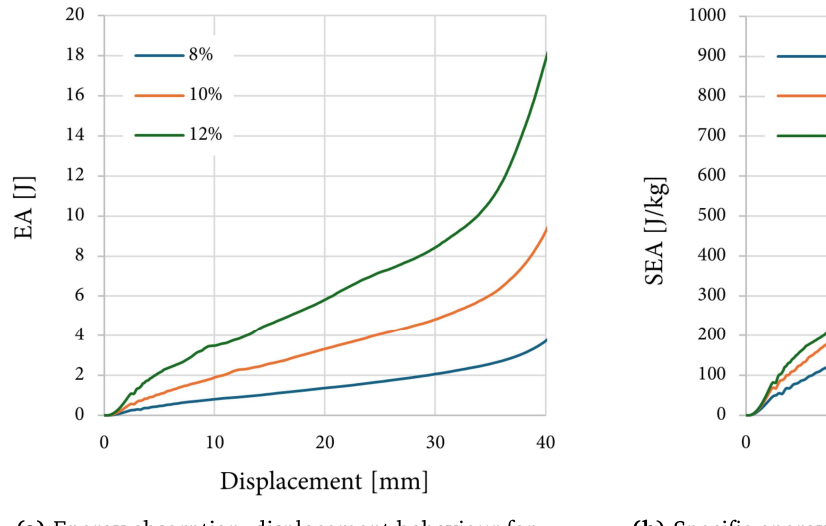
Table 5.3 includes SEA, PCF and MCF for the three variants using PP as the material of choice. The increased energy absorption of the larger base size can also be explained by the fact that at the same relative thickness, which is the case of all the considered structures, the absolute thickness of the larger cell is also higher, which is favorable as the following step of the discussion will prove. Therefore, hypothesis 2-a) can not be confirmed or refuted until further investigation takes place.

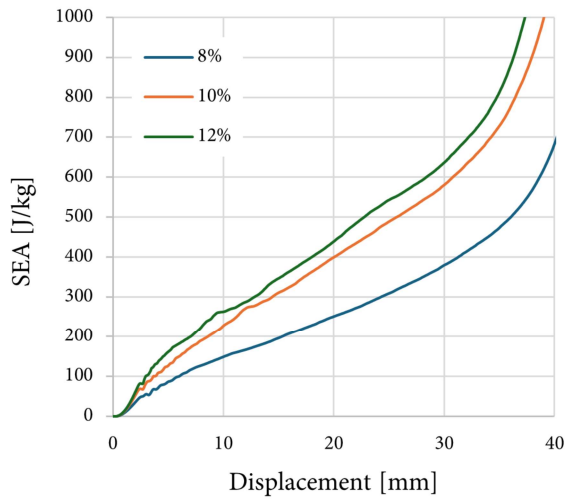
| Base Size [mm] | SEA [J/kg] | PCF [N] | MCF [N] |
|----------------|------------|---------|---------|
| 8,33 | 486 | 180 | 66 |
| $7{,}14$ | 443 | 170 | 59 |
| 6,25 | 436 | 170 | 57 |

Table 5.3: Influence of base size on SEA, PCF, and MCF.

5.6 Relative Thickness

The influence of the thickness of the struts in the performance of the auxetic is remarkable, and an interesting phenomenon takes place. The energy absorption increases with the relative thickness as seen in Figure 5.10a at a seemingly constant pace between steps.





- (a) Energy absorption—displacement behaviour for different relative thicknesses.
- **(b)** Specific energy absorption—displacement behaviour for different relative thicknesses.

Figure 5.10: Performance comparison for different relative thicknesses.

This is caused by similarly steady rise steps in PCF and MCF, as the force response in Figure 5.11 makes apparent. From the SEA plot in Figure 5.10b, however, the increased mass of the structure with the thicker struts cancels out some of the performance gains.

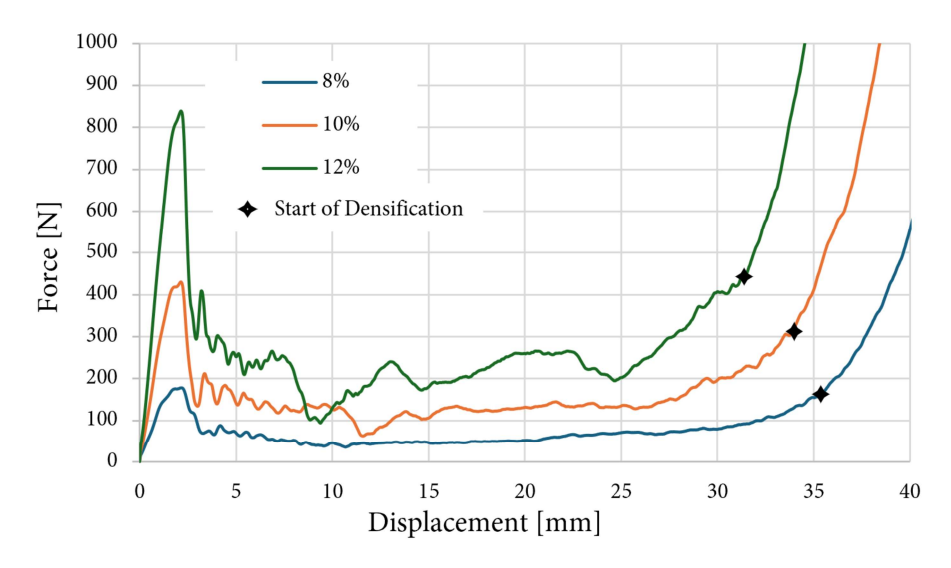


Figure 5.11: Force-displacement behaviour for different relative thicknesses.

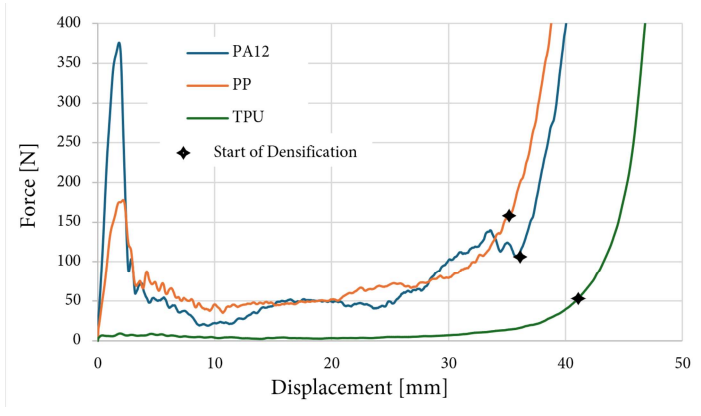
Together with the advancement of the densification phase in the case of the 12% cube, this yields a comparatively lower specific energy absorption. Table 5.4 confirms that there is an optimal relative thickness at a value of 10% of the base size, and ratifies hypothesis 2-b).

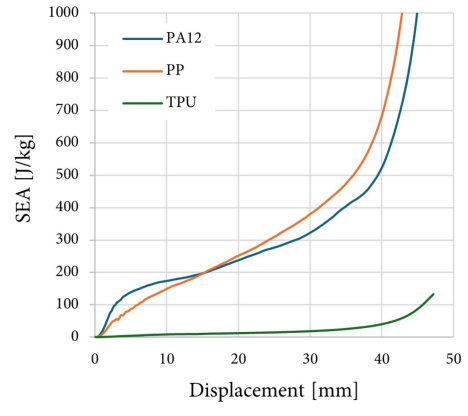
| Relative Thickness | SEA [J/kg] | PCF [N] | MCF [N] |
|--------------------|------------|---------|---------|
| 8% | 486 | 180 | 66 |
| 10% | 685 | 438 | 128 |
| 12% | 678 | 852 | 233 |

Table 5.4: Effect of relative thickness on SEA, PCF, and MCF.

5.7 Effect of the material properties

In this section, the effect of the different mechanical properties of the three polymers selected for the study is discussed. Each material exhibits particular mechanical characteristics when applied to the auxetic structures. PA12 and PP simulations result in similar behaviour in terms of force response, as presented in Figure 5.12a, with three key differences. The first and most relevant being the increased PCF of the Nylon, which amounts to more than double that of the PP, the second is the slightly increased MCF of the PP through the crushing plateau, and lastly, its earlier start of the densification.





(a) Force-displacement behaviour comparison.

(b) SEA-displacement comparison.

Figure 5.12: Performance comparison for different polymers.

TPU, on the other hand, offers a performance that differs by an order of magnitude. Its low elastic modulus and large elongation at break provides a reduced energy absorption capability, as presented in Figure 5.12b. Partially due to a slightly larger MCF and most importantly, to its density, which is the lowest of the three at only 0.89 g/cm³, PP delivers the highest SEA while offering a desirable reduction of the peak crushing force. Table 5.5 summarizes these metrics in further detail.

| Material | SEA [J/kg] | PCF [N] | MCF [N] |
|----------|------------|---------|---------|
| PA12 | 421 | 380 | 62 |
| PP | 486 | 180 | 66 |
| TPU | 41 | 9 | 5 |

Table 5.5: Comparison of SEA, PCF, and MCF for the polymer materials of the study.

5.8 Energy Dissipation

To assess the energy dissipation potential of auxetic structures and to make a distinction between it and the stored energy, the three polymers are again compared side by side, with the baseline 3D reentrant cube at an orientation of 90°. The simulation is configured so that the crushing plates compress the structure until the displacement that was previously identified as the point of start of densification, and in a way in which the force is released until reaching the initial gauge length. Figure 5.13 shows the last step of the numerical simulation for each material.

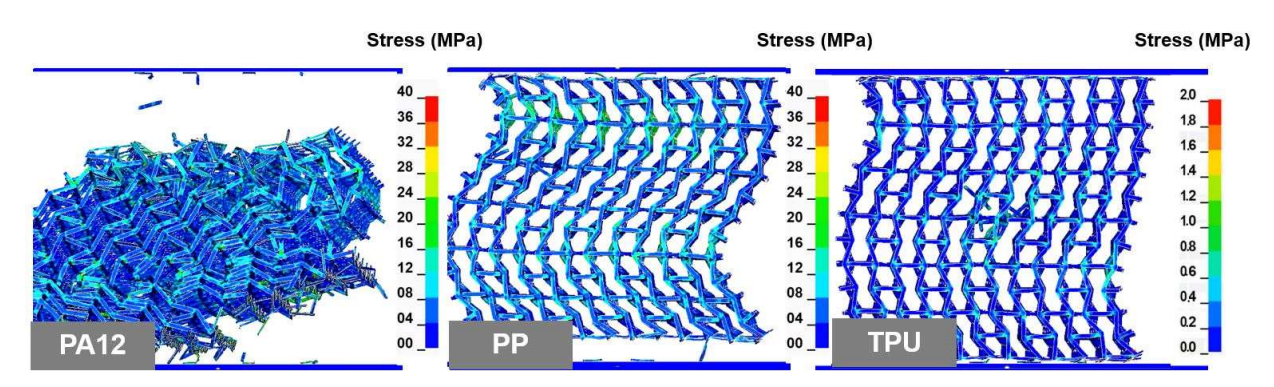


Figure 5.13: Last frame (d=0mm) of the dissipation simulation for the three materials of the study.

In Figure 5.14, the displacement is normalized by the densification displacement, and the areas under the two steps of the force-displacement curve are shaded to represent the energy stored (leaving the system when the plates are released) and the energy dissipated (the difference between the latter and the integration of the force from the origin to the densification). The polymers show decreasing levels of failure and non-recoverable strain from left to right

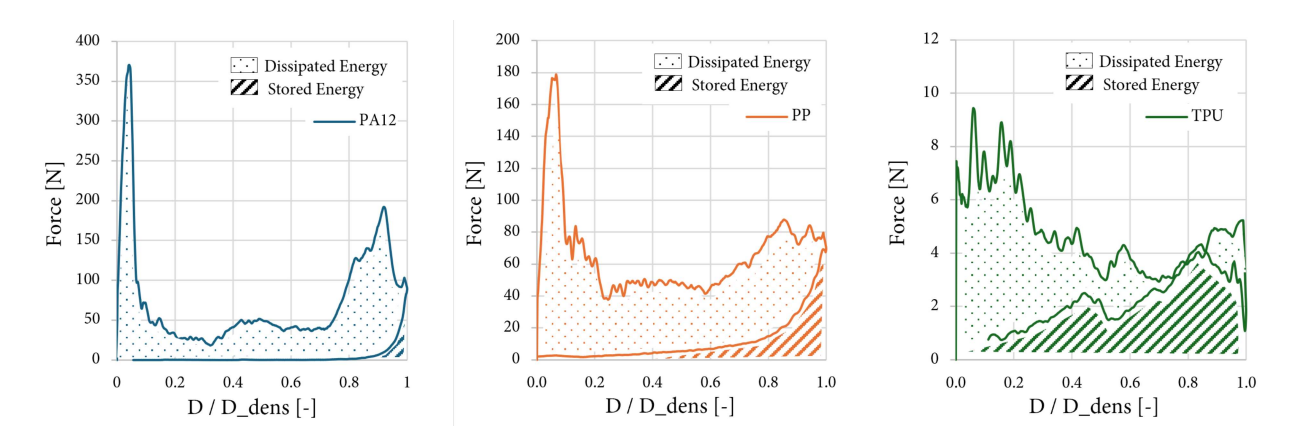


Figure 5.14: Force-Normalized displacement curves for the visualization of dissipated and stored energy of a 3D reentrant structure with the three materials of the study.

The differences observed across polymers are a direct result of their distinct mechanical properties. To gain a deeper understanding of the energy absorption mechanisms in each case, the internal energy and the eroded internal energy are again normalized by the mass of the auxetic structures and plotted separately in Figure 5.15. The internal energy curve is linked to the elastic and plastic deformation of the structure, while the eroded internal energy results from the failure of the elements within the geometry.

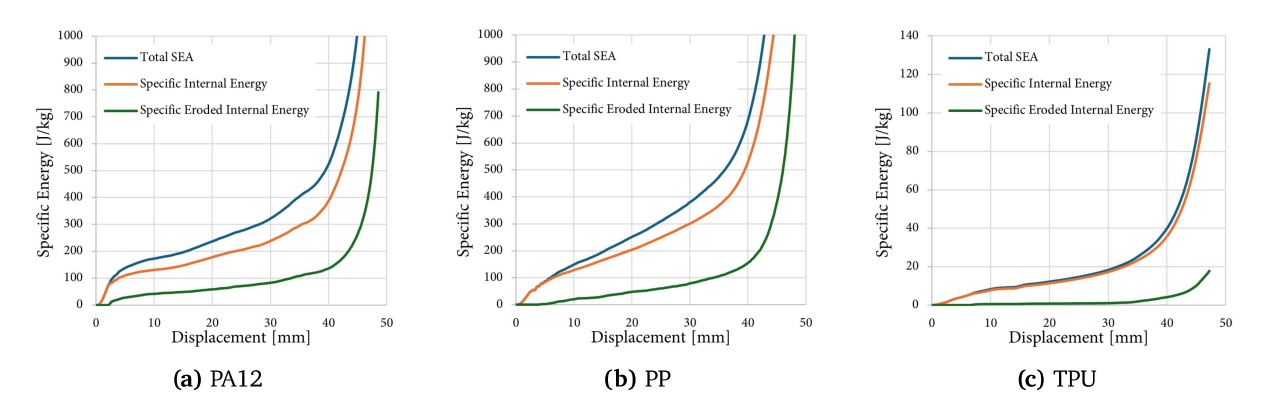


Figure 5.15: Breakdown of SEA-displacement behaviour for the three materials

The higher presence of erosion in the Nylon (linked to failure) explains its high dissipation ratio, and the same reasoning can be applied to the other materials, with TPU presenting very little contribution of the eroded energy to the total SEA, in line with the mostly elastic behaviour observed, with a minimal amount of non-recoverable strain. A quantitative comparison of the breakdown of SEA in stored and dissipated energy by each material can be found in Table 5.6, together with the calculated dissipation ratios.

| | PA12 | PP | TPU |
|---------------------------|----------|----------|----------|
| Total Internal Energy [J] | 2,67 | 2,11 | 0,12 |
| Dissipated Energy [J] | $2,\!56$ | 1,82 | 0,06 |
| Stored Energy [J] | $0,\!11$ | $0,\!28$ | $0,\!05$ |
| Dissipation Ratio | 96 % | 87 % | 53 % |

Table 5.6: Energy distribution in different polymer materials.

5.9 Performance Against 2D Structures

Since one of the main limitations for the application of lattice structures for real industrial use cases is the need for costly additive manufacturing processes to produce them, a secondary interest of this study lies in the comparison of 3D Reentrant cubes against two-dimensional variants that could theoretically be made by more scalable methods, such as plastic extrusion. To make this comparison more representative of the real challenges of a potential industrial implementation, a sec-

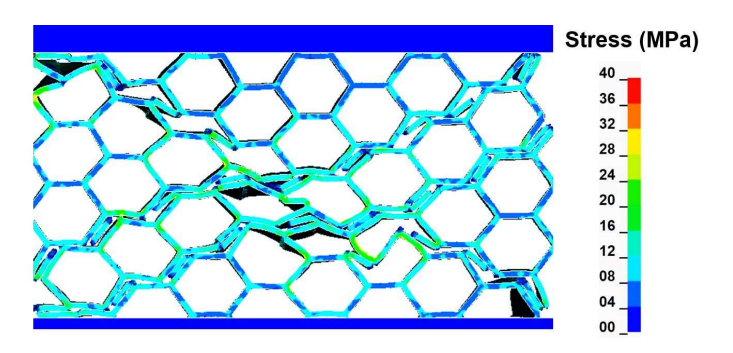


Figure 5.16: Contours of stress of a 2D honeycomb structure under crushing.

ond, commonly found 2D structure is also added to the performance evaluation: a honeycomb extrusion like the one seen in Figure 5.16.

The extrusion of the reentrant geometry results in a structure with much higher resistance, as depicted by Figure 5.17. A trend that is carried on to the energy absorption even after normalizing by the (much increased) mass of the cube. The classical hexagonal honeycomb studied yields a lower MCF and an unsteady crushing plateau, but its lower infill ratio, and the later densification that it presents both compensate for this fact.

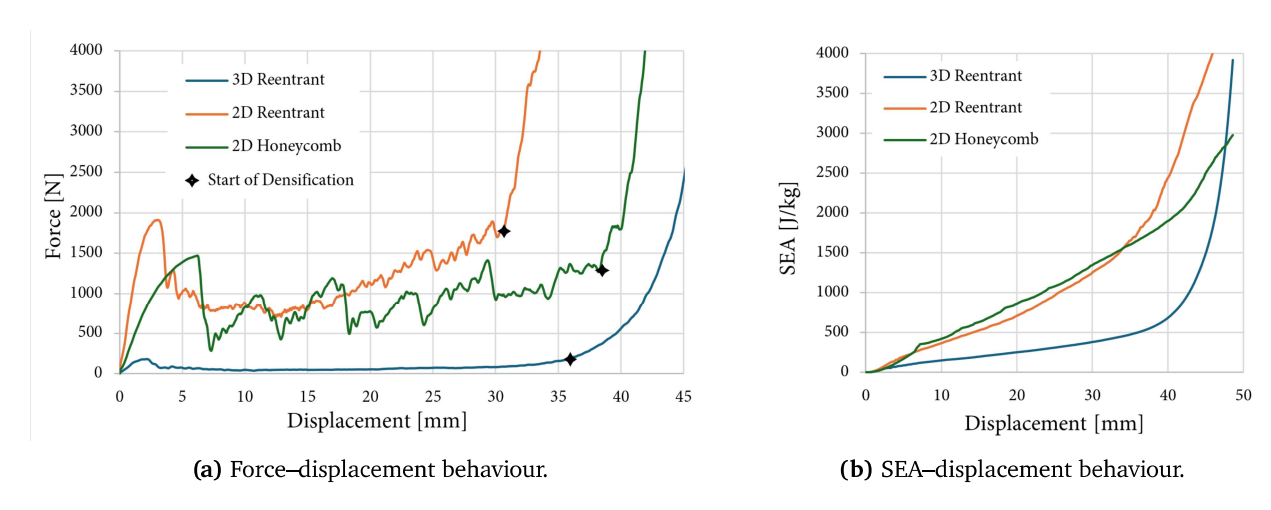


Figure 5.17: Performance comparison between 3D and 2D structures.

The results contradict the last hypothesis, stating that the larger number of deformation modes accessible to 3D structures could increase their performance, but the 2D Reentrant cubes possess a much higher mass for the same structural volume compared to the 3D variant, which makes them only suitable for certain applications. For a use case in which the increased infill is acceptable, a 2D type can offer a significant advantage in SEA, as Table 5.7.

| Structure | SEA [J/kg] | PCF [N] | MCF [N] |
|--------------|------------|---------|---------|
| 3D Reentrant | 486 | 180 | 66 |
| 2D Honeycomb | 1786 | 1473 | 872 |
| 2D Reentrant | 1283 | 1930 | 1468 |

Table 5.7: Comparison of 3D and 2D structures in terms of SEA, PCF, and MCF.

5.10 Performance Against Non-Auxetics

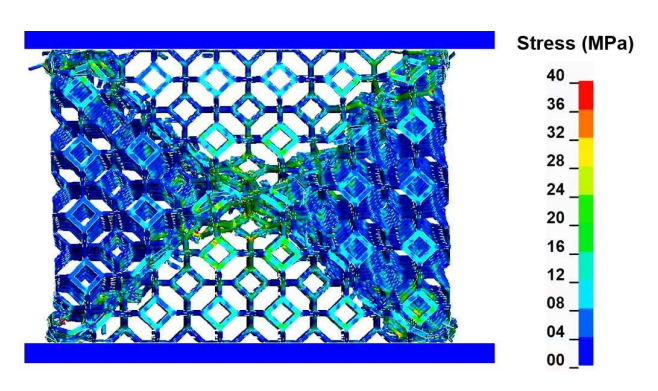


Figure 5.18: Contours of stress of a Kelvin Cell structure under crushing.

The parameters obtained from the non-auxetic 2D honeycomb suggested that other lattices with (regular) positive Poisson's ratio could also potentially outperform the auxetics of this study, and this was further analyzed by comparing the baseline 3D reentrant of 8% and (theoretically optimal) 10% relative thickness against an equivalent Kelvin lattice with 8% relative thickness, all of them using PP. Figure 5.18 shows the characteristic failure bands of the Kelvin lattice with contours of stress.

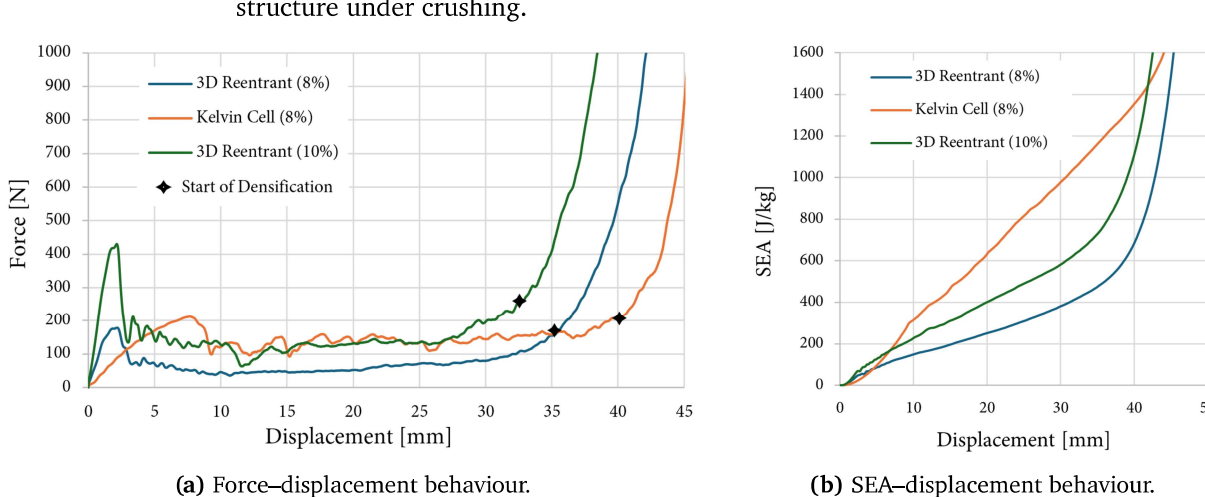


Figure 5.19: Performance comparison of 3D auxetic and non-auxetic structures.

The results, summarized in Figure 5.19, reveal the Kelvin lattice's typical behaviour, with a very contained peak crushing force that remains virtually constant throughout a remarkably long crushing plateau. The rate at which this structure absorbs energy is also worth highlighting, since the slope of its SEA curve in Figure 5.19b is quasi-linear.

| Structure | SEA [J/kg] | PCF [N] | MCF [N] |
|--------------------|------------|---------|---------|
| 3D Reentrant (8%) | 486 | 180 | 66 |
| Kelvin Cell | 1363 | 212 | 137 |
| 3D Reentrant (10%) | 685 | 438 | 128 |

Table 5.8: Comparison of structural configurations and their compressive performance.

All in all, the Kelvin lattice is better able to meet the crashworthyness criteria than the auxetics evaluated so far: a low PCF, a stable plateau, a late densification, and a steady energy absorption rate. Qualities that are further strengthened by the high SEA reached in comparison to the reentrant candidates, as Table 5.8 reads.

6 Conclusions

6.1 Summary

This research has provided an investigation into the energy absorption and dissipation potential of additively manufactured auxetic lattice structures, and a validated methodology for their numerical simulation. The progression from a simple material model to a compression-tension differentiated formulation demonstrated improvements in simulation accuracy for materials like PA12 where the difference in energy absorption predictions reached 92%.

The parametric investigation revealed that geometric optimization can improve auxetic performance. The identification of the superior 90° loading orientation and the determination of optimal relative thickness (10% of base size) provide specific design guidelines, with PP offering the best energy absorption and crashworthiness characteristics among the tested polymers.

An energy dissipation analysis revealed distinct results across materials, with PA12 achieving a high dissipation through extensive failure, PP providing a balanced performance, and TPU maintaining a largely elastic behavior suitable for recoverable energy absorption applications. The findings indicate that material selection must align with the intended energy management strategy.

The findings of this research have significant implications for the design and application of auxetic structures. While conventional structures like Kelvin cells and 2D honeycombs may demonstrate superior Specific Energy Absorption values, this comparison must be considered in the context of specific application requirements. The inferior performance of auxetics in energy absorption does not imply their lack of potential. In fact, their unique deformation capabilities, such as the effect of lateral contraction during compression, can provide advantages in specialized applications where maintaining structural alignment or preventing lateral damage propagation is crucial. Beyond this, auxetic structures display controlled and predictable deformation patterns. In scenarios where the onset of densification can be ignored, auxetics offer superior total energy absorption precisely due to their consistently early densification.

6.2 Challenges

Manufacturing represented one of the most substantial logistical challenges. The reliance on HSS equipment from another department was the origin of various scheduling constraints and a limited experimental flexibility. Print failures, such as the example of Figure 6.1, which occurred occasionally due to the delicate balance between the printing parameters, resulted in significant delays as new print jobs required further coordination. The situation was particularly complicated for PP specimens, which had to be externally sourced due to material compatibility, resulting in additional costs and extended lead times that impacted the experimental timeline.



Figure 6.1: A first PA12 print fail caused by the recoater dragging one of the parts.

The optimization of DIC acquisition parameters also presented technical challenges, particularly in combining temporal resolution with the management of the data volume. The wide range of strain rates employed (5-500 mm/min) required different strategies for each test series. Calculating the optimal shutter speeds and frame decimation factors required preliminary tests to ensure that the relevant deformation events, like failure, were captured without generating large data volumes.

The lighting setup was challenging aswell for compression specimens due to their small size (10mm diameter), requiring custom positioning of the LED arrays and careful attention to avoid shadows that could compromise correlation quality. The large elongation of TPU presented unique challenges for DIC implementation on these highly deformable specimens. TPU's ability to undergo elongations exceeding 100% caused sections of the gauge length to leave the calibrated field of view as deformation progressed. This resulted in a trade-off between spatial resolution and measurement range. A wider FOV reduces the risk of losing specimen areas during large strains, but at the cost of lower spatial resolution and a lower sensitivity to local strain concentrations. On the contrary, a narrower field of view maximized resolution and accuracy in early deformation stages but increased the likelihood of losing critical specimen areas during extreme elongation.

The adopted solution involved optimizing the FOV for each material in order to capture the complete gauge length at least through yield and early plastic deformation, assuming some visibility loss in the final stages for TPU specimens, while ensuring the essential stress-strain response could be captured.

LS-DYNA Material Model Implementation also encountered specific difficulties with PP due to its complex nonlinear plasticity behavior. The decreasing load curve after ultimate tensile strength (LCDT) caused convergence issues within the solver and generated multiple error messages and simulation terminations. The decrease of true stress with increasing plastic strain after reaching maximum strength violated assumptions built into the material model algorithms. The solution required artificial modification of the stress-strain curve to impose a minimal positive slope,

Contact definition optimization proved to be critical for an accurate simulation, requiring experimentation with different contact algorithms. The complex geometry and large deformations made standard contact formulations prone to unrealistic interpenetration.

6.3 Applications

The findings of this research can be translated to application domains where the characteristics of auxetic structures provide advantages over conventional alternatives. Crash energy management systems represent a potential application area in scenarios where lateral damage containment is critical. Auxetic structures could absorb impact energy while ensuring that debris remains contained within the designated zone, preventing damage to fuel lines, electrical systems, or intrusion into passenger compartments.

Structural sandwich cores present another compelling application, particularly utilizing 2D reentrant configurations demonstrated to achieve higher SEA values over 1200 J/kg. These structures could serve as cores in composite sandwich panels where the auxetic behavior is present in the plane of the composite face sheets while excellent compressive strength is maintained in the throughthickness direction of the extrusion.

6.4 Outlook

There are promising directions for future research that could significantly improve the understanding of energy absorption in 3D printed auxetics, beginning with the addition of alternative unit cell configurations with gradient thickness beams, curved struts, or hybrid configurations in which multiple auxetic mechanisms are combined. This could be followed by the refinement of the contact formulation, a critical aspect given the early densification observed, which creates complex contact interactions.

A deeper investigation into the thickness optimization should address the question of whether the optimal relative thickness of 10% identified in this study responds to a geometric scaling law or an absolute dimensional effect. The observed densification effects leading to the hindered performance of the thicker variant suggest the first option, but confirmation requires dedicated investigation.

Finally, future improvements to the material characterization could incorporate shear properties and manufacturing anisotropy into advanced. The triaxiality analysis revealed reduced and localized but present shear stress states within auxetic structures. Implementation of shear testing data, potentially using the MAT_187 (SAMP-1) formulation, could improve simulation accuracy. And the addition of the anisotropic behavior of 3D prints remains one of the main limitations of material cards for LS-DYNA, since there is currently no option for a compression-tension model with added anisotropy.

Bibliography

- [1] Michael F. Ashby. *Materials Selection in Mechanical Design*. 5th. Oxford, UK: Butterworth-Heinemann, 2016. ISBN: 978-0-08-100599-6.
- [2] Paolo Bettini et al. "Composite chiral structures for morphing airfoils: Numerical analyses and development of a manufacturing process". In: *Composites Part B: Engineering* 41 (2 Mar. 2010), pp. 133–147. ISSN: 1359-8368. URL: https://www.sciencedirect.com/science/article/abs/pii/S1359836809001899.
- [3] M Böddecker et al. "Highlights Effect of uncertainty of material parameters on stress triaxiality and Lode angle in finite elasto-plasticity-a variance-based global sensitivity analysis Effect of uncertainty of material parameters on stress triaxiality and Lode angle in finite elasto-plasticity-a variance-based global sensitivity analysis". In: *TU Dortmund University* (2024).
- [4] M J Bots. "Energy Absorption of Additively Manufactured Lattices Master Thesis". In: *Delft University of Technology* (2017).
- [5] J. Carlsson, V. S. Deshpande, and N. A. Fleck. "The compressive response of the filled Kelvin foam". In: *European Journal of Mechanics A/Solids* 104 (Mar. 2024), p. 105018. ISSN: 0997-7538. URL: https://www.sciencedirect.com/science/article/pii/S0997753823001109.
- [6] Hyeonho Cho, Dongsik Seo, and Do-Nyun Kim. "Mechanics of Auxetic Materials". In: *Hand-book of Mechanics of Materials* (2018), pp. 1–25. URL: https://link.springer.com/rwe/10.1007/978-981-10-6855-3_25-1.
- [7] CREVAD Crash Evaluierung Alternativer CFK-Rumpf Designs. 2014. URL: https://www.dlr.de/de/bt/forschung-transfer/projekte/projekt-archiv/crevad.
- [8] J Cronau and · F Engstler. "Energy absorption of 3D printed stochastic lattice structures under impact loading design parameters, manufacturing, and testing". In: *Progress in Additive Manufacturing* (2025). URL: https://doi.org/10.1007/s40964-025-01094-5.
- [9] V. S. Deshpande, M. F. Ashby, and N. A. Fleck. "Foam topology: bending versus stretching dominated architectures". In: *Acta Materialia* 49 (6 Apr. 2001), pp. 1035–1040. ISSN: 1359-6454. URL: https://www.sciencedirect.com/science/article/abs/pii/S1359645400003797.
- [10] Shanshan Dong and Hong Hu. "Sensors Based on Auxetic Materials and Structures: A Review". In: *Materials 2023, Vol. 16, Page 3603* 16 (9 May 2023), p. 3603. ISSN: 1996-1944. URL: https://www.mdpi.com/1996-1944/16/9/3603/htm%20https://www.mdpi.com/1996-1944/16/9/3603.
- [11] LS-DYNA. From engineering to true strain, true stress. 2002. URL: https://www.dynasupport.com/howtos/material/from-engineering-to-true-strain-true-stress.
- [12] K. E. Evans et al. "Molecular network design". In: *Nature* 353.6340 (1991), p. 124.

- [13] Ken Evans and Andrew Alderson. "Auxetic Materials: Functional Materials and Structures from Lateral Thinking!" In: *Advanced Materials* 12 (May 2000), pp. 617–628.
- [14] J.N. Grima. AUXETIC MATERIALS. 2000. URL: https://staff.um.edu.mt/jgri1/auxetic_f2.html.
- [15] James N. Grima-Cornish et al. "Auxetic Behavior and Other Negative Thermomechanical Properties from Rotating Rigid Units". In: *Physica Status Solidi Rapid Research Letters* 16 (2 Feb. 2022), p. 2100322. ISSN: 18626270. URL: /doi/pdf/10.1002/pssr.202100322% 20https://onlinelibrary.wiley.com/doi/abs/10.1002/pssr.202100322%20https://onlinelibrary.wiley.com/doi/10.1002/pssr.202100322.
- [16] R. S. Lakes. "Foam Structures with a Negative Poisson's Ratio". In: *Science* 235.4792 (1987), pp. 1038–1040.
- [17] Jiaxing Li et al. "An elongation-shortening strategy modifying the deformation mechanism of cellular structure for excellent energy absorption". In: *Virtual and Physical Prototyping* 20 (1 Dec. 2025). ISSN: 17452767. URL: https://www.tandfonline.com/doi/pdf/10. 1080/17452759.2025.2503259.
- [18] Carolin Lupprian. "Prediction of Mechanical Properties for tape-layered Specimen using Finite Element Method and Machine Learning". In: *Karlsruhe Institute of Technology* (2025).
- [19] Xin Ren et al. "Auxetic metamaterials and structures: a review". In: *Smart Materials and Structures* 27 (Jan. 2018).
- [20] Abdulrasheed Suleiman Shuaibu et al. "Advancing auxetic materials: Emerging development and innovative applications". In: *Reviews on Advanced Materials Science* 63 (1 Jan. 2024).

 ISSN: 16058127. URL: https://www.researchgate.net/publication/381340557_

 Advancing_auxetic_materials_Emerging_development_and_innovative_applications.
- [21] A. B.M. Supian et al. "Hybrid reinforced thermoset polymer composite in energy absorption tube application: A review". In: *Defence Technology* 14 (4 Aug. 2018), pp. 291–305. ISSN: 2214-9147. URL: https://www.sciencedirect.com/science/article/pii/S2214914718300230.
- [22] Livermore Software Technology. LS-DYNA Keyword User's Manual. 2021. URL: https://www.dynasupport.com/manuals.
- [23] Livermore Software Technology. LS-DYNA Material Models. 2025. URL: https://www.dynasupport.com/manuals.
- [24] Livermore Software Technology. LS-DYNA Theory Manual. 2023. URL: https://www.dynasupport.com/manuals.
- [25] Xing Chi Teng et al. "A simple 3D re-entrant auxetic metamaterial with enhanced energy absorption". In: *International Journal of Mechanical Sciences* 229 (Sept. 2022), p. 107524. ISSN: 0020-7403. URL: https://www.sciencedirect.com/science/article/abs/pii/S0020740322004222.
- [26] Sunao Tomita et al. "Transition of deformation modes from bending to auxetic compression in origami-based metamaterials for head protection from impact". In: *Scientific Reports* 13 (1 Dec. 2023), pp. 1–12. ISSN: 20452322. URL: https://www.nature.com/articles/s41598-023-39200-8.

- [27] Iman Valizadeh and Oliver Weeger. "Rate-dependent energy dissipation of graded viscoelastic structures fabricated by grayscale vat photopolymerization". In: *Smart Materials and Structures* 33 (6 June 2024). ISSN: 1361665X.
- [28] Voxeljet. VX200 HSS The 3D printing system for plastics | voxeljet. 2020. URL: https://www.voxeljet.com/industrial-3d-printer/prototyping/vx200-hss/.
- [29] Tao Wang et al. "Dynamic Crushing Analysis of a Three-Dimensional Re-Entrant Auxetic Cellular Structure". In: *Materials 2019, Vol. 12, Page 460* 12 (3 Feb. 2019), p. 460. ISSN: 1996-1944. URL: https://www.mdpi.com/1996-1944/12/3/460.
- [30] Oliver Weeger et al. "Inelastic finite deformation beam modeling, simulation, and validation of additively manufactured lattice structures". In: *Additive Manufacturing Letters* 4 (Feb. 2023). ISSN: 27723690.
- [31] Xiaolong Zhang et al. "Dynamic Response and Energy Absorption of Lattice Sandwich Composite Structures Under Underwater Explosive Load". In: *Materials 2025, Vol. 18, Page 1317* 18 (6 Mar. 2025), p. 1317. ISSN: 1996-1944. URL: https://www.mdpi.com/1996-1944/18/6/1317.

Annex

A Material Model Parameters

| LS Code | Name | MAT_024 | MAT_124 | MAT_187 |
|----------|---|---------|---------|---------|
| MID | Material ID | X | X | X |
| RO | Density | X | X | X |
| E | Young's Modulus | X | X | X |
| EC | Young's Modulus (Compression) | | X | |
| PR | Poisson Ratio | X | X | X |
| NUEP | Poisson Ratio (Transversal to Longitudinal) | | | X |
| SIGY | Yield Stress | X | | |
| ETAN | Tangent Modulus | X | | |
| C | Strain Rate parameter | X | X | |
| P | Strain Rate parameter | X | X | |
| LCSS | Eff Stress vs Eff Plastic Strain | X | | |
| LCSR | Strain Rate vs Yield Stress | X | | |
| LCIDC | Eff Stress vs Eff Plastic Strain (Compression) | | X | X |
| LCIDT | Eff Stress vs Eff Plastic Strain (Tension) | | X | X |
| LCSRC | Strain Rate vs Yield Stress (Compression) | | X | |
| LCSRT | Strain Rate vs Yield Stress (Tension) | | X | |
| LCFAIL | Plastic Strain at failure vs Strain Rate | | X | |
| PC | Compressive Mean Stress | | X | |
| PT | Tensile Mean Stress | | X | |
| PCUTT | Pressure cut-off in compression | | X | |
| PCUTF | Pressure cut-off in tension | | X | |
| LCID-C | Yield Stress vs Plastic Strain (Compression) | | | X |
| LCID-S | Yield Stress vs Plastic Strain (Shear) | | | X |
| LCID-B | Yield Stress vs Plastic Strain (Biax Tension) | | | X |
| LCID-P | Plastic Poisson Ratio vs Plastic Strain (Tension) | | | X |
| LCID-D | Damage Parameter vs Plastic Strain (Tension) | | | X |
| EPFAIL | Plastic Strain at Failure | | | X |
| DEPRPT | Δ of Eq Plastic Strain from failure to rupture | | | X |
| LCID_LC | Scaler of EPFAIL as a function of Characteristic Element Length | | | X |
| LCID_TRI | Scaler of EPFAIL as a function of Triaxiality | | | X |
| LCEMOD | Young's modulus vs Effective Strain Rate | | | X |

Table 1: Summary of parameters in the 3 material models considered for the study

B Material Cards

```
Material card for TPU - 124
*MAT_PLASTICITY_COMPRESSION_TENSION_TITLE
Card Template
$#
       mid
                  ro
                              е
                                       pr
                                                   С
                                                              р
                                                                     fail
            1.120e-6
        10
                         0.0211
                                     0.38
$#
     lcidc
               lcidt
                          lcsrc
                                    lcsrt
                                              srflag
                                                        lcfail
                                                                       ec
        14
                  15
                                                 0.0
                                                                  0.01744
$#
                  pt
                                               pcutf
        рс
                          pcutc
                                    pcutt
$#
         k
*DEFINE_CURVE_TITLE
LCIDT
        15
$#
                                        ი1
                  a1
                            0.00112867536
         0.001846408
                            0.00122330000
         0.005762774
         0.009679140
                            0.00127880000
         0.013595506
                            0.00131530000
         0.017511872
                            0.00137010000
         0.021428238
                            0.00142480000
         0.025344604
                            0.00147303384
         0.029260970
                            0.00151230108
         0.033177336
                            0.00155076537
         0.037093702
                            0.00163360000
         0.041010068
                            0.00166820886
         0.044926434
                            0.00169900000
         0.048842800
                            0.00173856379
         0.052759166
                            0.00177090000
         0.056675532
                            0.00181878069
                            0.00185860000
         0.060591898
         0.064508264
                            0.00191226193
         0.068424630
                            0.00193468655
         0.072340996
                            0.00200150118
         0.076257362
                            0.00201508873
         0.080173728
                            0.00204718619
         0.084090094
                            0.00207169983
         0.088006460
                            0.00211397978
         0.091922826
                            0.00214497450
         0.095839192
                            0.00220604754
         0.099755559
                            0.00223474326
         0.103671925
                            0.00227052458
         0.107588291
                            0.00230533840
         0.111504657
                            0.00233262677
                            0.00236758266
         0.115421023
```

| ı | | |
|---|---------------------|---------------|
| | 0.119337389 | 0.00240229010 |
| | 0.123253755 | 0.00242434673 |
| | 0.127170121 | 0.00248508292 |
| | 0.131086487 | 0.00252929848 |
| | 0.135002853 | 0.00253808572 |
| | 0.138919219 | 0.00258036907 |
| | 0.142835585 | 0.00264020998 |
| | 0.146751951 | 0.00267167662 |
| | 0.150668317 | 0.00268571449 |
| | 0.154584683 | 0.00271660664 |
| | 0.158501049 | 0.00276668613 |
| | 0.162417415 | 0.00278037719 |
| | 0.166333781 | 0.00280828296 |
| | 0.170250147 | 0.00286035534 |
| | 0.174166513 | 0.00290367784 |
| | 0.178082879 | 0.00291825638 |
| | 0.181999245 | 0.00294612919 |
| | 0.185915611 | 0.00297855248 |
| | 0.189831977 | 0.00298222993 |
| | 0.193748343 | 0.00301546950 |
| | *DEFINE_CURVE_TITLE | 5.5555.540700 |
| | LCIDC | |
| | 14 | |
| | \$# a1 | 01 |
| | 0.00692406 | 0.00303566 |
| | 0.05019457 | 0.00346054 |
| | 0.09346508 | 0.00385858 |
| | 0.13673560 | 0.00425436 |
| | 0.18000611 | 0.00425436 |
| | 0.22327663 | 0.00509027 |
| | 0.26654714 | 0.00553632 |
| | 0.30981766 | 0.00599717 |
| | 0.35308817 | |
| | | 0.00646726 |
| | 0.39635868 | 0.00693760 |
| | 0.43962920 | 0.00740957 |
| | 0.48289971 | 0.00792362 |
| | 0.52617023 | 0.00851204 |
| | 0.56944074 | 0.00917241 |
| | 0.61271125 | 0.00982678 |
| | 0.65598177 | 0.01050997 |
| | 0.69925228 | 0.01120609 |
| | 0.74252280 | 0.01193323 |
| | 0.78579331 | 0.01266082 |
| | 0.82906383 | 0.01346095 |
| | 0.87233434 | 0.01434386 |
| | 0.91560485 | 0.01529771 |
| | 0.95887537 | 0.01630652 |
| | 1.00214588 | 0.01741581 |
| | 1.04541640 | 0.01860540 |
| | 1.08868691 | 0.01988418 |
| I | 1.0000001 | 0.01700410 |

```
0.02126493
          1.13195742
          1.17522794
                                0.02276461
          1.21849845
                                0.02435230
          1.26176897
                                0.02605844
          1.30503948
                                0.02788924
          1.34831000
                                0.02982855
          1.39158051
                                0.03194864
          1.43485102
                                0.03420146
                                0.03660688
          1.47812154
          1.52139205
                                0.03914946
          1.56466257
                                0.04197170
          1.60793308
                                0.04487096
          1.65120360
                                0.04807970
          1.69447411
                                0.05151022
          1.73774462
                                0.05501191
          1.78101514
                                0.05887024
          1.82428565
                                0.06314746
          1.86755617
                                0.06777733
          1.91082668
                                0.07242994
          1.95409719
                                0.07755320
          1.99736771
                                0.08314660
          2.04063822
                                0.08930928
          2.08390874
                                0.09600374
          2.12717925
                                0.10207777
$
$
*MAT_ADD_EROSION
$
       mid
                 excl
                                               effeps
                                                          voleps
                         mxpres
                                     mneps
        10
$
    mnpres
                sigp1
                           sigvm
                                     mxeps
                                                epssh
                                                           sigth
$
      idam
               dmgtyp
                           lcsdg
                                     ecrit
                                               dmgexp
                                                           dcrit
        -1
$
     dityp
                              p2
                                         рЗ
                   p1
                   99
$
     detyp
                dctyp
                                         q2
                              q1
                           5e-05
         1
*DEFINE_CURVE_TITLE
Triaxiality curve of undamaged material
        99
                   -1
                                    10.000
                -0.33
                                     5.000
                    0
                               0.193748343
                 0.33
                               0.193748343
                               0.193748343
$
$
*END
```

```
$-----
   Material card for PA12 - 124
$-----
*MAT_PLASTICITY_COMPRESSION_TENSION_TITLE
Card Template
$#
      mid
                                                            fail
                ro
                          е
                                  pr
                                           С
                                                     р
       10
          1.010e-6
                      1.495
                              0.3618
$#
                                                 lcfail
    lcidc
             lcidt
                      lcsrc
                               lcsrt
                                        srflag
                                                              ec
                                          0.0
       14
                15
                                  16
                                                         1.07705
$#
                                         pcutf
       рс
                pt
                      pcutc
                               pcutt
$#
        k
Ś
*DEFINE_CURVE_TITLE
LCSRT
       16
$#
                a1
                                  о1
       1.488095e-06
                                   1
       1.488095e-05
                             1.062916
       1.488095e-04
                             1.503105
              1000
                             1.503105
*DEFINE_CURVE_TITLE
LCIDT
       15
$#
                а1
                                  о1
          0.002358
                             0.029059
          0.002625
                             0.029591
          0.002943
                             0.030188
          0.003240
                             0.030639
          0.003692
                             0.031100
          0.004118
                             0.031467
          0.004635
                             0.031910
          0.005079
                             0.032269
          0.005648
                             0.032659
          0.006106
                             0.033000
          0.006625
                             0.033428
          0.007178
                             0.033847
          0.007675
                             0.034166
          0.008320
                             0.034528
          0.008870
                             0.034767
          0.009546
                             0.035027
          0.010102
                             0.035278
          0.010765
                             0.035555
          0.011354
                             0.035766
          0.012035
                             0.036046
          0.012734
                             0.036284
          0.013375
                             0.036468
```

| | 0.014134 | 0.036696 | |
|-------|----------------|----------------------|--|
| | 0.014766 | 0.036888 | |
| | 0.015500 | 0.037114 | |
| | 0.016160 | 0.037291 | |
| | 0.016862 | 0.037462 | |
| | 0.017467 | 0.037615 | |
| | 0.018179 | 0.037825 | |
| | 0.018805 | 0.037978 | |
| | 0.019555 | 0.038161 | |
| | 0.020372 | 0.038315 | |
| | 0.021083 | 0.038455 | |
| | 0.021902 | 0.038609 | |
| | 0.022598 | 0.038743 | |
| | 0.023418 | 0.038904 | |
| | 0.023410 | 0.039008 | |
| | 0.025025 | 0.039050 | |
| | 0.025709 | 0.039270 | |
| | 0.025709 | 0.039387 | |
| | | 0.039548 | |
| | 0.027336 | 0.039548 0.039666 | |
| | 0.028042 | | |
| | 0.028886 | 0.039752 | |
| | 0.029596 | 0.039854 | |
| | 0.030437 | 0.039960 | |
| | 0.031176 | 0.040049 | |
| | 0.032111 | 0.040148 | |
| | 0.032988 | 0.040234 | |
| | 0.034166 | 0.040336 | |
| | 0.035687 | 0.040444 | |
| | NE_CURVE_TITLE | | |
| LCIDC | | | |
| | 14 | | |
| \$# | a1 | 01 | |
| | 0.00215147 | 0.04830621 | |
| | 0.03737327 | 0.05885951 | |
| | 0.07259508 | 0.06267896 | |
| | 0.10781688 | 0.06429436 | |
| | 0.14303869 | 0.06500621 | |
| | 0.17826049 | 0.06542731 | |
| | 0.21348230 | 0.06581312 | |
| | 0.24870410 | 0.06627164 | |
| | 0.28392590 | 0.06678345 | |
| | 0.31914771 | 0.06738713 | |
| | 0.35436951 | 0.06804707 | |
| | 0.38959132 | 0.06883469 | |
| | 0.42481312 | 0.06965476 | |
| | 0.46003493 | 0.07056601 | |
| | 0.49525673 | 0.07151896 | |
| | 0.53047854 | 0.07254034 | |
| | 0.56570034 | 0.07363752 | |
| | 0.60092215 | 0.07479222 | |
| | | | |

```
0.63614395
                                0.07599800
          0.67136576
                                0.07731324
                                0.07864679
          0.70658756
          0.74180937
                                0.08006326
          0.77703117
                                0.08153934
          0.81225298
                                0.08307981
          0.84747478
                                0.08468211
          0.88269659
                                0.08638300
          0.91791839
                                0.08815842
          0.95314020
                                0.09006283
          0.98836200
                                0.09206427
          1.02358381
                                0.09418956
          1.05880561
                                0.09643203
          1.09402742
                                0.09878849
          1.12924922
                                0.10132013
                                0.10394818
          1.16447103
          1.19969283
                                0.10666283
          1.23491463
                                0.10955160
                                0.11254530
          1.27013644
          1.30535824
                                0.11581166
          1.34058005
                                0.11909043
          1.37580185
                                0.12243367
          1.41102366
                                0.12605572
          1.44624546
                                0.13002564
          1.48146727
                                0.13416900
          1.51668907
                                0.13846513
                                0.14297229
          1.55191088
          1.58713268
                                0.14796369
          1.62235449
                                0.15331668
          1.65757629
                                0.15968391
          1.69279810
                                0.16634975
                                0.17301559
          1.72801990
*MAT_ADD_EROSION
Ś
       mid
                 excl
                                               effeps
                                                          voleps
                                                                          ncs
                         mxpres
                                     mneps
        10
                                                                        1e-08
$
    mnpres
                          sigvm
                                                           sigth
                                                                       failtm
                sigp1
                                     mxeps
                                                epssh
Ś
                                                           dcrit
                                                                       lcregd
      idam
               dmgtyp
                          lcsdg
                                     ecrit
                                               dmgexp
        -1
$
                                        р3
     dityp
                   р1
                              p2
                   99
$
     detyp
                dctyp
                              q1
                                        q2
                          5e-05
*DEFINE_CURVE_TITLE
Triaxiality curve of undamaged material
        99
                                    10.000
                   -1
                -0.33
                                  5.000000
```

| | 0 | 0.035687 | |
|------|------|----------|--|
| | 0.33 | 0.035687 | |
| | 1 | 0.035687 | |
| \$ | | | |
| *END | | | |

```
_____
   Material card for PP - 124
$-----
*MAT_PLASTICITY_COMPRESSION_TENSION_TITLE
Card Template
$#
      mid
                                                              fail
                 ro
                                    pr
                           е
                                              С
       10
           0.890e-6
                      0.8926
                                  0.32
                                                          0.191209
$#
    lcidc
              lcidt
                       lcsrc
                                 lcsrt
                                         srflag
                                                   lcfail
                                                                ec
       14
                 15
                                            0.0
                                                           0.44217
$#
                                          pcutf
       рс
                 pt
                       pcutc
                                 pcutt
$#
        k
*DEFINE_CURVE_TITLE
LCIDT
       15
$#
                 a1
                                    01
         0.00216631
                            0.01620054
         0.00610470
                            0.01837781
         0.01004309
                            0.01987185
         0.01398148
                            0.02115550
         0.01791987
                            0.02204875
         0.02185826
                            0.02285015
         0.02579665
                            0.02350638
         0.02973504
                            0.02395497
         0.03367343
                            0.02436592
         0.03761182
                            0.02468245
         0.04155021
                            0.02488758
                            0.02507940
         0.04548860
         0.19120901
                            0.02970000
*DEFINE_CURVE_TITLE
LCIDC
       14
$#
                 a1
                                    01
         0.00407005
                            0.04332045
         0.03389433
                            0.04462071
         0.06371861
                            0.04481184
         0.09354289
                            0.04467620
         0.12336717
                            0.04449754
         0.15319145
                            0.04440057
         0.18301573
                            0.04436122
         0.21284002
                            0.04444806
                            0.04467265
         0.24266430
                            0.04499726
         0.27248858
         0.30231286
                            0.04534862
         0.33213714
                            0.04570894
         0.36196142
                            0.04619820
         0.39178570
                            0.04676628
         0.42160998
                            0.04745631
         0.45143426
                            0.04828290
```

```
0.48125854
                                0.04912772
          0.51108282
                                0.05000405
                                0.05080395
          0.54090710
          0.57073139
                                0.05180399
          0.60055567
                                0.05293038
          0.63037995
                                0.05413946
          0.66020423
                                0.05539840
          0.69002851
                                0.05680950
          0.71985279
                                0.05836414
          0.74967707
                                0.06002681
          0.77950135
                                0.06179548
          0.80932563
                                0.06372214
          0.83914991
                                0.06582456
          0.86897419
                                0.06810923
          0.89879847
                                0.07057144
          0.92862275
                                0.07323778
          0.95844704
                                0.07612174
          0.98827132
                                0.07931039
          1.01809560
                                0.08292480
          1.04791988
                                0.08681147
          1.07774416
                                0.09100828
          1.10756844
                                0.09560162
          1.13739272
                                0.10062997
                                0.10607497
          1.16721700
          1.19704128
                                0.11219684
          1.22686556
                                0.11913389
                                0.12710905
          1.25668984
          1.28651412
                                0.13574894
          1.31633841
                                0.14503506
          1.34616269
                                0.15538734
          1.37598697
                                0.16713807
          1.40581125
                                0.18079673
                                0.19662168
          1.43563553
          1.46545981
                                0.21318322
Ś
*MAT_ADD_EROSION
$
       mid
                 excl
                         mxpres
                                     mneps
                                               effeps
                                                          voleps
                                                                    numfip
        10
$
    mnpres
                                                                   impulse
                sigp1
                          sigvm
                                     mxeps
                                                epssh
                                                           sigth
$
                                                                    fadexp
      idam
               dmgtyp
                          lcsdg
                                               dmgexp
                                                           dcrit
                                     ecrit
        -1
$
     dityp
                   p1
                              p2
                                        р3
                   99
$
                dctyp
     detyp
                                        q2
                              q1
                          5e-05
*DEFINE_CURVE_TITLE
Triaxiality curve of undamaged material
        99
```

| | -1 | 10.000 |
|------|-------|------------|
| | -0.33 | 5.000 |
| | 0 | 0.19120901 |
| | 0.33 | 0.19120901 |
| | 1 | 0.19120901 |
| \$ | | |
| *END | | |